



HAL
open science

A series of two-phase models for grain-fluid flows with dilatancy

François Bouchut, Elias Drach, Enrique D Fernández-Nieto, Anne Mangeney, Gladys Narbona-Reina

► **To cite this version:**

François Bouchut, Elias Drach, Enrique D Fernández-Nieto, Anne Mangeney, Gladys Narbona-Reina. A series of two-phase models for grain-fluid flows with dilatancy. 2024. hal-04573125

HAL Id: hal-04573125

<https://univ-eiffel.hal.science/hal-04573125>

Preprint submitted on 13 May 2024

HAL is a multi-disciplinary open access archive for the deposit and dissemination of scientific research documents, whether they are published or not. The documents may come from teaching and research institutions in France or abroad, or from public or private research centers.

L'archive ouverte pluridisciplinaire **HAL**, est destinée au dépôt et à la diffusion de documents scientifiques de niveau recherche, publiés ou non, émanant des établissements d'enseignement et de recherche français ou étrangers, des laboratoires publics ou privés.

A series of two-phase models for grain-fluid flows with dilatancy

François Bouchut*, Elias Drach*, Enrique D. Fernández-Nieto[†],
Anne Mangeney^{‡§}, Gladys Narbona-Reina[†]

May 8, 2024

Abstract

Debris flows are a growing natural hazard due to climate change and population density. To effectively assess this hazard, simulating field-scale debris flows at a reasonable computational cost is crucial. We enhance existing debris flows models by rigorously deriving a series of depth-averaged shallow models with varying complexities describing the behavior of grain-fluid flows, considering granular mass dilatancy and pore fluid pressure feedback. The most complete model includes a mixture layer with an upper fluid layer and solves for solid and fluid velocity in the mixture and for the upper fluid velocity. Simpler models are obtained by assuming velocity equality in the mixture or single-layer descriptions with a virtual thickness. Simulations in a uniform configuration mimicking submarine landslides and debris flows reveal that these models are extremely sensitive to the rheology, the permeability (grain diameter), and initial volume fraction, parameters that are hard to measure in the field. Notably, velocity equality assumptions in the mixture hold true only for low permeability (corresponding to grain diameters $d = 10^{-3}$ m). One-layer models' results can strongly differ from those of the complete model, for example the mass can stop much earlier. One-layer models however provide a rough estimate of two-layer models when permeability is low, initial volume fraction is distant from critical, and upper fluid layer is very thin. Our work demonstrates the need of developing two-layer models accounting for dilatancy and accounting for an upper layer made either of fluid or grains.

*Laboratoire d'Analyse et de Mathématiques Appliquées (UMR 8050), CNRS, Université Gustave Eiffel, UPEC, F-77454, Marne-la-Vallée, France (francois.bouchut@univ-eiffel.fr, elias.drach@univ-eiffel.fr)

[†]Departamento de Matemática Aplicada I, Universidad de Sevilla. E.T.S. Arquitectura. Avda, Reina Mercedes, s/n. 41012 Sevilla, Spain (edofer@us.es, gnarbona@us.es)

[‡]Université Paris Diderot, Université Paris Cité, Institut de Physique du Globe de Paris, Equipe de Sismologie, 1 rue Jussieu, 75005 Paris, France (mangeney@ipgp.jussieu.fr)

[§]ANGE team, INRIA, CETMEF, Lab. J. Louis Lions, Paris, France

Contents

1	Introduction	3
2	Full two-layer model with three velocities	5
2.1	Notation and main variables	6
2.2	Rheological laws in viscous-inertial regimes	7
2.2.1	Rheology describing the critical state	7
2.2.2	Dilatancy law	9
2.3	Two-layer model with three velocities (A1)	11
2.3.1	Conservation equations and closure relations	11
2.3.2	Computation of the basal solid pressure	13
2.4	Origin and impact of dilatancy in mixture models	14
2.4.1	Dilatancy and pore fluid pressure	14
2.4.2	Dilatancy and fluid transfer rate	15
2.4.3	Relation between the key variables	15
3	Simplest one-velocity models	17
3.1	Two-layer model with one velocity (B2)	17
3.1.1	System of equations	17
3.1.2	Model (B2) expressed as a function of the virtual thickness	18
3.2	One-layer model with one velocity (C2)	20
3.3	Impact of considering a virtual thickness	21
3.4	Comparison with the Iverson-George model	21
3.4.1	The Iverson-George model	21
3.4.2	Comparison with our one-layer one-velocity model (C2)	23
4	Models with two velocities in the mixture	24
4.1	Two-layer model with two velocities in the mixture (B1)	24
4.2	Rewriting the model (B1) using the virtual thickness	27
4.3	Oversimplified one-layer model with two velocities (C1)	28
4.4	Comparison with the Meng-Wang model	29
4.4.1	The Meng-Wang model	29
4.4.2	Obtaining our model (C1)	31
5	Numerical illustrations in uniform regime	31
5.1	Immersed flows - effect of rheology	32
5.1.1	Physical and rheological parameters	32
5.1.2	Flow behavior in loose and dense cases	33
5.1.3	Influence of the rheology	35
5.2	Debris flow configuration - basal pressure	36
5.2.1	Physical and rheological parameters	36
5.2.2	Computation of the solid pressure at the bottom	38
5.3	Comparison of all the proposed models for debris flows	39
5.3.1	One-layer models compared to Iverson-George and Meng-Wang models	39
5.3.2	Influence of grain diameter and drag force between the layers	40
5.3.3	Influence of the thickness of the upper fluid layer	45
5.3.4	Influence of φ^0 and η_f	48
6	Conclusion	48

A	Two-layer three-velocity model (A1) modified from [7]	54
A.1	Summary of boundary conditions	54
A.2	Fluid viscous shear at the bottom	56
A.3	Drag at the upper-fluid/mixture interface	56
A.4	Alternative descriptions proposed in the literature	59
A.4.1	Fluid viscous stress and basal fluid shear stress at the bottom	60
A.4.2	Drag and mass exchange at the interface	60
A.4.3	Inter-phase friction	63
A.5	Energy balance	65
A.6	Derivation of a pressure evolution equation	65
B	Equivalence of notations in our model and in Iverson and George [23, 18] and Meng and Wang [35]	68
C	Comparison with the Iverson-George model: further details	70
C.1	Details of calculations	70
C.2	Comparison of the basal pore pressure equation	72
D	Comparison with the Meng-Wang model: further details	75
D.1	Details of calculations	75
D.2	Comparison of the boundary conditions	76
E	Calculation details of the two-phase model (B1)	78
F	Alternative simplified models	79
F.1	One-layer one-velocity model with solid mass conservation	80
F.2	Two layer model with one velocity in the mixture and one velocity in the upper-fluid layer (A2)	80
F.3	Two-layer model with one velocity for each phase	81
G	Models in uniform regime	82
G.1	Our hierarchy of models in uniform regime	82
G.2	Other models in uniform regime	87
H	Supplementary material for numerical results	88
H.1	Influence of the parameters on long-term stationary states	88
H.2	Forces in models in uniform regime	88

1 Introduction

Landslide and debris flows play a key role in erosion processes at the Earth’s surface and represent major natural hazards threatening life and property in mountainous, volcanic, and coastal areas. Recent examples include the debris flows that occurred in the Democratic Republic of Congo in 2023, causing more than 400 deaths [<https://blogs.agu.org/landslideblog/>]. One of the ultimate goals of research involving the dynamic analysis of landslides and debris flows is to produce tools for detection of natural instabilities and prediction of the velocity, dynamic impact and runout extent of the associated landslides and debris flows. Such tools will then be used to design hazard maps, early warning systems and land-use planning.

In recent years, significant progress in the mathematical, physical, and numerical modeling of these gravitational flows has made it possible to develop and use numerical models to investigate geomorphological processes and assess risks related to such natural hazards. Solving the complete 3D equations of field-scale granular mass motion with sufficient resolution to describe the real topography involves prohibitive computational costs. For this reason, a class of efficient techniques developed and successfully employed to reproduce a large range of experimental and geological observations makes use of a depth-averaged continuum description based on the shallow layer approximation (*i.e.* the thickness of the flowing mass is assumed to be small compared to its downslope extension), *e.g.* [53, 33, 32, 40, 30, 47, 21]. However, most of these models do not take into account the co-existence and interaction of a fluid (water and mud) and solid phase within the flowing mass, which play a key role in the flow dynamics. This limitation prevents accurate hazard assessment [45, 46] and full interpretation of field measurements, in particular seismic data which could be used to detect such events [39, 1].

Iverson [22] first addressed the need to include interstitial fluid effects in the constitutive behavior of the mass flow and developed a shallow layer model for a solid-fluid mixture, under the simplifying assumptions of constant solid volume fraction and equality of the fluid and solid velocity. The flow is described by a single set of equations for the density and momentum of the mixture, which formally appears as a single-phase model with a stress term accounting for contributions from the two constituents. A pore pressure advection-diffusion equation was added based on experimental measurements. Various versions and applications of this grain-fluid mixture model have since been presented [50]. In parallel, Pitman and Le [48] have proposed a depth-averaged two-fluid model for debris flows that contains mass and momentum equations for both the fluid and solid phase, thus providing equations for the velocities of the two phases and for the solid volume fraction, without any additional equation for the pore fluid pressure. Pelanti et al. [31, 44] proposed numerical schemes to solve these equations. Bouchut et al. [6] showed that a closure relation was missing in these previous models. Indeed, this closure was implicitly (artificially) replaced by the assumption that the upper surfaces of the solid and fluid phases coincide with the free surface. This is however not the case in real flows due to dilatancy of the granular mass that expel or incorporate the fluid at its surface as it contracts or dilates, respectively.

The challenge is thus to derive a closure relation describing the dilation/contraction of the solid phase that decrease/increase the pore fluid pressure with strong feedback on the friction experienced by the granular phase [42, 52, 24, 7]. Such effects have been shown to dramatically change the dynamics of the grain-fluid mixture [51, 7, 8], possibly leading to its complete liquefaction. Dilatancy laws can be formulated in the framework of the critical state theory based on the existence of a well-defined steady shear state depending only on the nature of the granular material and used as reference state. Deviations from the critical state are formulated as state variables to describe transient deformations [12]. Iverson and George proposed a shallow depth-averaged mixture model to describe these dilatancy effects, assuming equal downslope velocity for the solid and fluid phases. They introduced a so-called *virtual surface*, eliminating the need to describe whether the layer on top of the mixture is a solid or a fluid. Following a different approach, Bouchut et al. in [7] proposed a two-phase model with an upper fluid layer capable of collecting or providing water during contraction or dilation of the mixture. However, this model does not describe the situation where the upper layer is made only of grains. Such a configuration has been studied in [34], where a depth-averaged model for debris flows is proposed dealing with transitions from pure fluid/solid configurations to under-saturated or over-saturated mixtures. However, this model does not account for dilatancy or mass exchange. In [35], Meng and Wang combined the idea of the *virtual surface* introduced by Iverson and George and the dilatancy

approach developed in Bouchut et al. [7], keeping two different velocities in the mixture for the solid and fluid phases. The exchange of mass between the mixture and the upper fluid layer, introduced in [7], was also adopted using a particular interpretation in which the model does not account for a layer above to collect or provide water. The mass is instead said to pass through a virtual surface. Luca et al. [29] developed a depth-averaged two-layer model for over-saturated flows that considers bottom curvature and accounts for two velocities in the mixture and one independent velocity for the upper-fluid layer, similar to the approach of Bouchut et al. [7] although dilatancy effects are not considered. More recently, Sun et al. [54] investigated submarine avalanches, presenting a model that accounts for dilatancy and mass exchange, akin to Bouchut et al. [7]. This model features one velocity for the mixture and an independent velocity for the upper fluid layer, making it an immersed version of the model proposed by Drach [14].

Another difference between the Bouchut et al. [7] and Iverson and George [23] models lies in the calculation of the pore fluid pressure. In the Iverson and George model, a differential equation is proposed to solve basal fluid pressure. This equation comes from the assumption of elastic deformation of the grains [4, 27, 38], which is assumed to be negligible in Bouchut et al. [7].

We lack a clear understanding and quantification of the hypotheses of the models and of the pressure calculation and the assumption of a virtual free surface. This results from the complexity of the derivation of shallow depth-averaged equations with dilatancy and of the strong coupling between the different terms. Numerical resolution of these systems is very challenging [8, 17] and sometimes models are only partially solved using key simplifications. For example, the Meng and Wang model in [35] is solved for a uniform configuration as in [7]. In [34], the proposed model is solved for a steady-state configuration and a specified velocity profile. A model for submarine avalanches with the same fluid and solid velocity in the mixture is considered in [54] and is solved only for the immersed configuration, avoiding the difficulty of the upper-layer thickness that may become negative.

This paper aims to clarify these points by deriving a series of models including dilatancy from complex two-phase two-layer models to simple one-layer one-velocity mixture models, clearly highlighting the assumptions made in each. A main objective is to show precisely how they compare with one another and with two relevant models in the literature, namely the one presented in [23, 18] by Iverson and George and the one in [35] by Meng and Wang. We then perform a series of numerical simulations of uniform grain-fluid flows on inclined planes to quantify how the differences between the models and their strong sensitivity to the rheology and flow parameters impact the flow behavior.

2 Full two-layer model with three velocities

We present here the equations of the two-layer model for grain-fluid flows with dilatancy effects derived in [7], with slight modifications related to the boundary conditions between the two layers and the updated rheological laws proposed in the literature. This model solves the depth-averaged mass and momentum conservation equations for both a grain-fluid layer and an upper fluid layer as well as the exchange of mass and momentum between these layers (see figure 1). The key idea in this model is to allow the fluid to be expelled from the mixture during contraction and to be sucked into the mixture during dilation thanks to the presence of a thin fluid layer on top of the mixture (grain-fluid) layer. In the model derived in [7], the thickness $h_f(t, x, y)$ of this layer cannot be negative (figure 1). As a result, the pure fluid phase is always present at the free surface as long as $h_f > 0$. In the limit case where $h_f = 0$, the upper free surface coincides with the surface of the mixture. The opposite configuration with a thin layer of dry granular

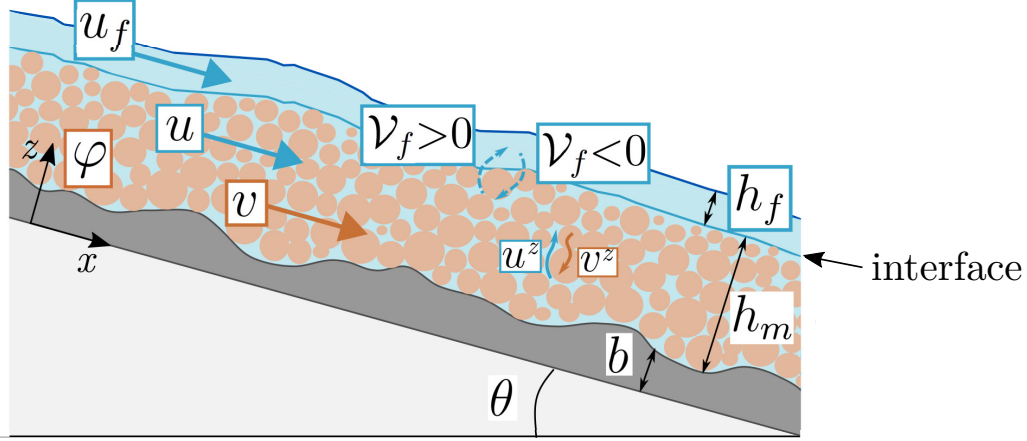


Figure 1: Flow configuration and notations for the full two-layer model with three velocities (A1) from [7]. The velocity vectors u , v , u_f are in the x, y plane. Even though the velocities u^z and v^z in the direction perpendicular to the slope do not appear explicitly in the model, the difference between them controls the excess pore fluid pressure. The dilatancy law specifying $\text{div } \mathbf{v}$ makes it possible to replace $u^z - v^z$ by an expression involving only the downslope velocities (see section 2.4).

material on top of the mixture also occurs in reality, as suggested in rotating drum experiments [28, 41, 34], but will be dealt with in a forthcoming study. The depth-averaged model in [7] was obtained from the 3D Jackson’s equations for a grain-fluid mixture [26] with appropriate boundary conditions. We used classical no-penetration and friction boundary conditions at the bottom and kinematic and stress-free conditions at the free surface. The challenge in deriving depth-averaged models lies in the choice of the conditions imposed at the interface between the mixture and fluid layers. Indeed, even if the boundary separating these layers appears as an interface in two-layer depth-averaged models, the real fluid phase is continuous across this interface. However, conditions at the interface must be imposed to relate depth-averaged quantities that are discontinuous, even though their non-averaged values are continuous. For the sake of clarity, we review the different choices for the conditions at this interface in Appendix A.3 and only present here the main closure relations.

2.1 Notation and main variables

The notations for our complete model are sketched in figure 1 and detailed in table 1 (for the sake of simplicity, the superscript \mathbf{x} and the “bar” notation used in [7] have been removed). We denote the base vector in the (x, y) plane as $\mathbf{e}_x = (1, 0)^t$. The systems that will be presented here correspond to depth-averaged models, therefore the quantities only depend on the slope coordinates x and y , with no dependency on the normal coordinate z . The slope-aligned (*i.e.* along the inclined plane of angle θ) depth-averaged 2D velocities of the solid and fluid phases in the mixture, and of the upper fluid phase, are denoted by $v(t, x, y)$, $u(t, x, y)$, and $u_f(t, x, y)$, respectively. The 3D solid and fluid velocities in the mixture are denoted by $\mathbf{v}(t, x, y, z) = (v(t, x, y), v^z(t, x, y, z))$ and $\mathbf{u}(t, x, y, z) = (u(t, x, y), u^z(t, x, y, z))$, respectively. The thickness of the mixture layer is $h_m(t, x, y)$. The depth-averaged solid volume fraction is denoted by $\varphi(t, x, y)$, often referred to as the compacity or the packing fraction. The fixed bottom variation $b(x, y)$ is measured in the direction normal to a fixed reference plane inclined at an angle θ (our convention is that $\theta < 0$ in the situation of left to right inclination as in figure 1), and we denote

$\tilde{b}(x) = x \tan \theta$. The gradient notation is $\nabla f = (\partial_x f, \partial_y f)$ for any function $f(t, x, y)$. The bulk density of the mixture is defined as

$$\rho = \varphi \rho_s + (1 - \varphi) \rho_f, \quad (2.1)$$

where ρ_s and ρ_f are the constant densities for grains and fluid, respectively. The average mixture velocity is defined as

$$V_m = \frac{\rho_s \varphi v + \rho_f (1 - \varphi) u}{\rho}. \quad (2.2)$$

Finally, we call \mathcal{V}_f the fluid transfer rate between the mixture and upper fluid layers (figure 1), $\rho_f \mathcal{V}_f$ thus being the fluid mass flux through the interface.

2.2 Rheological laws in viscous-inertial regimes

As in most depth-averaged models for debris flows, the rheology appears in our model in the basal shear stress of the solid phase $\tau_{s|b}$ through a Coulomb-type friction law

$$\tau_{s|b} = \mu p_{s|b}, \quad (2.3)$$

where μ is the friction coefficient and $p_{s|b}$ the basal pressure of the solid phase. In such models, the challenge is to specify the friction coefficient μ and, if dilatancy is accounted for, the solid volume fraction φ . In the framework of the Critical State theory, two steps are necessary to describe the rheological behavior (*i.e.* constitutive laws) of a grain-fluid system. First, we must specify constitutive laws describing the (steady) critical state reached at the equilibrium, *i.e.* (i) the critical-state solid volume fraction φ^{eq} and (ii) the critical-state friction coefficient μ^{eq} (section 2.2.1). These empirical laws are deduced from lab-scale experiments or Discrete Element simulations of steady and uniform shear flows (flows in the critical state). Once the critical-state solid volume fraction and friction coefficient have been defined, the model should describe how transient deformation depends on the deviation from this critical state. This is done in the dilatancy law that relates φ and μ to the dilatancy angle ψ (section 2.2.2).

2.2.1 Rheology describing the critical state

As in recent studies, constitutive laws describing steady uniform flows (*i.e.* at the critical state) are written in terms of a combination of two dimensionless numbers, based on the assumption of additivity of inertial and viscous stresses [10, 9, 57, 2, 55]. These two independent numbers I and J characterize inertial and viscous regimes, respectively:

$$I = \frac{d \dot{\gamma}}{\sqrt{p_{s|b}/\rho_s}}, \quad J = \frac{\eta_f \dot{\gamma}}{p_{s|b}}, \quad (2.4)$$

where $p_{s|b}$ represents the solid pressure at the bottom. At imposed pressure, the shear stress is proportional to I^2 in the inertial regime and to J in the viscous regime. The transition between these regimes is given by the Stokes number, defined by the ratio between the inertial and viscous stress scales (cf. [55])

$$\text{St} = I^2/J = \frac{\rho_s \dot{\gamma} d^2}{\eta_f}. \quad (2.5)$$

To describe all possible regimes, from inertial to viscous flows, different combinations of I and J have been proposed in the literature (see table 2). These inertial-viscous numbers may all be written as

$$\mathcal{J} = \alpha_i I^2 + \alpha_v J \quad (2.6)$$

Physical variables	Notation
Mixture density	ρ
Thickness of the upper fluid layer	h_f
Thickness of the mixture layer	h_m
3D solid velocity	\mathbf{v}
Depth-averaged slope-aligned mixture-solid velocity	v
Depth-averaged slope-aligned mixture-fluid velocity	u
Depth-averaged slope-aligned upper fluid velocity	u_f
Depth-averaged slope-aligned mixture velocity	V_m
Depth-averaged solid volume fraction	φ
Critical-state solid volume fraction	φ^{eq}
Friction coefficient	μ
Critical-state friction coefficient	μ^{eq}
Fluid transfer rate	\mathcal{V}_f
Solid pressure	p_s
Fluid pressure in the mixture	p_{f_m}
Excess pore fluid pressure in the mixture	$p_{f_m}^e$
Fluid pressure in the upper layer	p_f
Effective viscosity	η_e
Physical parameters	
Solid density	ρ_s
Fluid density	ρ_f
Dynamic fluid viscosity	η_f
Mean grain diameter	d
Hydraulic permeability	k
Material friction angle	δ
Dilatancy angle	ψ
Dilatancy law coefficient	K
Inertial number	I
Viscous number	J
Inertial-viscous number for φ^{eq}	$\mathcal{J}_\varphi = \alpha_\varphi I^2 + J$
Inertial-viscous number for μ^{eq}	$\mathcal{J}_\mu = \alpha_\mu I^2 + J$
Rheological parameters	$\varphi_c, \mu_c, \Delta\mu, I_0, b, \alpha_\varphi, \alpha_\mu$

Table 1: Notations for the physical variables and parameters in the depth-averaged two-phase (grain-fluid) model with an upper fluid layer.

where α_i and α_v are two constant coefficients that define the relative importance of inertial and viscous numbers and depend on the material involved. Tapia et al. 2022 [55] showed that α_i and α_v are not the same in the rheological laws defining φ^{eq} and μ^{eq} , respectively. Note that inertial-viscous numbers can also be written in terms of the Stokes number:

$$\mathcal{J} = I^2 \left(\alpha_i + \alpha_v \frac{1}{\text{St}} \right) = J(\alpha_i \text{St} + \alpha_v).$$

The inertial regime corresponds to large Stokes numbers and thus to $\mathcal{J} \simeq \alpha_i I^2$ and the viscous regime to small Stokes numbers and thus to $\mathcal{J} \simeq \alpha_v J$. We choose here a rheological law as in [55], even though we use nonlinear functions to define φ^{eq} and μ^{eq} , in order to bound their value for infinite \mathcal{J} numbers. We define two inertial-viscous numbers involved in the critical-state solid volume fraction φ^{eq} and friction coefficient μ^{eq} , respectively,

$$\mathcal{J}_\varphi = \alpha_\varphi I^2 + J \quad \text{and} \quad \mathcal{J}_\mu = \alpha_\mu I^2 + J, \quad (2.7a)$$

where α_φ and α_μ are two constant coefficients. The critical-state solid volume fraction is then defined as

$$\varphi^{\text{eq}}(\mathcal{J}_\varphi) = \frac{\varphi_c}{1 + b_\varphi \mathcal{J}_\varphi^{1/2}}, \quad (2.7b)$$

where b_φ is a calibration constant and φ_c the static value of the critical state solid volume fraction. Finally, the critical friction coefficient is defined as

$$\mu^{\text{eq}}(\mathcal{J}_\mu) = \mu_c + \frac{\Delta\mu}{1 + \frac{I_0}{\mathcal{J}_\mu^{1/2}}}, \quad (2.7c)$$

where $\mu_c = \tan \delta$ is the static value of the critical state friction coefficient, with δ the granular friction angle. $\Delta\mu$ and I_0 are constant parameters (see table 2 for their values in the literature). Numerical simulations will be performed in Section 5 to show how strongly these coefficients impact the flow behavior.

2.2.2 Dilatancy law

Following [52, 42] the dilatancy law is given by

$$\text{div } \mathbf{v} = \Phi = \dot{\gamma} \tan \psi, \quad (2.8)$$

with ψ the dilatancy angle related to the deviation from critical state, defined by

$$\tan \psi = K(\varphi - \varphi^{\text{eq}}(\mathcal{J}_\varphi)), \quad (2.9)$$

and the shear rate approximated by (cf. [10])

$$\dot{\gamma} = \frac{5}{2} \frac{|v|}{h_m}. \quad (2.10)$$

When the flow is denser than the flow in the critical state ($\varphi > \varphi^{\text{eq}}$), the dilatancy angle ψ is positive and the solid phase dilates, and vice versa. The friction coefficient in the transient regime involves the dilatancy angle as

$$\mu = (\mu^{\text{eq}}(\mathcal{J}_\mu) + \tan \psi)_+. \quad (2.11)$$

Note that the dilatancy rules (2.8), (2.11) for φ and μ use the most simple linear expansions involving the dilatancy factor (2.9) expressed linearly in terms of the deviation from critical state. A positive part has been put in (2.11) as a minimal correction to ensure that μ is nonnegative.

Reference	Regime	Non-dim. numbers	μ^{eq}	φ^{eq}	Coefficients
Cassar et al. 2005 [10]	inertial, viscous	$I_c = \begin{cases} I & \text{inertial} \\ \frac{J}{\alpha} & \text{viscous} \end{cases}$	$\mu_c + \frac{\Delta\mu}{1 + \frac{I_0}{I_c}}$	–	$\mu_c = 0.43,$ $\Delta\mu = 0.39,$ $I_0 = 0.27$ $\alpha = 0.01$
Pailha and Pouliquen 2009 [43]	viscous	J	$\mu_c + K_1 J$	$\varphi_c - k_2 J$	$\varphi_c = 0.582, \mu_c = 0.415,$ $K_1 = 90.5, K_2 = 25$
Boyer et. al 2011 [9]	viscous	J	$\mu_c + \frac{\Delta\mu}{1 + \frac{I_0}{J}} + J + \frac{5}{2}\varphi_c J^{1/2}$	$\frac{\varphi_c}{1 + J^{1/2}}$	$\varphi_c = 0.585, \mu_c = 0.32,$ $\Delta\mu = 0.38,$ $I_0 = 0.005$
Trulsson et al. 2012 [57]	inertial, viscous	$\mathcal{J} = \alpha_i I^2 + J$	$\mu_c + \frac{\Delta\mu}{1 + \frac{I_0}{\mathcal{J}^{1/2}}}$	$\varphi_c - b \mathcal{J}^{1/2}$	$\varphi_c = 0.814, \mu_c = 0.277,$ $\Delta\mu = 0.573,$ $I_0 = 0.29,$ $\alpha_i = 0.635, b = 0.42$
Iverson and George 2014 [23]	inertial, viscous	$N = \frac{J}{1 + I^2}$	μ_c	$\frac{\varphi_c}{1 + \sqrt{N}}$	$\varphi_c = 0.56,$ $\mu_c = 0.55$
Amarsid et al. 2017 [2]	inertial, viscous	$\mathcal{J} = (\alpha_i I^2 + \alpha_v J)^{1/2}$	$\mu_c + \frac{\Delta\mu}{1 + \frac{b}{\mathcal{J}}}$	$\frac{\varphi_c}{1 + b \mathcal{J}}$	$\varphi_c = 0.8123, \mu_c = 0.28,$ $\Delta\mu = 0.783,$ $b = 0.246,$ $\alpha_i = 1, \alpha_v = 2$
Bouchut et al. 2021 [8]	inertial	I	$\mu_c + \frac{\Delta\mu}{1 + \frac{I_0}{I}}$	$\frac{\varphi_c}{1 + \frac{\tilde{K} I}{\varphi_c}}$	$\varphi_c = 0.582, \mu_c = 0.48,$ $\Delta\mu = 0.25,$ $I_0 = 0.279,$ $\tilde{K} = 0.2$
Montella et al. 2021 [38]	viscous	J	$\mu_c + \frac{\Delta\mu}{1 + \frac{I_0}{J}}$	$\frac{\varphi_c}{1 + J^{1/2}}$	$\varphi_c = 0.585, \mu_c = 0.425,$ $\Delta\mu = 0.34,$ $I_0 = 0.004$
Athani et al. 2022 [3]	viscous	J	μ_c	$\varphi_c - K J^\beta$	$\varphi_c = 0.58, \mu_c = 0.5,$ $K = 0.67,$ $\beta = 0.44$
Tapia et al. 2022 [55]	inertial, viscous	$\mathcal{J}_\mu = \alpha_\mu I^2 + J,$ $\mathcal{J}_\varphi = \alpha_\varphi I^2 + J$	$\mu_c(1 + a_\mu \mathcal{J}^{1/2})$	$\varphi_c(1 - a_\varphi \mathcal{J}^{1/2})$	$\varphi_c = 0.615, \mu_c = 0.31,$ $\alpha_\mu = 0.0088, \alpha_\varphi = 0.1$ $a_\mu = 11.29, a_\varphi = 0.66$

Table 2: Rheological laws in the literature

2.3 Two-layer model with three velocities (A1)

Let us present here the full model derived from [7] with the rheology defined above. This model describes the behavior of a mixture with different velocities for the solid and fluid phases u , v , respectively, as well as an upper fluid layer of velocity u_f (see figure 1). Only slight modifications have been made in the model derivation compared to [7], owing to the different choice of conditions at the bottom and at the mixture/upper fluid interface, as well as to the description of viscous dissipation for the fluid phase (see Appendix A.2 and A.3 for details). The free surface, interfacial and basal boundary conditions are summarized in Appendix A.1.

2.3.1 Conservation equations and closure relations

The mass conservation equations for the solid and fluid phases in the mixture and for the fluid phase in the upper-layer read, respectively

$$\partial_t(\rho_s \varphi h_m) + \nabla \cdot (\rho_s \varphi h_m v) = 0, \quad (2.12a)$$

$$\partial_t(\rho_f(1 - \varphi)h_m) + \nabla \cdot (\rho_f(1 - \varphi)h_m u) = -\rho_f \mathcal{V}_f, \quad (2.12b)$$

$$\partial_t(\rho_f h_f) + \nabla \cdot (\rho_f h_f u_f) = \rho_f \mathcal{V}_f. \quad (2.12c)$$

The corresponding momentum conservation equations are

$$\partial_t(\rho_s \varphi h_m v) + \nabla \cdot (\rho_s \varphi h_m v \otimes v) = S_v \quad (2.13a)$$

$$\partial_t(\rho_f(1 - \varphi)h_m u) + \nabla \cdot (\rho_f(1 - \varphi)h_m u \otimes u) = S_u \quad (2.13b)$$

$$\partial_t(\rho_f h_f u_f) + \nabla \cdot (\rho_f h_f u_f \otimes u_f) = S_f \quad (2.13c)$$

The source terms are given respectively by

$$\begin{aligned} S_v = & \underbrace{-g \cos \theta \varphi h_m (\rho_s \nabla(b + h_m) + \rho_f \nabla h_f)}_{\text{hydrostatic pressure}} - g \cos \theta (\rho_s - \rho_f) \frac{h_m^2}{2} \nabla \varphi + \underbrace{(1 - \varphi) h_m \overline{\nabla p_{f_m}^e}}_{\text{excess pore pressure}} \\ & + \underbrace{\beta h_m (u - v)}_{\text{drag in the mixture}} + \underbrace{k_f \frac{\rho_s \varphi}{\rho} (u_f - V_m)}_{\text{drag with upper-fluid}} - \underbrace{\mu \operatorname{sgn}(v) (\varphi (\rho_s - \rho_f) g \cos \theta h_m - (p_{f_m}^e)|_b)}_{\text{solid bottom friction}} \\ & - \underbrace{\varphi h_m \rho_s g \sin \theta \mathbf{e}_x}_{\text{gravity}}, \end{aligned} \quad (2.14a)$$

$$\begin{aligned} S_u = & - \underbrace{(1 - \varphi) h_m \rho_f g \cos \theta \nabla(b + h_m + h_f)}_{\text{hydrostatic pressure}} - \underbrace{(1 - \varphi) h_m \overline{\nabla p_{f_m}^e}}_{\text{excess pore pressure}} - \underbrace{((1 - \lambda_f)u + \lambda_f u_f) \rho_f \mathcal{V}_f}_{\text{fluid transfer}} \\ & - \underbrace{\beta h_m (u - v)}_{\text{drag in the mixture}} + \underbrace{k_f \frac{\rho_f (1 - \varphi)}{\rho} (u_f - V_m)}_{\text{drag with upper-fluid}} - \underbrace{\frac{5 \eta_e (1 - \varphi)}{2 h_m} u}_{\text{fluid bottom friction}} - \underbrace{(1 - \varphi) h_m \rho_f g \sin \theta \mathbf{e}_x}_{\text{gravity}}, \end{aligned} \quad (2.14b)$$

$$\begin{aligned} S_f = & - \underbrace{\rho_f h_f g \cos \theta \nabla(b + h_m + h_f)}_{\text{hydrostatic pressure}} + \underbrace{((1 - \lambda_f)u + \lambda_f u_f) \rho_f \mathcal{V}_f}_{\text{fluid transfer}} \\ & - \underbrace{k_f (u_f - V_m)}_{\text{drag with upper-fluid}} - \underbrace{\rho_f h_f g \sin \theta \mathbf{e}_x}_{\text{gravity}}. \end{aligned} \quad (2.14c)$$

where the coefficient k_f and the effective viscosity¹ η_e are

$$k_f = m_f \frac{\rho h_m \rho_f h_f}{\rho h_m + \rho_f h_f} |u_f - V_m| \quad \text{and} \quad \eta_e = \eta_f \left(1 + \frac{5}{2}\varphi\right). \quad (2.15)$$

with m_f a constant coefficient [49]. The excess pore pressure $p_{f_m}^e$ appears in the depth-averaged value of $\nabla p_{f_m}^e$:

$$\overline{\nabla p_{f_m}^e} = \frac{1}{h_m} \left(\nabla (h_m \overline{p_{f_m}^e}) + (p_{f_m}^e)_{|b} \nabla b \right). \quad (2.16a)$$

with $p_{f_m}^e$ at the bottom and the depth-averaged value of $p_{f_m}^e$ given by

$$(p_{f_m}^e)_{|b} = -\frac{\beta}{(1-\varphi)^2} \frac{h_m^2}{2} \Phi, \quad \overline{p_{f_m}^e} = -\frac{\beta}{(1-\varphi)^2} \frac{h_m^2}{3} \Phi \quad (2.16b)$$

with the drag coefficient β defined by [43]

$$\beta = (1-\varphi)^2 \frac{\eta_f}{k} \quad \text{with} \quad k = \frac{(1-\varphi)^3 d^2}{150\varphi^2}, \quad (2.17)$$

where d is the grain diameter, η_f the dynamic viscosity of the fluid and k the hydraulic permeability of the granular aggregate. Similar parameters are used in [4] (see Appendix A.4.3). The dilatancy function is defined by

$$\Phi = K \dot{\gamma} (\varphi - \varphi^{\text{eq}}), \quad (2.18)$$

and the rheological laws give

$$\begin{aligned} \varphi^{\text{eq}} &= \frac{\varphi_c}{1 + b_\varphi \mathcal{J}_\varphi^{1/2}} \quad \text{with} \quad \mathcal{J}_\varphi = \alpha_\varphi I^2 + J, \\ \mu^{\text{eq}} &= \mu_c + \frac{\Delta\mu}{1 + I_0/\mathcal{J}_\mu^{1/2}} \quad \text{with} \quad \mathcal{J}_\mu = \alpha_\mu I^2 + J, \end{aligned}$$

where $I = \frac{d \dot{\gamma}}{\sqrt{p_{s|b}/\rho_s}}$, $J = \frac{\eta_f \dot{\gamma}}{p_{s|b}}$, with $\dot{\gamma} = \frac{5|v|}{2h_m}$ and $p_{s|b} = \varphi(\rho_s - \rho_f)g \cos \theta h_m - (p_{f_m}^e)_{|b}$.

$$(2.19)$$

Owing to dilatancy, the friction coefficient is defined as

$$\mu = (\mu^{\text{eq}} + K(\varphi - \varphi^{\text{eq}}))_+. \quad (2.20)$$

The fluid transfer rate reads

$$\mathcal{V}_f = -h_m \Phi - \nabla \cdot (h_m (1 - \varphi)(u - v)). \quad (2.21)$$

The transfer of fluid momentum between the mixture and the upper fluid layer ends up in the term $((1 - \lambda_f)u + \lambda_f u_f) \rho_f \mathcal{V}_f$ in the fluid momentum equations (2.14b), (2.14c), where λ_f is a parameter describing the stress distribution between the fluid and solid phases at the interface between the layers (see Appendix A.3 for details). We define two possible choices for this arbitrary parameter

$$\lambda_f = \frac{1}{2} - \frac{1}{2} \text{sgn}(\mathcal{V}_f) \delta_f, \quad \delta_f = \begin{cases} 0 & \text{centered distribution,} \\ 1 & \text{upwind distribution.} \end{cases} \quad (2.22)$$

¹The effective shear viscosity η_e is approximated using Einstein's formula [15] to take into account the presence of granular material (see for example [11, 4, 9]), see also Appendix A.2.

As a result, if we choose $\delta_f = 0$, the fluid velocity at the interface defined by $(1 - \lambda_f)u + \lambda_f u_f$ reduces to $(u + u_f)/2$, while if we choose $\delta_f = 1$, this velocity depends on the sign of \mathcal{V}_f . In this case, if the fluid is expelled from the mixture, $\mathcal{V}_f > 0$ and $\lambda_f = 0$ so that the velocity is u . On the other hand, if the fluid is sucked into the mixture, $\mathcal{V}_f < 0$ and $\lambda_f = 1$, and the velocity is u_f . Note that, as exposed in [7], the expression (2.21) of the fluid transfer rate \mathcal{V}_f is obtained from the mass equations together with the transport of the solid volume fraction

$$\partial_t \varphi + v \cdot \nabla \varphi = -\varphi \Phi, \quad (2.23)$$

that constitutes an alternative scalar equation to be considered instead of (2.21).

2.3.2 Computation of the basal solid pressure

A first approach to compute the solid pressure at the bottom $p_{s|b}$ appearing in the granular friction term is to combine the above relations that implicitly define $p_{s|b}$. Indeed, $p_{s|b}$ depends on $p_{f_m|b}^e$ (equations (2.19)) that can be expressed as a function of Φ (equation (2.16b)), that is a function of φ^{eq} (equation (2.18)) that itself can be expressed as a function of $p_{s|b}$ (equations (2.19)). Combining these expressions, we find that $\sqrt{p_{s|b}}$ is the positive root of the third order polynomial,

$$\begin{aligned} & (\sqrt{p_{s|b}})^3 + A_2(\sqrt{p_{s|b}})^2 \\ & - (\varphi(\rho_s - \rho_f)g \cos \theta h_m + A_1(\varphi - \varphi_c))(\sqrt{p_{s|b}}) - A_2(\varphi(\rho_s - \rho_f)g \cos \theta h_m + \varphi A_1) = 0 \end{aligned} \quad (2.24)$$

with coefficients $A_1 = \frac{\beta}{(1 - \varphi)^2} \frac{h_m^2}{2} \dot{\gamma} K$, $A_2 = b_\varphi (\alpha_\varphi d^2 \dot{\gamma}^2 \rho_s + \eta_f \dot{\gamma})^{1/2}$. It can be shown that this equation has a unique positive root $p_{s|b} > 0$. Note that the polynomial and therefore its root are not the same when changing the rheological laws. Even if solving this equation is simple in depth-averaged models, it becomes problematic when solving multilayer models with dilatancy [17]. An alternative approach is to solve an evolution equation for the solid pressure as in [23] instead of specifying the 3D dilatancy closure $\Phi = \dot{\gamma} \tan \psi$ (equation (2.8)). This equation may be deduced from the 3D solid stress tensor equation proposed in [4] where a thermodynamic analysis of a two-phase mixture for elastic-plastic granular solid in a viscous fluid is performed to close the Jackson system. Under certain assumptions, mainly neglecting pure plastic behavior (see Appendix A.6 for details), we find the following equation for the solid pressure p_s

$$\frac{1}{B} \left(\partial_t p_s + \mathbf{v} \cdot \nabla p_s \right) = -\nabla \cdot \mathbf{v} + \dot{\gamma} \tan \psi, \quad (2.25)$$

where $B = \frac{E}{3(1-2\nu)}$ is the elastic bulk modulus of the solid (here the grains), and E and ν are the Young modulus and the Poisson ratio, respectively. Typical values for glass beads are $E = 70 \times 10^9 \text{Pa}$ and $\nu = 0.2$, corresponding to a solid bulk modulus $B = 38.9 \times 10^9 \text{Pa}$, and for sand are $E = 100 \times 10^6 \text{Pa}$ and $\nu = 0.4$, corresponding to a solid bulk modulus $B = 16.6 \times 10^7 \text{Pa}$ [20, 37]. Note that (2.25) reduces to the 3D dilatancy closure $\Phi = \dot{\gamma} \tan \psi$ when B tends to infinity. Using classical asymptotic assumptions and the depth-averaging process detailed in Appendix A.6, we obtain the following equation for the solid pressure at the bottom $p_{s|b}$

$$\partial_t p_{s|b} + v \cdot \nabla p_{s|b} = \frac{1}{4}(\rho_s - \rho_f)g \cos \theta \varphi h_m \nabla \cdot v - \frac{3}{2}B(\Phi - \dot{\gamma} \tan \psi). \quad (2.26)$$

We still need to define Φ , which can be easily obtained by using the expression of the excess pore pressure in (2.16b) and $p_{s|b}$ in (2.19) as follows

$$\Phi = -\frac{2(1 - \varphi)^2}{\beta h_m^2} (p_{f_m}^e)_{|b}, \quad \text{with} \quad (p_{f_m}^e)_{|b} = -\left(p_{s|b} - h_m \varphi (\rho_s - \rho_f) g \cos \theta \right).$$

We will compare these two approaches in the numerical tests in section 5.

2.4 Origin and impact of dilatancy in mixture models

How dilatancy is accounted for in depth-averaged mixture models is somewhat hidden since it involves a motion in the z -direction perpendicular to the slope, which is assumed to be small in these shallow models. The dilatancy law Φ clearly appears in the mass equations describing mass exchange in the systems (2.12), (2.23), taking into account (2.21).

2.4.1 Dilatancy and pore fluid pressure

Dilatancy is also present in the momentum equation through the excess pore pressure at the bottom $(p_{f_m}^e)_{|b}$ (equation (2.16b)), which represents the non-hydrostatic part of the pore fluid pressure p_{f_m} in our model. It is very sensitive to contraction/dilation of the granular phase and impacts in turn the rheology of the fluidized granular material. Indeed, $(p_{f_m}^e)_{|b}$ appears in the solid pressure at the bottom $p_{s|b}$ together with a hydrostatic term including buoyancy,

$$p_{s|b} = \varphi(\rho_s - \rho_f)g \cos \theta h_m - (p_{f_m}^e)_{|b}, \quad (2.27)$$

$p_{s|b}$ being directly involved in the friction law on the right-hand side of (2.14a). The excess pore pressure $p_{f_m}^e$ is generated by the normal displacement produced by the dilation-contraction of the granular material saturated by the fluid and is originally defined as²

$$p_{f_m}^e = \frac{\beta}{1 - \varphi} \int_z^{b+h_m} (u^z - v^z)(z') dz', \quad (2.28)$$

where u^z and v^z represent the fluid and solid velocities respectively, in the direction normal to the inclined reference plane (see figure 1). It appears as a non-hydrostatic contribution in the solid and fluid pressures in the mixture (see Section 3.4 in [7] for details). From this definition we see that the excess pore pressure is negative if the granular material goes up with respect to the fluid ($v^z > u^z$) in the case of dilation ($\Phi > 0$) and is positive ($v^z < u^z$) in the opposite case of contraction ($\Phi < 0$). As only downslope velocities are considered in our shallow depth-averaged model, we replace the normal velocities (u^z, v^z) by the downslope velocities (u, v) using the dilatancy closure equation $\text{div } \mathbf{v} = \Phi$, leading to

$$u^z - v^z = -\frac{z - b}{1 - \varphi} \left(\Phi + \nabla \cdot ((1 - \varphi)(u - v)) \right) + (u - v) \cdot \nabla b + O(\epsilon^3),$$

with ϵ the ratio between the characteristic thickness and downslope extension of the flow, which is assumed to be small in shallow models. The pore pressure at the bottom thus becomes

$$(p_{f_m}^e)_{|b} = \frac{\beta}{1 - \varphi} \left(-\frac{1}{2} \frac{h_m^2}{1 - \varphi} \Phi - \frac{1}{2} \frac{h_m^2}{1 - \varphi} \nabla \cdot ((1 - \varphi)(u - v)) + h_m (u - v) \cdot \nabla b + O(\epsilon^4) \right).$$

Interestingly, the dilatancy effects remain in the system whether the downslope velocities u, v are the same or not. As proposed in [7], a high drag coefficient, $\beta \sim \epsilon^{-1}$, implies a small velocity difference $u - v \sim \epsilon$, so that, at order ϵ^2 , we obtain the values of $(p_{f_m}^e)_{|b}$ and $\overline{p_{f_m}^e}$ used in our model (equation (2.16b)). Using equation (2.18), the excess pore fluid pressure at the bottom thus reads

$$(p_{f_m}^e)_{|b} = -75 \frac{\eta_f}{d^2} \frac{\varphi^2}{(1 - \varphi)^3} (\varphi - \varphi^{\text{eq}}) K \frac{5}{2} h_m |v|. \quad (2.29)$$

²see equation 3.45 in [7] and Section 3.5 in that paper for more details.

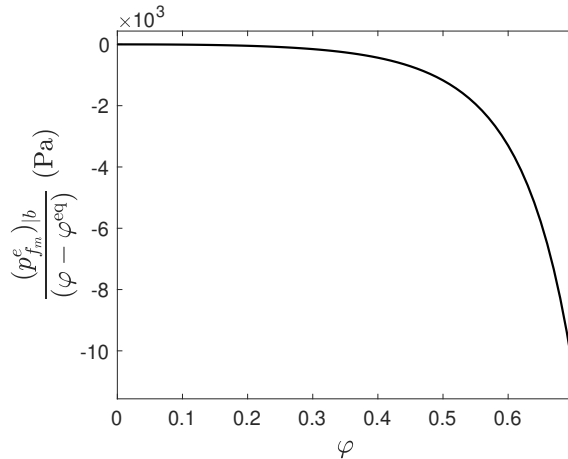


Figure 2: Illustration of the values of $(p_{f_m}^e)_b/(\varphi - \varphi^{eq})$ defined in (2.29) as a function of φ for the parameters $\eta_f = 9.8 \times 10^{-3}$ Pa s, $d = 160 \mu\text{m}$, $K = 4.09$, $h_m = 5$ mm, $v = 0.4$ mm/s taken from [7]. Note that in [7], $\varphi - \varphi^{eq} \simeq 10^{-2}$.

As a result, the excess pore fluid pressure at the bottom directly depends on the deviation from the critical state ($\varphi - \varphi^{eq}$) and in particular on its sign. If $\varphi > \varphi^{eq}$, the granular phase dilates and the excess pore pressure is negative and vice versa. In particular, the excess pore pressure is equal to zero in steady flows where $\varphi = \varphi^{eq}$, *i.e.* in the critical state. The absolute value of the excess pore fluid pressure increases as the viscosity of the fluid and the downslope solid flux increase and it decreases with increasing grain diameter as a result of higher permeability. To illustrate this, figure 2 shows $(p_{f_m}^e)_b/(\varphi - \varphi^{eq})$ as a function of φ for values of the parameters taken from [7].

2.4.2 Dilatancy and fluid transfer rate

Another key quantity in debris flow models with dilatancy is the fluid transfer rate \mathcal{V}_f between the mixture and upper fluid layers. The fluid mass transfer appears in the mass conservation equation (2.12). When $\mathcal{V}_f > 0$, the fluid is expelled from the mixture region towards the fluid-only layer as depicted in figure 1, and vice versa. This fluid transfer rate is directly related to the dilatancy of the granular phase by (2.21) that leads, owing to equations (2.8) and (2.9), to

$$\mathcal{V}_f = -h_m \dot{\gamma} K (\varphi - \varphi^{eq}) - \nabla \cdot (h_m (1 - \varphi)(u - v)). \quad (2.30)$$

When $\varphi > \varphi^{eq}$, the granular phase dilates and the first term in the fluid transfer rate is negative, which means that the fluid is sucked from the upper fluid layer into the mixture (figure 1), and vice versa. Note that the second term in equation (2.30) shows that, in principle, the fluid can still be transferred from one layer to the other when $\varphi = \varphi^{eq}$, as long as $u - v \neq 0$. However, this situation is hardly ever achieved since the time scale for u and v to be equal due to drag is much shorter than the time scale to reach the critical state (see [7]).

2.4.3 Relation between the key variables

It is worth pointing out that the key variables describing the deviation to the critical state (compaction/dilatation) in the model are all related to dilatation angle vis $\tan \psi$ since

$$\tan \psi = -(p_{f_m}^e)_b * \frac{2(1 - \varphi)^2}{\dot{\gamma} \beta h_m^2} = \mu - \mu^{eq} = K (\varphi - \varphi^{eq}) = \frac{\text{div } \mathbf{v}}{\dot{\gamma}}. \quad (2.31)$$

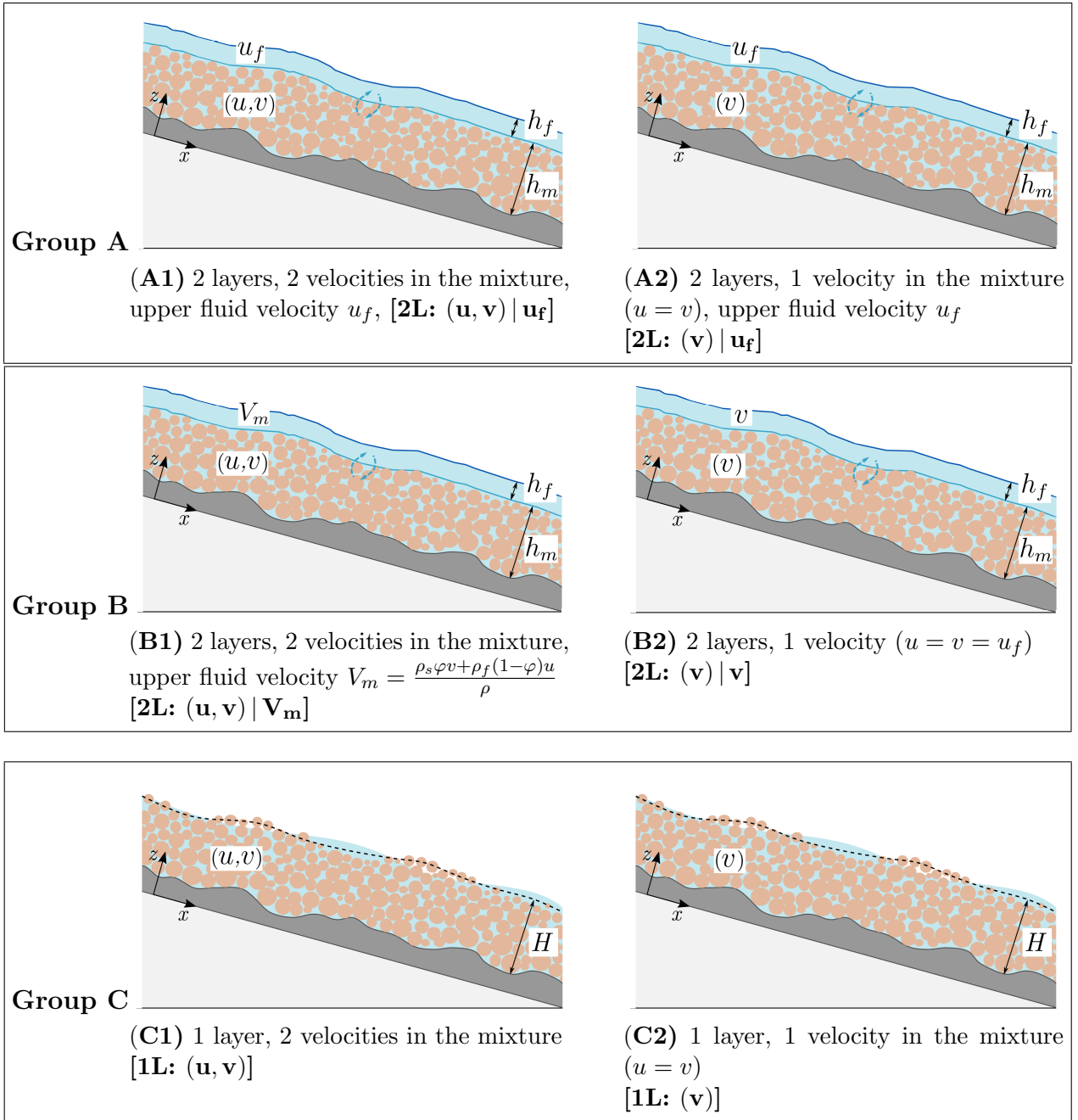


Figure 3: (A1) Flow configuration and notations for the full two-layer model with three velocities: the fluid and solid velocities in the mixture u and v and the velocity of the upper fluid layer u_f [7]. The derived simplified models are (A2), the same as (A1) except that the solid and fluid velocities in the mixture are assumed to be the same ($u = v$), (B1), the same as (A1) except that the velocity of the upper fluid layer is assumed to be the mean velocity of the mixture ($u_f = V_m$), (B2), the same as (A1) except that all the velocities are assumed to be the same ($u = v = u_f$), (C1), a one-layer model with a virtual thickness H , a solid velocity v , and a fluid velocity u , (C2) the same as (C1) but with identical velocities for the solid and fluid phases ($u = v$).

3 Simplest one-velocity models

We are going to introduce several simplified models, sketched in figure 3. They are derived from the full two-layer and three-velocity model (A1) described in Section 2.3. We will present here only the two simplest models that involve only one velocity: (i) the two-layer model (B2), (ii) the one-layer model with a virtual thickness (C2). The two-layer model with a different velocity for the mixture and the upper fluid layer (A2) was presented in [14] and is given in Appendix F.2.

3.1 Two-layer model with one velocity (B2)

3.1.1 System of equations

The procedure to obtain this simplified model is as follows. A key assumption is that we consider a high friction coefficient β between the solid and fluid phases in the mixture and a high friction coefficient k_f between the layers. This results in a single downslope velocity for the whole system

$$u = v = u_f.$$

We keep the notation v for the single velocity (figure 3B2). In this two-layer model, the system has four unknowns h_m, h_f, φ , and v and is described by the following equations (remember that $\rho = \rho_s\varphi + \rho_f(1 - \varphi)$): The total and upper fluid layer mass conservation equations,

$$\partial_t(\rho h_m + \rho_f h_f) + \nabla \cdot ((\rho h_m + \rho_f h_f)v) = 0, \quad (3.1a)$$

$$\partial_t(\rho_f h_f) + \nabla \cdot (\rho_f h_f v) = \rho_f \mathcal{V}_f, \quad (3.1b)$$

the volume fraction equation

$$\partial_t \varphi + v \cdot \nabla \varphi = -\varphi \Phi, \quad (3.1c)$$

and the total momentum conservation equation

$$\begin{aligned} & \partial_t((\rho h_m + \rho_f h_f)v) + \nabla \cdot ((\rho h_m + \rho_f h_f)v \otimes v) + g \cos \theta \nabla \left(\rho \frac{h_m^2}{2} + \rho_f \frac{h_f^2}{2} + \rho_f h_m h_f \right) \\ & = -g \cos \theta (\rho h_m + \rho_f h_f) \nabla b - g \sin \theta (\rho h_m + \rho_f h_f) \mathbf{e}_x \\ & \quad - \mu \operatorname{sgn}(v) \left((\rho - \rho_f) g \cos \theta h_m - (p_{f_m}^e)_{|b} \right) - \frac{5 \eta_e (1 - \varphi)}{2 h_m} v. \end{aligned} \quad (3.1d)$$

The closures for this model are adapted from (2.16)-(2.22), giving

$$(p_{f_m}^e)_{|b} = -\frac{\beta}{(1 - \varphi)^2} \frac{h_m^2}{2} \Phi, \quad \beta = \frac{150 \eta_f \varphi^2}{(1 - \varphi) d^2}, \quad (3.2a)$$

and the dilatancy relations

$$\mu = (\mu^{\text{eq}} + K(\varphi - \varphi^{\text{eq}}))_+, \quad \mathcal{V}_f = -h_m \Phi, \quad \Phi = \dot{\gamma} K(\varphi - \varphi^{\text{eq}}), \quad (3.2b)$$

with rheological laws

$$\begin{aligned} \varphi^{\text{eq}} &= \frac{\varphi_c}{1 + b_\varphi \mathcal{J}_\varphi^{1/2}} \quad \text{with} \quad \mathcal{J}_\varphi = \alpha_\varphi I^2 + J, \\ \mu^{\text{eq}} &= \mu_c + \frac{\Delta \mu}{I_0 + \mathcal{J}_\mu^{1/2}} \mathcal{J}_\mu^{1/2} \quad \text{with} \quad \mathcal{J}_\mu = \alpha_\mu I^2 + J, \\ \text{where} \quad I &= \frac{d \dot{\gamma}}{\sqrt{p_{s|b}/\rho_s}}, \quad J = \frac{\eta_f \dot{\gamma}}{p_{s|b}}, \quad \text{and} \quad \dot{\gamma} = \frac{5 |v|}{2 h_m}, \quad p_{s|b} = (\rho - \rho_f) g \cos \theta h_m - (p_{f_m}^e)_{|b}. \end{aligned} \quad (3.2c)$$

This model preserves the total mass (equation (3.1a)), the total volume, and the mass and volume of each phase, as we will briefly prove now. Equations (2.1) and (2.23) give the evolution equation for the bulk density,

$$\partial_t \rho + v \cdot \nabla \rho = -(\rho - \rho_f) \Phi. \quad (3.3)$$

We subtract (3.1b) from (3.1a) and use $\mathcal{V}_f = -h_m \Phi$, then further subtract h_m times (3.3). We obtain the equation for the mixture volume,

$$\partial_t h_m + \nabla \cdot (h_m v) = h_m \Phi. \quad (3.4)$$

Now combining this last equation with (3.1b) we obtain the total volume conservation equation

$$\partial_t (h_m + h_f) + \nabla \cdot ((h_m + h_f) v) = 0. \quad (3.5)$$

The solid and fluid volumes are calculated straightforward as a combination of (3.1b) and (3.3) with (3.4),

$$\partial_t (\varphi h_m) + \nabla \cdot (\varphi h_m v) = 0, \quad \partial_t ((1 - \varphi) h_m + h_f) + \nabla \cdot (((1 - \varphi) h_m + h_f) v) = 0. \quad (3.6)$$

Since the phase densities ρ_s, ρ_f are constant, we equivalently obtain mass conservation for each phase by multiplying these two equations by ρ_s and ρ_f respectively. The sum of these two gives (3.1a), whereas the sum of (3.6) gives (3.5).

3.1.2 Model (B2) expressed as a function of the virtual thickness

Let us define the so-called *virtual thickness* (see figure 4 for a schematic representation) as

$$H = \frac{\rho h_m + \rho_f h_f}{\rho} = h_m + \frac{\rho_f}{\rho} h_f. \quad (3.7)$$

Then ρH represents the total mass that is conserved (see equation (3.1a)). This quantity is conserved but part of the solid or fluid may pass through this virtual surface during dilation or contraction. Since $\rho \geq \rho_f$ according to (2.1), we have $h_m \leq H \leq h_m + h_f$. The above definition of H was introduced by Iverson and George [23] as the height of the so-called “virtual free surface”. Figure 4 shows schematically the virtual thickness and how it changes in the case of dilation and compaction. As the granular phase dilates, the solid volume fraction φ decreases, thus the bulk density ρ decreases owing to (2.1). Hence H increases as long as the mass is conserved. On the other hand, during compaction ρ increases with φ and then H decreases. As mentioned before, our system does not allow $h_f < 0$ and therefore there is always a small layer of water above the mixture, or in the limit case where $h_f = 0$, we obtain $H = h_m$. We additionally introduce

$$\Delta_H = H - h_m. \quad (3.8)$$

Thus Δ_H represents the distance of the virtual surface ($b + H$) to the mixture surface $b + h_m$ and $h_f - \Delta_H$ represents the difference between the real free surface ($b + h_m + h_f$) and the virtual surface ($b + H$). This is illustrated in figure 5, where for clarity we use the same schematic view as in figure 4). Note that $\Delta_H = \frac{\rho_f}{\rho} h_f$ so that for typical values of $0.3 < \varphi < 0.6$, we obtain $0.5h_f < \Delta_H < 0.7h_f$.

Taking into account these expressions, the mixture model (3.1)-(3.2) is equivalently written for unknowns H, Δ_H, φ, v as

$$\partial_t (\rho H) + \nabla \cdot (\rho H v) = 0, \quad (3.9a)$$

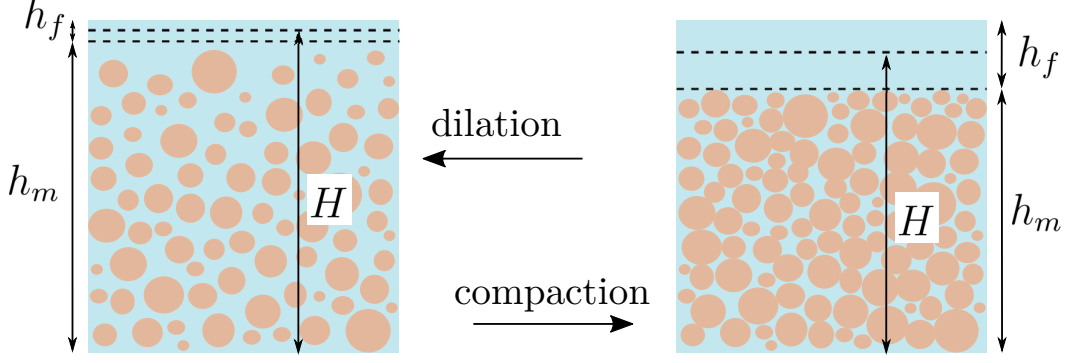


Figure 4: Schematic view showing the virtual thickness H introduced in [23] and defined by (3.7) as well as the behavior of the system experiencing dilation or compaction.

$$\partial_t(\rho\Delta_H) + \nabla \cdot (\rho\Delta_H v) = \rho_f \mathcal{V}_f, \quad (3.9b)$$

$$\partial_t\varphi + v \cdot \nabla\varphi = -\varphi\Phi, \quad (3.9c)$$

$$\begin{aligned} \partial_t(\rho H v) + \nabla \cdot (\rho H v \otimes v) + g \cos\theta \nabla \left(\frac{1}{2} \rho \left(H^2 + \frac{\rho - \rho_f}{\rho_f} \Delta_H^2 \right) \right) \\ = -\rho H g \cos\theta \nabla b - \rho H g \sin\theta \mathbf{e}_x - \mu \operatorname{sgn}(v) \left((\rho - \rho_f) g \cos\theta (H - \Delta_H) - (p_{f_m}^e)_{|b} \right)_+ - \frac{5}{2} \frac{\eta_e (1 - \varphi)}{H - \Delta_H} v. \end{aligned} \quad (3.9d)$$

with

$$(p_{f_m}^e)_{|b} = -\frac{\beta}{(1 - \varphi)^2} \frac{(H - \Delta_H)^2}{2} \Phi, \quad \beta = \frac{150\eta_f \varphi^2}{(1 - \varphi)d^2}, \quad (3.10a)$$

the dilatancy laws

$$\mu = (\mu^{\text{eq}} + K(\varphi - \varphi^{\text{eq}}))_+, \quad \mathcal{V}_f = -(H - \Delta_H)\Phi, \quad \Phi = \dot{\gamma} K(\varphi - \varphi^{\text{eq}}), \quad (3.10b)$$

and the rheological laws

$$\begin{aligned} \varphi^{\text{eq}} &= \frac{\varphi_c}{1 + b_\varphi \mathcal{J}_\varphi^{1/2}} \quad \text{with} \quad \mathcal{J}_\varphi = \alpha_\varphi I^2 + J, \\ \mu^{\text{eq}} &= \mu_c + \frac{\Delta\mu}{I_0 + \mathcal{J}_\mu^{1/2}} \mathcal{J}_\mu^{1/2} \quad \text{with} \quad \mathcal{J}_\mu = \alpha_\mu I^2 + J, \\ \text{where} \quad I &= \frac{d\dot{\gamma}}{\sqrt{p_{s|b}/\rho_s}}, \quad J = \frac{\eta_f \dot{\gamma}}{p_{s|b}}, \\ \text{and} \quad \dot{\gamma} &= \frac{5}{2} \frac{|v|}{H - \Delta_H}, \quad p_{s|b} = (\rho - \rho_f) g \cos\theta (H - \Delta_H) - (p_{f_m}^e)_{|b}. \end{aligned} \quad (3.10c)$$

With the aim to compare our model to the Iverson-George model [23, 18], we write the pressure appearing in the Coulomb friction term as

$$p_{s|b} = (\rho - \rho_f) g \cos\theta (H - \Delta_H) - (p_{f_m}^e)_{|b} = \rho g \cos\theta H - (p_{f_m}^e)_{|b}, \quad (3.11)$$

with the pore fluid pressure at the bottom (see equations (3.44) and (4.31) in [7])

$$(p_{f_m}^e)_{|b} = \rho_f g \cos\theta \left(H + \frac{\rho - \rho_f}{\rho_f} \Delta_H \right) + (p_{f_m}^e)_{|b}. \quad (3.12)$$

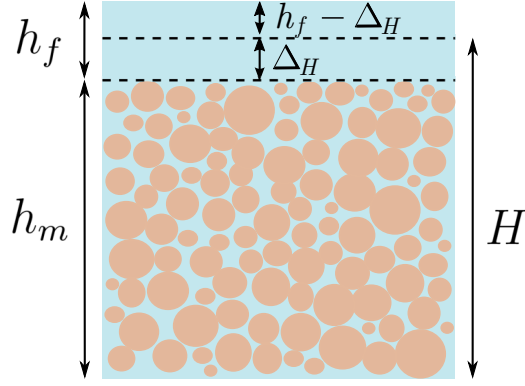


Figure 5: Virtual thickness H introduced in (3.7) and associated thickness Δ_H in (3.8)

3.2 One-layer model with one velocity (C2)

In order to derive a simplified model with only one thickness and one velocity, as in the Iverson-George model [23, 18], we keep the virtual thickness H as the only thickness in the model. We thus neglect the terms involving Δ_H in the system (3.9) by assuming

$$\Delta_H = H - h_m \ll H. \quad (3.13)$$

According to (3.7), this means that h_f is small and that the virtual thickness H is very close to the mixture thickness h_m (figure 5). This assumption is appropriate to describe debris flows, where the upper fluid layer is expected to be thin, but not at all to describe submarine landslides, where the thickness of the fluid layer is large, even though such a model has been used for submarine landslides [19]. Furthermore, with assumption (3.13), equation (3.9b) for h_f tells us that the dilatancy Φ must be small too, since $\mathcal{V}_f = -h_m\Phi$. In spite of this, we keep it in the system in order to conserve the dilatancy effect (explicitly appearing in the equation for φ and in the excess pore pressure $p_{f_m}^e$). As a result, the oversimplified system (3.14) below is only valid when dilatancy is small $|\Phi| \ll 1$. Our single layer mixture model thus reads

$$\partial_t(\rho H) + \nabla \cdot (\rho H v) = 0, \quad (3.14a)$$

$$\partial_t \varphi + v \cdot \nabla \varphi = -\varphi \Phi^*, \quad (3.14b)$$

$$\begin{aligned} & \partial_t(\rho H v) + \nabla \cdot (\rho H v \otimes v) + g \cos \theta \nabla \left(\rho \frac{H^2}{2} \right) \\ & = -\rho H g \cos \theta \nabla b - \rho H g \sin \theta \mathbf{e}_x - \mu^* \operatorname{sgn}(v) (\rho g \cos \theta H - (p_{f_m}^e)_{|b}^*)_+ - \frac{5}{2} \frac{\eta_e (1 - \varphi)}{H} v. \end{aligned} \quad (3.14c)$$

The critical-state solid volume fraction and friction coefficient, the shear rate and the excess pore pressure depend on the mixture thickness $h_m = H - \Delta_H$. Condition (3.13) implies that h_m can be replaced by H . To point out this modification, we will add a “star” notation when h_m is replaced by H in the expressions. These simplifications induce significant differences with the previous model (3.1)-(3.2), which will be quantified in the numerical tests (see section 3.3 below for a deeper analysis). The pore fluid pressure at the base becomes

$$(p_{f_m}^e)_{|b}^* = \rho_f g \cos \theta H + (p_{f_m}^e)_{|b}^*, \quad \text{with} \quad (p_{f_m}^e)_{|b}^* = -\frac{\beta}{(1 - \varphi)^2} \frac{H^2}{2} \Phi^*, \quad \beta = \frac{150 \eta_f \varphi^2}{(1 - \varphi) d^2}. \quad (3.15a)$$

The dilatancy and rheological laws involve

$$\mu^* = (\mu^{\text{eq}*} + K(\varphi - \varphi_c^{\text{eq}*}))_+, \quad \Phi^* = \dot{\gamma}^* K(\varphi - \varphi_c^{\text{eq}*}), \quad (3.15b)$$

and

$$\begin{aligned} \varphi^{\text{eq}*} &= \frac{\varphi_c}{1 + b_\varphi (\mathcal{J}_\varphi^*)^{1/2}} \quad \text{with} \quad \mathcal{J}_\varphi^* = \alpha_\varphi (I^*)^2 + J^*, \\ \mu^{\text{eq}*} &= \mu_c + \frac{\Delta\mu}{I_0 + (\mathcal{J}_\mu^*)^{1/2}} (\mathcal{J}_\mu^*)^{1/2} \quad \text{with} \quad \mathcal{J}_\mu^* = \alpha_\mu (I^*)^2 + J^*, \\ \text{where} \quad I^* &= \frac{d\dot{\gamma}^*}{\sqrt{p_{s|b}^*/\rho_s}}, \quad J^* = \frac{\eta_f \dot{\gamma}^*}{p_{s|b}^*}, \\ \text{and} \quad \dot{\gamma}^* &= \frac{5|v|}{2H}, \quad p_{s|b}^* = (\rho - \rho_f)g \cos \theta H - (p_{f_m}^e)_{|b}^*. \end{aligned} \quad (3.15c)$$

3.3 Impact of considering a virtual thickness

Let us analyze how the assumption of a virtual thickness H (condition (3.13)) instead of considering two layers impacts the pressure at the bottom that appears in the Coulomb-type friction. The solid pressure at the bottom $p_{s|b}$ in the original two-layer one-velocity model involves the mixture thickness h_m while its approximate value $p_{s|b}^*$ involves H and thus part of the upper fluid layer (see figure 5). We can explicitly estimate the difference (in blue) between the original and approximate solid basal pressure terms (assuming $\Phi^* \simeq \Phi$)

$$\begin{aligned} p_{s|b}^* &= \rho g \cos \theta H - (p_{f_m}^e)_{|b}^* = (\rho - \rho_f)g \cos \theta H - (p_{f_m}^e)_{|b}^* \\ &= p_{s|b} + (\rho - \rho_f)g \cos \theta \Delta_H + \frac{\beta}{(1 - \varphi)^2} \frac{H^2 - h_m^2}{2} \Phi \\ &= p_{s|b} + \Delta_H \left((\rho - \rho_f)g \cos \theta + \frac{\beta}{(1 - \varphi)^2} \frac{H + h_m}{2} \Phi \right). \end{aligned}$$

This term, negligible under assumption (3.13), is positive since $\Delta_H > 0$, thus $p_{s|b}^* > p_{s|b}$. The difference between the original shear rate $\dot{\gamma} = \frac{5|v|}{2h_m}$ and its approximation can also be written in terms of Δ_H as

$$\dot{\gamma}^* = \dot{\gamma} + \frac{5}{2}|v| \left(\frac{1}{H} - \frac{1}{h_m} \right) = \dot{\gamma} - \frac{5}{2}|v| \frac{\Delta_H}{h_m H}.$$

The additional term in blue is small under (3.13) and negative, leading to smaller inertial numbers I^* and J^* in (3.15c) and $\mu^* \leq \mu$ (with equality if $v = 0$). As a result, the increase of $p_{s|b}$ and the decrease of μ in the one-layer one-velocity model (C2) compared to the two-layer one-velocity model (B2) have opposite effects on the granular friction. This will be analyzed in the numerical tests presented in Section 5.

3.4 Comparison with the Iverson-George model

In this section we compare our oversimplified mixture model (C2) with the Iverson-George model presented in two companion papers [23] and [18].

3.4.1 The Iverson-George model

The two main characteristics of the Iverson-George model are (i) the basal pore fluid pressure called p_b calculated by solving an advection-diffusion equation (3.16d) involving the elasticity of the grains, and (ii) the idea of a virtual surface called h in their papers (see section 3.1.2).

Let us use the Iverson-George model [23, 18] with our notation, except for h and p_b (see the equivalence of notations in Appendix B). We use the subscript IG to denote particular coefficients for the Iverson-George model. The unknowns h, ρ, v, p_b obey the following equations

$$\partial_t h + \nabla \cdot (hv) = \frac{\rho - \rho_f}{\rho} D, \quad (3.16a)$$

$$\partial_t(\rho h) + \nabla \cdot (\rho hv) = 0, \quad (3.16b)$$

$$\begin{aligned} \partial_t(hv) + \nabla \cdot (hv \otimes v) + \kappa h^2 g \cos \theta \nabla \rho + \kappa \nabla \left(g \cos \theta \frac{h^2}{2} \right) + \frac{h(1 - \kappa)}{\rho} \nabla p_b \\ = -hg \cos \theta \nabla b - hg \sin \theta \mathbf{e}_x + \frac{\rho - \rho_f}{\rho} Dv - \frac{\tau_s + \tau_f}{\rho}, \end{aligned} \quad (3.16c)$$

$$\partial_t p_b + v \cdot \nabla p_b + \frac{1}{4} g \cos \theta \left((\rho_f + 3\rho) h \nabla \cdot v - \rho_f \frac{\rho - \rho_f}{\rho} D \right) = \frac{3}{2\alpha} \left(\frac{D}{h} - \dot{\gamma}_{\text{IG}} \tan \psi_{\text{IG}} \right). \quad (3.16d)$$

The terms τ_s and τ_f in the momentum equation are the solid and fluid basal shear stresses respectively, given by

$$\tau_f = (1 - \varphi) \eta_e \frac{2v}{h}, \quad \tau_s = \mu_{\text{IG}} \frac{v}{|v|} \sigma_e, \quad \mu_{\text{IG}} = \tan(\delta + \psi_{\text{IG}}), \quad (3.17a)$$

with δ the basal constant-volume friction angle of the material and σ_e the basal solid pressure

$$\sigma_e = \rho g \cos \theta h - p_b. \quad (3.17b)$$

The bottom pore fluid pressure p_b is solved in the last equation of the system. It is composed of the hydrostatic contribution and the excess pore fluid pressure p_e , giving

$$p_b = \rho_f g \cos \theta h + p_e, \quad (3.17c)$$

where p_e is an unknown related to D by

$$D = -\frac{2k_{\text{IG}}}{h\eta_e} p_e, \quad \text{with} \quad k_{\text{IG}} = k_0 e^{\frac{0.6-\varphi}{0.04}}, \quad (3.17d)$$

the hydraulic permeability of the granular aggregate and k_0 a reference permeability ($k_0 \sim 10^{-13} - 10^{-10} \text{ m}^2$, cf. [23]). The coefficient $\alpha > 0$ in the pressure equation is the elastic compressibility and κ is a lateral pressure coefficient that equals 1 when isotropy of normal stresses is assumed. The shear rate $\dot{\gamma}$ is approximated by Iverson and George as (see equations 4.24 in [23] or 2.14 in [18])

$$\dot{\gamma}_{\text{IG}} = \frac{2|v|}{h}. \quad (3.17e)$$

The closures for the dilatancy law are given as

$$\tan \psi_{\text{IG}} = \varphi - \varphi_{\text{IG}}^{\text{eq}}, \quad \varphi_{\text{IG}}^{\text{eq}} = \frac{\varphi_c}{1 + \sqrt{N}}, \quad N = \frac{J}{1 + J \text{St}} = \frac{J}{1 + I^2}, \quad (3.17f)$$

where the inertial, viscous and Stokes numbers I, J , and St are defined in (2.4)-(2.5). Note that the basal solid pressure is denoted here by σ_e instead of $p_{s|b}$.

Note also that in [18], where the model is numerically solved, the authors neglect the term $\kappa h^2 g \cos \theta \nabla \rho$ in the momentum equation (3.16c) under the assumption of a small longitudinal gradient of ρ (see equation A.2 in [18]). In fact, this term does not appear in our system, as

will be seen later. It is worth mentioning that the Iverson-George model does not give any information on the conservation of the solid and the fluid mass or volume since h is not a real surface. Even if the total mass ρh is conserved, the solid or the fluid may pass through the virtual surface h during dilation or contraction (cf. [23]), as in our one-layer one-velocity model (C2). It follows that the quantities $\rho_s \varphi h$ and $\rho_f (1 - \varphi) h$ do not represent the total solid and fluid mass respectively and are not conserved in the Iverson-George model. Therefore, from equations (3.16a)-(3.16b) we obtain (see equations 4.7 and 4.8 in [23])

$$\partial_t(\rho_s \varphi h) + \nabla \cdot (\rho_s \varphi h v) = -\frac{\rho_s \rho_f}{\rho} \varphi D, \quad \partial_t(\rho_f (1 - \varphi) h) + \nabla \cdot (\rho_f (1 - \varphi) h v) = \frac{\rho_s \rho_f}{\rho} \varphi D. \quad (3.18)$$

On the other hand, our two-layer one-velocity model (B2) in (3.1) naturally accounts for the liquid mass flux expelled or sucked from/by the mixture through the quantity $\mathcal{V}_f = -h_m \Phi$ and conserves the total solid and fluid masses.

3.4.2 Comparison with our one-layer one-velocity model (C2)

We obtain our oversimplified mixture model (C2) in (3.14) from the Iverson-George model (3.16) with small differences detailed below, under the following assumptions (see details of the calculation in Appendix C.1):

- * $\kappa = 1$ (isotropy of normal stresses),
- * $\alpha \rightarrow 0$ (grain elasticity is neglected),
- * $h = H$,
- * $\nabla \rho \ll 1$, that leads to neglecting $\kappa h^2 g \cos \theta \nabla \rho$ in the momentum equation, as done by Iverson and George [18].

When the grain elasticity α is neglected ($\alpha \rightarrow 0$), we obtain from equation (3.16d) that

$$\frac{D}{h} = \dot{\gamma}_{\text{IG}} \tan \psi_{\text{IG}} = \frac{2|v|}{h} (\varphi - \varphi_{\text{IG}}^{\text{eq}})$$

where we used (3.17e) and (3.17f). Our dilatancy law (2.8)-(2.9) gives

$$\Phi = \dot{\gamma} \tan \psi = \frac{5}{2} \frac{|v|}{h_m} K (\varphi - \varphi^{\text{eq}}).$$

When $h_m \simeq H = h$ and if φ^{eq} would have been equal to $\varphi_{\text{IG}}^{\text{eq}}$, we would have

$$D \equiv h \Phi, \quad (3.19)$$

for the particular value $K = \frac{4}{5}$. In this case, the excess pore pressure p_e of Iverson and George in (3.17d) and our value $p_{f_m}^e$ in (2.16b) would be the same if we further assume $\eta_f = \eta_e$, as done in their numerical application, and $k = k_{\text{IG}}$. In figure 6, we show the huge differences between the values of the hydraulic permeability in the two models as a function of φ (see figure 5 in [23] for typical values). Its impact will be shown in test 2 of section 5. In the Iverson-George model, the viscous basal shear stress for the fluid τ_f in (3.17a) would be the same as in our model (see last term of equation (3.14c)) if we would have approximated the shear strain rate in the same way (compare equation (3.17e) with equation (3.2c)). A similar term τ_f is considered in the work of Pailha-Pouliquen [43] (see their equation 3.16) and in our work on numerical simulation

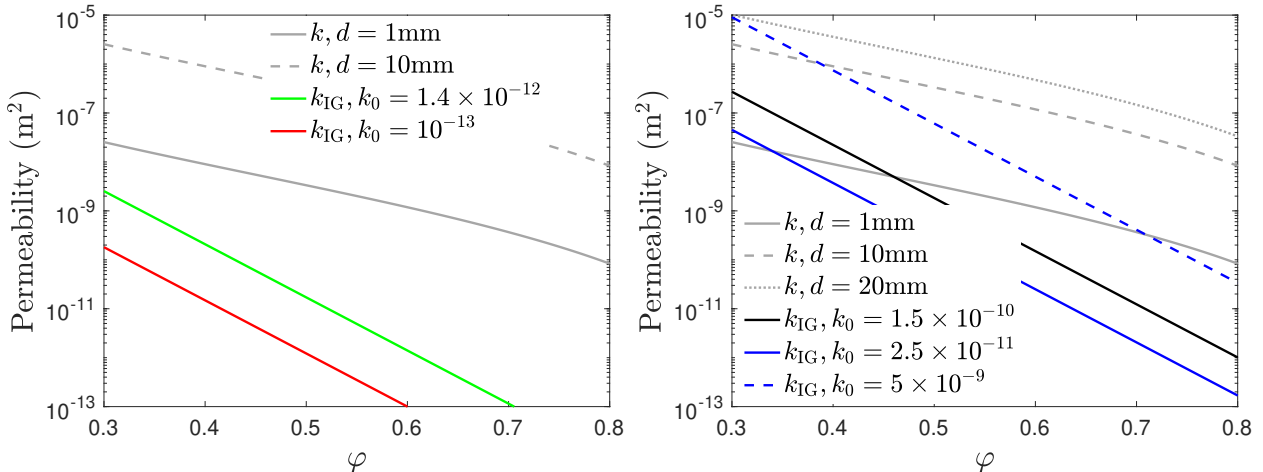


Figure 6: Comparison of the hydraulic permeability as a function of φ for the proposed model and for the Iverson-George model, given respectively by $k = \frac{(1-\varphi)^3 d^2}{150\varphi^2}$ m² in (2.17) and $k_{\text{IG}} = k_0 e^{\frac{0.6-\varphi}{0.04}}$ m² in (3.17d), in a logarithmic scale for the y -axis. Values are taken from figure 5 in [23] for different debris flows: left corresponds to real debris flows MSH and OSC where $d < 16$ mm, $k_0 = 1.4 \times 10^{-12}$ m², $k_0 = 10^{-13}$ m² and right corresponds to experiments SG and SGM where $d \sim 0.4 - 20$ mm, $k_0 = 1.5 \times 10^{-10}$ m² for SG, and $k_0 = 2.5 \times 10^{-11}$ m² (measured) and $k_0 = 5 \times 10^{-9}$ m² (for simulation in [18]) for SGM.

of immersed granular collapses (see equation 5.4 in [7]).

Other important differences between our model and the Iverson-George model are related to the rheology, as detailed in Appendix C.1). For our model, the rheology is given in (2.7), (2.9), and for Iverson-George in (3.17f). If we linearize the tangent in the friction coefficient given by (3.17a), it reads

$$\mu_{\text{IG}} = \tan(\delta + \psi_{\text{IG}}) \simeq \tan \delta + \tan \psi_{\text{IG}}.$$

The friction coefficient in the critical state $\mu_c = \tan \delta$ is thus constant while it depends on the inertial and viscous numbers in our model ($\mu^{\text{eq}}(\mathcal{J}_\mu)$) (see equations (2.7) and (2.11)). Regarding the dilatancy, we obtain $\tan \psi_{\text{IG}}$ in (3.17f) if we set $K = 1$ in (2.9). Furthermore, the expression of the effective volume fraction $\varphi_{\text{IG}}^{\text{eq}}$ is similar to the one proposed here in (2.7), but the dimensionless number differs: N here and $\mathcal{J}_\varphi = \alpha_\varphi I^2 + J$ in our model (see table (3)). The dependence on J is linear in both \mathcal{J}_φ and N , whereas the dependence on I^2 is completely different. In figure 7, we show the behavior of $\varphi_{\text{IG}}^{\text{eq}}$ and φ^{eq} for different values of J . Differences of more than 10% are observed, in particular for high values of I and J , as will be further analyzed in the numerical tests. Finally, concerning the pressure equation (3.16d), we can obtain it by depth-averaging equation (2.25), for $\alpha = 1/B$ under several assumptions detailed in section C.2. Among them, the most relevant are the specification of a linear profile for the vertical velocity and a quadratic profile for the pore pressure.

4 Models with two velocities in the mixture

4.1 Two-layer model with two velocities in the mixture (B1)

The model (B1) (see figure 3) is a simplification of the original full model (A1) (section 2.3) that is obtained by assuming that the upper fluid layer is no longer free but moves with the velocity

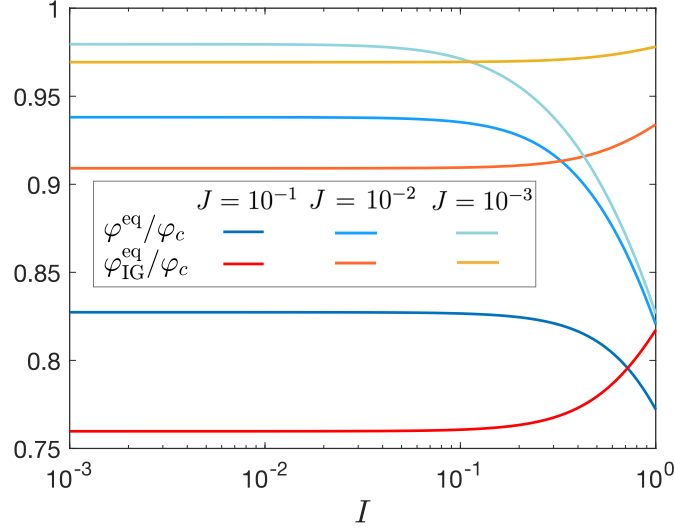


Figure 7: Comparison of the effective volume fractions proposed here φ^{eq} in (2.7) and by Iverson and George $\varphi_{\text{IG}}^{\text{eq}}$ in (3.17f) as a function of the inertial number I for fixed $J = 10^{-1}, 10^{-2}, 10^{-3}$ and with values $\alpha_\varphi = 0.1, a_\varphi = 0.66$ for φ^{eq} in (2.7).

	Iverson-George model	Our mixture model
Effective fric. coeff.	$\mu_{\text{IG}}^{\text{eq}} = \mu_c = \tan \delta$ (const.)	$\mu^{\text{eq}} = \mu_c + \frac{\Delta\mu}{I_0 + \mathcal{J}_\mu^{1/2}} \mathcal{J}_\mu^{1/2},$ $\mathcal{J}_\mu = \alpha_\mu I^2 + J$
Dilatancy fric. coeff.	$\tan \psi_{\text{IG}} = \varphi - \varphi_{\text{IG}}^{\text{eq}}$ $\varphi_{\text{IG}}^{\text{eq}} = \frac{\varphi_c}{1 + \sqrt{N}}, \quad N = \frac{J}{1 + I^2}$	$\tan \psi = K(\varphi - \varphi^{\text{eq}})$ $\varphi^{\text{eq}} = \frac{\varphi_c}{1 + a\sqrt{\mathcal{J}_\varphi}}, \quad \mathcal{J}_\varphi = \alpha_\varphi I^2 + J$

Table 3: Comparison between the dilatancy and rheological laws in the Iverson-George model ((3.17a), (3.17f)) and in our models ((2.7), (2.9))

of the mixture V_m :

$$u_f = V_m \equiv \frac{\rho_s \varphi v + \rho_f (1 - \varphi) u}{\rho},$$

with ρ given by (2.1). This makes it possible to remove one velocity from the unknowns by assuming an infinite friction coefficient between the layers ($k_f \rightarrow \infty$) in the original model (2.12)-(2.21). In order to eliminate $k_f(u_f - V_m)$ in the momentum equations, we combine the fluid equations as follows: (2.14b) + $\frac{\rho_f(1-\varphi)}{\rho} \times$ (2.14c). We then write the system in a conservative form (see Appendix E for details) to obtain the following two-velocity system for unknowns h_m, h_f, φ, u, v . The mass conservation equations are the same as in the original model:

$$\partial_t(\rho_s \varphi h_m) + \nabla \cdot (\rho_s \varphi h_m v) = 0, \quad (4.1a)$$

$$\partial_t(\rho_f(1 - \varphi)h_m) + \nabla \cdot (\rho_f(1 - \varphi)h_m u) = -\rho_f \mathcal{V}_f, \quad (4.1b)$$

$$\partial_t(\rho_f h_f) + \nabla \cdot (\rho_f h_f V_m) = \rho_f \mathcal{V}_f, \quad (4.1c)$$

with the same expression of the fluid transfer rate

$$\mathcal{V}_f = -h_m \Phi - \nabla \cdot (h_m(1 - \varphi)(u - v)), \quad (4.2)$$

or alternatively the continuity equation for the solid volume fraction

$$\partial_t \varphi + v \cdot \nabla \varphi = -\varphi \Phi. \quad (4.3)$$

The momentum equations read

$$\begin{aligned} & \partial_t \left(\rho_s \varphi \left(h_m v + \frac{\rho_f h_f}{\rho} V_m \right) \right) + \nabla \cdot \left(\rho_s \varphi \left(h_m v \otimes v + \frac{\rho_f h_f}{\rho} V_m \otimes V_m \right) \right) \\ &= -g \cos \theta \nabla \left((\rho_s - \rho_f) \varphi \frac{h_m^2}{2} + \rho_f \frac{(h_m + h_f)^2}{2} \right) + g \cos \theta (\rho h_m + \rho_f h_f) \frac{\rho_f(1 - \varphi)}{\rho} \nabla (h_m + h_f) \\ & \quad - (\rho h_m + \rho_f h_f) \frac{\rho_s \varphi}{\rho} g \cos \theta \nabla b + (1 - \varphi) h_m \overline{\nabla p_{f_m}^e} + \beta h_m (u - v) \\ & \quad - \text{sgn}(v) \mu (\varphi (\rho_s - \rho_f) g \cos \theta h_m - (p_{f_m}^e)_{|b}) + \frac{\rho_s \varphi}{\rho} ((1 - \lambda_f) u + \lambda_f V_m) \rho_f \mathcal{V}_f \\ & \quad - (\rho h_m + \rho_f h_f) \frac{\rho_s \varphi}{\rho} g \sin \theta \mathbf{e}_x - \frac{\rho_f^2 \rho_s}{\rho^2} h_f V_m (\varphi \Phi + (v - V_m) \cdot \nabla \varphi), \end{aligned} \quad (4.4a)$$

$$\begin{aligned} & \partial_t \left(\rho_f (1 - \varphi) \left(h_m u + \frac{\rho_f h_f}{\rho} V_m \right) \right) + \nabla \cdot \left(\rho_f (1 - \varphi) \left(h_m u \otimes u + \frac{\rho_f h_f}{\rho} V_m \otimes V_m \right) \right) \\ &= -(\rho h_m + \rho_f h_f) \frac{\rho_f(1 - \varphi)}{\rho} g \cos \theta \nabla (b + h_m + h_f) - (1 - \varphi) h_m \overline{\nabla p_{f_m}^e} \\ & \quad - \beta h_m (u - v) - \frac{\rho_s \varphi}{\rho} ((1 - \lambda_f) u + \lambda_f V_m) \rho_f \mathcal{V}_f - \frac{5 \eta_e (1 - \varphi)}{2 h_m} u \\ & \quad - (\rho h_m + \rho_f h_f) \frac{\rho_f(1 - \varphi)}{\rho} g \sin \theta \mathbf{e}_x + \frac{\rho_f^2 \rho_s}{\rho^2} h_f V_m (\varphi \Phi + (v - V_m) \cdot \nabla \varphi). \end{aligned} \quad (4.4b)$$

The closures are again the original ones, given by equations (2.16)-(2.22) that we indicate again here for completeness. The excess pore pressure $p_{f_m}^e$ terms involve

$$\overline{\nabla p_{f_m}^e} = \frac{1}{h_m} \left(\nabla (h_m \overline{p_{f_m}^e}) + (p_{f_m}^e)_{|b} \nabla b \right), \quad (4.5a)$$

with

$$(p_{f_m}^e)_{|b} = -\frac{\beta}{(1-\varphi)^2} \frac{h_m^2}{2} \Phi, \quad \overline{p_{f_m}^e} = -\frac{\beta}{(1-\varphi)^2} \frac{h_m^2}{3} \Phi \quad (4.5b)$$

where the drag coefficient β and the dilatancy function Φ are

$$\beta = \frac{150\eta_f\varphi^2}{(1-\varphi)d^2}, \quad \Phi = K\dot{\gamma}(\varphi - \varphi^{\text{eq}}). \quad (4.6)$$

The rheological laws give

$$\begin{aligned} \varphi^{\text{eq}} &= \frac{\varphi_c}{1 + b_\varphi \mathcal{J}_\varphi^{1/2}} \quad \text{with} \quad \mathcal{J}_\varphi = \alpha_\varphi I^2 + J, \\ \mu^{\text{eq}} &= \mu_c + \frac{\Delta\mu}{I_0 + \mathcal{J}_\mu^{1/2}} \mathcal{J}_\mu^{1/2} \quad \text{with} \quad \mathcal{J}_\mu = \alpha_\mu I^2 + J, \\ \text{where} \quad I &= \frac{d\dot{\gamma}}{\sqrt{p_{s|b}/\rho_s}}, \quad J = \frac{\eta_f \dot{\gamma}}{p_{s|b}}, \\ \text{and} \quad \dot{\gamma} &= \frac{5}{2} \frac{|v|}{h_m}, \quad p_{s|b} = \varphi(\rho_s - \rho_f)g \cos \theta h_m - (p_{f_m}^e)_{|b}. \end{aligned} \quad (4.7)$$

The friction coefficient is defined as

$$\mu = (\mu^{\text{eq}} + K(\varphi - \varphi^{\text{eq}}))_+. \quad (4.8)$$

The transfer of the fluid momentum distribution parameter is given by

$$\lambda_f = \frac{1}{2} - \frac{1}{2} \text{sgn}(\mathcal{V}_f) \delta_f, \quad \delta_f = \begin{cases} 0 & \text{centered distribution,} \\ 1 & \text{upwind distribution.} \end{cases} \quad (4.9)$$

As for the full model (A1), model (B1) preserves the total mass and volume and the masses and volumes for each phase as a consequence of (4.1)-(4.3) (cf. [7]).

4.2 Rewriting the model (B1) using the virtual thickness

As we did in Section 3.1.2 and in order to compare our model with the Meng-Wang model [35], we rewrite the above system (B1) in terms of the virtual thickness H and Δ_H introduced in (3.7) and (3.8) respectively. For easy tracking in this section, we point out once again that

$$h_m = H - \Delta_H, \quad h_m + h_f = H + (h_f - \Delta_H), \quad \rho_f h_f = \rho(H - h_m) = \rho \Delta_H.$$

From the mass equations in (4.1), we obtain the total mass conservation equation

$$\partial_t(\rho H) + \nabla \cdot (\rho H V_m) = 0. \quad (4.10)$$

Each of the mass equations can also be written in terms of H as follows (see Appendix E for details)

$$\partial_t(\rho_s \varphi H) + \nabla \cdot (\rho_s \varphi H v) = -\varphi \frac{\rho_f \rho_s}{\rho} (H \Phi + \nabla \cdot (H(1-\varphi)(u-v))), \quad (4.11a)$$

$$\partial_t(\rho_f (1-\varphi) H) + \nabla \cdot (\rho_f (1-\varphi) H u) = \varphi \frac{\rho_f \rho_s}{\rho} (H \Phi + \nabla \cdot (H(1-\varphi)(u-v))), \quad (4.11b)$$

$$\partial_t(\rho \Delta_H) + \nabla \cdot (\rho \Delta_H V_m) = \rho_f \mathcal{V}_f. \quad (4.11c)$$

The momentum equations given in (4.4a), (4.4b) become

$$\begin{aligned}
& \partial_t \left(\rho_s \varphi (Hv + \Delta_H (V_m - v)) \right) + \nabla \cdot \left(\rho_s \varphi (Hv \otimes v + \Delta_H (V_m \otimes V_m - v \otimes v)) \right) \\
&= -g \cos \theta \nabla \left((\rho_s - \rho_f) \varphi \frac{(H - \Delta_H)^2}{2} + \rho_f \frac{(H + (h_f - \Delta_H))^2}{2} \right) \\
&+ \rho_f (1 - \varphi) g \cos \theta H \nabla (H + (h_f - \Delta_H)) - \rho_s \varphi H g \cos \theta \nabla b + (1 - \varphi) (H - \Delta_H) \overline{\nabla p_{f_m}^e} \\
&+ \beta (H - \Delta_H) (u - v) - \mu \operatorname{sgn}(v) \left(\varphi (\rho_s - \rho_f) g \cos \theta (H - \Delta_H) - (p_{f_m}^e)_{|b} \right)_+ \\
&+ \frac{\rho_s \varphi}{\rho} ((1 - \lambda_f) u + \lambda_f V_m) \rho_f \mathcal{V}_f - \rho_s \varphi H g \sin \theta \mathbf{e}_x - \Delta_H \frac{\rho_f \rho_s}{\rho} V_m (\varphi \Phi + (v - V_m) \cdot \nabla \varphi),
\end{aligned} \tag{4.11d}$$

$$\begin{aligned}
& \partial_t \left(\rho_f (1 - \varphi) (Hu + \Delta_H (V_m - u)) \right) + \nabla \cdot \left(\rho_f (1 - \varphi) (Hu \otimes u + \Delta_H (V_m \otimes V_m - u \otimes u)) \right) \\
&= -\rho_f (1 - \varphi) H g \cos \theta \nabla (b + H + (h_f - \Delta_H)) - (1 - \varphi) (H - \Delta_H) \overline{\nabla p_{f_m}^e} \\
&- \beta (H - \Delta_H) (u - v) - \frac{\rho_s \varphi}{\rho} ((1 - \lambda_f) u + \lambda_f V_m) \rho_f \mathcal{V}_f - \frac{5 \eta_e (1 - \varphi)}{2} \frac{u}{H - \Delta_H} \\
&- \rho_f (1 - \varphi) H g \sin \theta \mathbf{e}_x + \Delta_H \frac{\rho_f \rho_s}{\rho} V_m (\varphi \Phi + (v - V_m) \cdot \nabla \varphi),
\end{aligned} \tag{4.11e}$$

with

$$\mathcal{V}_f = -(H - \Delta_H) \Phi - \nabla \cdot ((H - \Delta_H) (1 - \varphi) (u - v)). \tag{4.11f}$$

In these equations we can also use the following equivalence that relates the velocity differences,

$$\rho_f (1 - \varphi) (u - V_m) = \rho_s \varphi (V_m - v) = \frac{\rho_f (1 - \varphi) \rho_s \varphi}{\rho} (u - v).$$

4.3 Oversimplified one-layer model with two velocities (C1)

As we did for the one-velocity model (C2), an oversimplified version (C1) (see figure 3) of the two-layer model (B1) may be obtained by using the virtual thickness H as the only thickness. We thus assume the same condition as in (3.13),

$$\Delta_H = H - h_m \ll H,$$

and obtain the following system for the unknowns H, φ, u, v :

$$\partial_t (\rho_s \varphi H) + \nabla \cdot (\rho_s \varphi H v) = \varphi \frac{\rho_f \rho_s}{\rho} \mathcal{V}_f^*, \tag{4.12a}$$

$$\partial_t (\rho_f (1 - \varphi) H) + \nabla \cdot (\rho_f (1 - \varphi) H u) = -\varphi \frac{\rho_f \rho_s}{\rho} \mathcal{V}_f^*, \tag{4.12b}$$

$$\begin{aligned}
\partial_t (\rho_s \varphi H v) + \nabla \cdot (\rho_s \varphi H v \otimes v) &= -g \cos \theta \nabla \left(\rho_s \varphi \frac{H^2}{2} \right) + g \cos \theta \rho_f \frac{H^2}{2} \nabla \varphi - \rho_s \varphi H g \cos \theta \nabla b \\
&+ (1 - \varphi) H (\overline{\nabla p_{f_m}^e})^* + \beta H (u - v) - \operatorname{sgn}(v) \mu \left(\varphi (\rho_s - \rho_f) g \cos \theta H \right. \\
&\left. - (p_{f_m}^e)_{|b}^* \right)_+ + \frac{\rho_s \varphi}{\rho} ((1 - \lambda_f^*) u + \lambda_f^* V_m) \rho_f \mathcal{V}_f^* - \rho_s \varphi H g \sin \theta \mathbf{e}_x,
\end{aligned} \tag{4.12c}$$

$$\begin{aligned}
\partial_t \left(\rho_f (1 - \varphi) H u \right) + \nabla \cdot \left(\rho_f (1 - \varphi) H u \otimes u \right) = & -\rho_f (1 - \varphi) H g \cos \theta \nabla (b + H) - (1 - \varphi) H (\overline{\nabla p_{f_m}^e})^* \\
& - \beta H (u - v) - \frac{\rho_s \varphi}{\rho} ((1 - \lambda_f^*) u + \lambda_f^* V_m) \rho_f \mathcal{V}_f^* \\
& - \frac{5}{2} \frac{\eta_e (1 - \varphi)}{H} u - \rho_f (1 - \varphi) H g \sin \theta \mathbf{e}_x.
\end{aligned} \tag{4.12d}$$

The rheological and dilatancy laws are modified in exactly the same way as for the one-layer model given by equations (3.15). The pressure term in the above momentum equations reads

$$(\overline{\nabla p_{f_m}^e})^* = \frac{1}{H} \left(\nabla (H (\overline{p_{f_m}^e})^*) + (p_{f_m}^e)_{|b}^* \nabla b \right), \quad \text{with} \quad (\overline{p_{f_m}^e})^* = -\frac{\beta}{(1 - \varphi)^2} \frac{H^2}{3} \Phi^*. \tag{4.13}$$

Note that this term does not appear in the one-layer model. Finally, the approximation the exchange term in (4.11f) becomes

$$\mathcal{V}_f^* = -H \Phi^* - \nabla \cdot (H (1 - \varphi) (u - v)), \tag{4.14}$$

and the distribution coefficient λ_f^* is defined as in (2.22) but with \mathcal{V}_f^*

$$\lambda_f^* = \frac{1}{2} - \frac{1}{2} \operatorname{sgn}(\mathcal{V}_f^*) \delta_f, \quad \delta_f = \begin{cases} 0 & \text{centered distribution,} \\ 1 & \text{upwind distribution.} \end{cases} \tag{4.15}$$

4.4 Comparison with the Meng-Wang model

In this section, we compare our previous one-layer two-velocity model (C1) to the model proposed by Meng and Wang in [35]. The Meng-Wang model comes from a combination of our previous work [7] and of the Iverson and George model [23, 18]. Indeed, they use the rheological and dilatancy laws from [7], as well as different fluid and solid velocities in the mixture, and they used our way of calculating the basal solid pressure. However, they use the virtual thickness concept of Iverson and George [23, 18]. As a result, as in the Iverson-George model only the total mass ρh is conserved in the Meng-Wang model and there is no information on the conservation of the solid and the fluid mass or volume.

4.4.1 The Meng-Wang model

We express here the Meng-Wang model using our notation for the densities ρ, ρ_s, ρ_f , velocities v, u and volume fraction φ , while we keep the notation h for the virtual surface and p_e for the averaged excess pore pressure, as in the Iverson-George model (see equivalence of notations in Appendix B). We use the sub-index MW to denote particular coefficients for the Meng-Wang model. We have also recombined some terms in the equations for an easier comparison.

The Meng-Wang model for unknowns h, φ, v, u is stated as

$$\partial_t (\rho_s \varphi h) + \nabla (\rho_s \varphi h v) = \mathfrak{J}, \tag{4.16a}$$

$$\partial_t (\rho_f (1 - \varphi) h) + \nabla (\rho_f (1 - \varphi) h u) = -\mathfrak{J}, \tag{4.16b}$$

$$\begin{aligned}
\partial_t(\rho_s\varphi hv) + \nabla \cdot (\rho_s\varphi hv \otimes v) &= -\nabla \left(\rho_s\varphi g \cos\theta \frac{h^2}{2} \right) + g \cos\theta \rho_f \frac{h^2}{2} \nabla\varphi \\
&+ (1-\varphi)\nabla(hp_e) \\
&- \text{sgn}(v)\mu_{\text{MW}} \left(\varphi(\rho_s - \rho_f)hg \cos\theta - (p_e)|_b \right) \\
&+ h\beta_{\text{MW}}(u-v) - \rho_s\varphi hg \sin\theta \mathbf{e}_x \\
&+ ((1-\lambda)u + \lambda v)\mathfrak{J} - \alpha_s\varphi v,
\end{aligned} \tag{4.16c}$$

$$\begin{aligned}
\partial_t(\rho_f(1-\varphi)hu) + \nabla \cdot (\rho_f(1-\varphi)hu \otimes u) &= -(1-\varphi)\nabla \left(\rho_f g \cos\theta \frac{h^2}{2} \right) \\
&- (1-\varphi)\nabla(hp_e) \\
&- \alpha_f(1-\varphi)u - h\beta_{\text{MW}}(u-v) \\
&- \rho_f(1-\varphi)hg \sin\theta \mathbf{e}_x \\
&- ((1-\lambda)u + \lambda v)\mathfrak{J} \\
&+ h(1-\varphi)\nabla \cdot (2\eta_f D(u)).
\end{aligned} \tag{4.16d}$$

The granular mass flux \mathfrak{J} through the virtual surface is given by

$$\mathfrak{J} = -\varphi \frac{\rho_f \rho_s}{\rho} \left(h\Phi_{\text{MW}} + \nabla \cdot (h(1-\varphi)(u-v)) \right), \tag{4.16e}$$

and the value for Φ_{MW} considered in [35] coincides with the one defined in equations 5.8 and 5.9 of [7], that is

$$\begin{aligned}
\Phi_{\text{MW}} &= \dot{\gamma}_{\text{MW}} \tan\psi_{\text{MW}}, \quad \tan\psi_{\text{MW}} = K_1(\varphi - \varphi_{\text{MW}}^{\text{eq}}), \quad \varphi_{\text{MW}}^{\text{eq}} = \varphi_c - K_2 \frac{\eta_f \dot{\gamma}_{\text{MW}}}{p_{s|b}}, \\
\dot{\gamma}_{\text{MW}} &= 3 \frac{|v|}{h}, \quad \mu_{\text{MW}} = \tan(\delta + \psi_{\text{MW}}),
\end{aligned} \tag{4.16f}$$

for η_f the dynamic viscosity of the fluid. The friction coefficient between phases is

$$\beta_{\text{MW}} = (1-\varphi)^2 \frac{\eta_f}{k_{\text{MW}}} \tag{4.16g}$$

where the hydraulic permeability k_{MW} is considered as a constant. The terms related to the pressure are

$$p_e = \frac{2}{3}(p_e)|_b, \quad (p_e)|_b = -\frac{1}{2} \frac{\beta_{\text{MW}}}{(1-\varphi)^2} h^2 \left(\Phi_{\text{MW}} + \nabla \cdot ((1-\varphi)(u-v)) \right). \tag{4.16h}$$

The viscous term, the last in equation (4.16d), involves the strain rate $D(u) = (\nabla u + \nabla^t u)/2$, for u the averaged fluid velocity. The coefficient λ in the momentum equations arbitrarily determines the distribution of the granular mass flux between the phases at the virtual interface. It is given in [35] by

$$\lambda = 1 - \varphi. \tag{4.16i}$$

The friction coefficients α_s and α_f are for the solid and fluid at the bottom, respectively. Strangely, two friction forces are considered for the solid at the bottom: the Coulomb friction and a Navier drag with coefficient α_s .

4.4.2 Obtaining our model (C1)

The Meng-Wang model (4.16) becomes our one-layer two-velocity model (C1) (*i.e.* (4.12)) with $b = 0$ under the following assumptions:

- * $h = H$,
- * $\nabla \cdot (2\eta_f D(u))$ is negligible,
- * $\alpha_f = \frac{5}{2} \frac{\eta_e}{h_m}$,
- * $\alpha_s = 0$ (no additional Navier friction at the bottom for the solid phase).

Let us discuss the second and third assumptions related to the viscous and bottom friction stresses in the fluid. In the Meng-Wang model the authors only kept the downslope gradient of the viscous stress tensor $\nabla \cdot (2\eta_f D(u))$ and removed the slope perpendicular gradient that leads, when depth-averaged, to the viscous stress at the bottom $\frac{5}{2} \frac{\eta_e u}{h_m}$. This last term is however dominant in the asymptotics related to the shallow flow approximation. Furthermore, if the term $\nabla \cdot (2\eta_f D(u))$ is kept, other small terms of the same order should have been kept in the slope-perpendicular momentum equations. Instead of keeping the viscous stress at the bottom, they used the Navier friction law from [7]. Replacing the constant value of α_f by the expression above results in replacing the Navier friction law by the basal viscous term (see Appendix A.2). There are other differences coming from the considered closure relations. Details of calculations are given in Appendix D.1. The rheology in the Meng-Wang model is taken from [43] and [7], while we used updated rheology in the present work. The friction coefficient β between the solid and fluid phases in the mixture is also different since the hydraulic permeability k_{MW} is a constant while our permeability depends on the grain diameter and on the solid volume fraction (see (2.17)). This is a key difference as will be shown in the numerical tests. Another difference comes from the approximation of the basal pore pressure (compare (4.16h) for the Meng-Wang model and (3.15) in the present work). Indeed, they took the higher order approximation given in [7] corresponding to values of $\beta \sim O(1)$ while we only kept here the term corresponding to $\beta \sim O(\epsilon^{-1})$. Since β values are very high, we do not require an approximation of the basal pore pressure higher than $\beta \sim O(\epsilon^{-1})$.

Regarding the additional Navier solid friction, the authors in [36] assert that in the absence of such an additional friction term, the granular mass would be continuously accelerated. However, in the numerical comparison performed here (see Section 5.3.1), this additional friction term has no significant effect. This lack of impact stems from the fact that Coulomb friction is proportional to the pressure, making it four orders of magnitude larger than this linear term.

To identify other differences between the Meng-Wang model and model (C1), note that

$$\mathfrak{J} = \varphi \frac{\rho_f \rho_s}{\rho} \mathcal{V}_f^*, \quad \text{and} \quad \lambda = \frac{\varphi \rho_s}{\rho} \lambda_f^*.$$

Note also that if we assume $u = v$ in the Meng-Wang model we do not obtain the Iverson-George model since the closures for pressure, dilatancy and rheology are instead inspired by our previous work [7]. Instead, we obtain a model similar to our oversimplified model (C2) with the equivalence $h = H$ (equations (3.14)).

5 Numerical illustrations in uniform regime

In this section, we perform a series of simulations of granular flows on sloping beds in uniform regimes in order to compare the series of models derived here between one another and with the

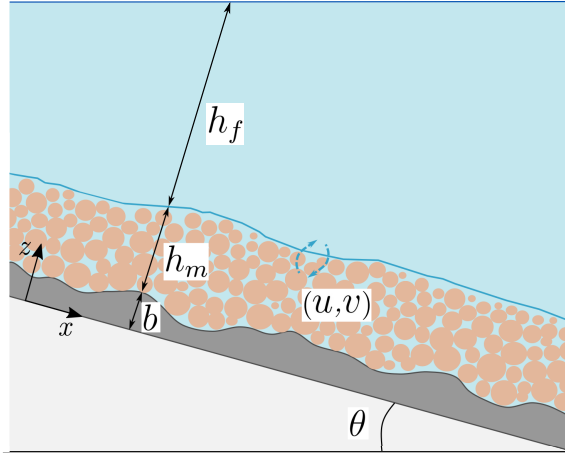


Figure 8: Flow configuration for the full **two-layer model with three velocities (A1)** from [7] in the immersed configuration **where the upper layer velocity u_f is set to zero and the water free surface is fixed as horizontal $h_f + h_m + b + x \tan \theta = cst$.**

Iverson-George and Meng and Wang models. We first consider, in section 5.1, immersed granular flows (figure 8) that mimic submarine avalanches in order to compare with the lab-experiments presented in [43]. Then, in the next sections 5.2-5.3, we focus on grain-fluid flows with a small layer of fluid on top of them, which are a proxy for natural debris flows. For the sake of clarity, the equations describing these uniform configurations for the different models (figure 3) are given in Appendix G.

5.1 Immersed flows - effect of rheology

In this test, we compare the present rheology (2.7) to the one used in [7] and discuss the sensitivity of the results to the rheological parameters by comparing with lab-experiments [43]. These experiments correspond to the immersed configuration represented in figure 8, described by the following equations

$$\partial_t h_m = h_m \Phi, \quad (5.1a)$$

$$\partial_t \varphi = -\varphi \Phi, \quad (5.1b)$$

$$\partial_t v = -\mu \operatorname{sgn}(v) \frac{p_s|b}{\rho_s \varphi h_m} + \frac{\beta}{\rho_s \varphi} (u - v) - g(1 - \rho_f/\rho_s) \sin \theta \mathbf{e}_x, \quad (5.1c)$$

$$\partial_t u = -\frac{1}{2} \Phi \frac{u}{1 - \varphi} - \frac{\beta}{\rho_f(1 - \varphi)} (u - v) - \frac{k_b}{\rho_f(1 - \varphi) h_m} u, \quad (5.1d)$$

with $k_b = (5/2)\eta_e(1 - \varphi)/h_m$, which is a very small term in all the simulations. To be consistent with [7], we neglect the friction between the mixture and the upper-fluid layer by setting $k_f = 0$ in (2.15) and we considered the centered distribution in (2.22), $\lambda_f = \frac{1}{2}$.

5.1.1 Physical and rheological parameters

Following [43] and [7], four cases are analyzed, corresponding to loose and dense initial packing volume fraction, both for high and low fluid viscosity. For all of them we use

$$\rho_s = 2500 \text{ kg/m}^3, \quad \rho_f = 1041 \text{ kg/m}^3, \quad d = 1.6 \times 10^{-4} \text{ m}.$$

The high viscosity case corresponds to $\eta_f = 0.96 \times 10^{-1}$ Pa s, a slope angle $\theta = 25^\circ$ and

$$h_m^0 = 4.9 \times 10^{-3} \text{ m}, \quad \varphi^0 = \begin{cases} 0.562 & \text{loose,} \\ 0.588 & \text{dense,} \end{cases} \quad u^0 = v^0 = 0 \text{ m/s.}$$

The low viscosity case corresponds to $\eta_f = 0.98 \times 10^{-2}$ Pa s, a slope angle $\theta = 28^\circ$ with

$$h_m^0 = 6.1 \times 10^{-3} \text{ m}, \quad \varphi^0 = \begin{cases} 0.576 & \text{loose,} \\ 0.592 & \text{dense,} \end{cases} \quad u^0 = v^0 = 0 \text{ m/s.}$$

where u^0 and v^0 are the initial fluid and solid velocities within the mixture. Finally, the parameters defining the rheological laws, see equations (2.7), are: α_φ , α_μ , φ_c , μ_c , I_0 , b_φ and $\Delta\mu$. For the first two parameters involved in the definition of \mathcal{J}_φ and \mathcal{J}_μ , respectively, we use the values of [55]

$$\alpha_\varphi = 0.1, \quad \alpha_\mu = 0.0088$$

since such parameters did not appear in the rheology chosen in [43] where the lab-experiments were presented. As in [43], we set

$$\varphi_c = 0.582, \quad \mu_c = 0.415, \quad \text{and} \quad I_0 = 0.279.$$

Finally, we must specify the values of b_φ and $\Delta\mu$. To be as close as possible to the rheology of [55] (table 2), that is

$$\varphi_{\text{Tapia}}^{\text{eq}} = \varphi_c(1 - a_\varphi \mathcal{J}_\varphi^{1/2}), \quad \mu_{\text{Tapia}}^{\text{eq}} = \mu_c(1 + a_\mu \mathcal{J}_\mu^{1/2}), \quad (5.2)$$

we linearize our expressions (2.7) as follows

$$\varphi_{\text{lin}}^{\text{eq}} = \varphi_c - \varphi_c b_\varphi \mathcal{J}_\varphi^{1/2}, \quad \mu_{\text{lin}}^{\text{eq}} = \mu_c + \frac{\Delta\mu}{I_0} \mathcal{J}_\mu^{1/2}. \quad (5.3)$$

By comparing (5.2) and (5.3) we obtain the following equivalence of parameters

$$b_\varphi \equiv a_\varphi, \quad \Delta\mu \equiv \mu_c I_0 a_\mu.$$

In [55], the values $a_\varphi = 0.66$, $a_\mu = 11.29$ are proposed to fit their laboratory experiments, thus leading to

$$b_\varphi = a_\varphi = 0.66, \quad \Delta\mu = \mu_c I_0 a_\mu, \quad \text{with} \quad a_\mu = 11.29.$$

Finally, we perform a sensitivity analysis around these values to identify the set of parameters making it possible to obtain the steady states with our present rheology that are as close as possible to the one used in [7] (see Appendix H.1). Based on this analysis, we set

$$\Delta\mu = 0.653, \quad b_\varphi = 0.99,$$

corresponding to $a_\mu = 5.645$.

5.1.2 Flow behavior in loose and dense cases

In figure 9, we show the solid velocity v , the excess pore fluid pressure $(p_{fm}^e)_b$, solid volume fraction φ , friction coefficient μ and tangent of the dilatancy angle $\tan(\psi)$ for the loose and dense cases for both high and low viscosity. Let us first present the flow behavior obtained with the rheology proposed here that involves the dimensionless inertial and viscous numbers I^2 and

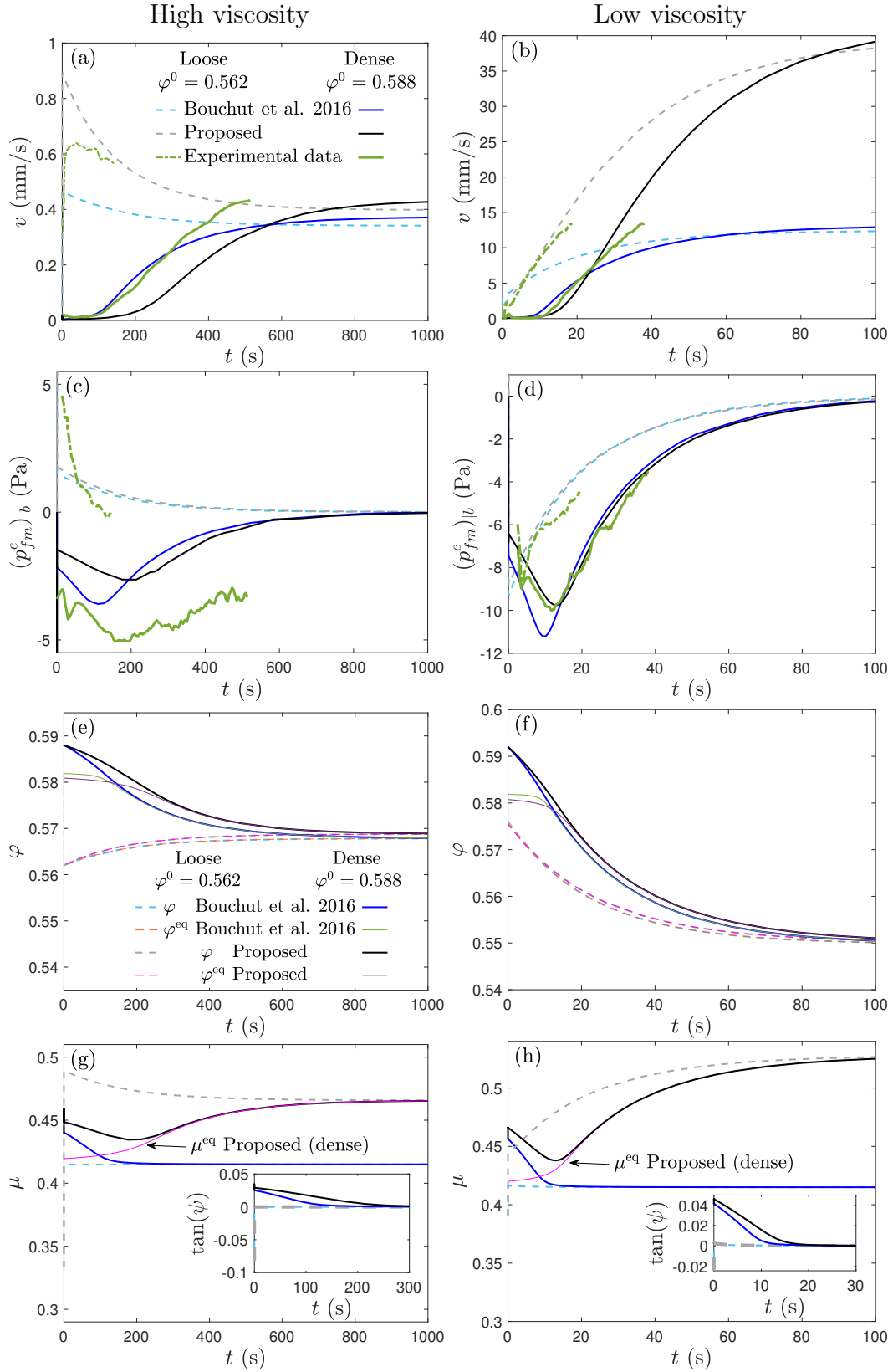


Figure 9: Solid velocity v , basal excess pore pressure $(p_{fm}^e)_b$, solid volume fraction φ , friction coefficient μ , and tangent of the dilatation angle ψ in the high viscosity (left column) and low viscosity (right column) case, for both the dense (full lines) and the loose (dashed lines) cases. The results for the proposed rheology are in black/gray and for the rheology in [7] in blue. The lab-experiments from [42] are in green.

J. Note that in the simulated cases I^2 is negligible for high viscosity and is only about 10% of J for low viscosity (see figure 28 of Appendix H.1).

In the dense case, for both viscosities, the granular mass takes some time to start moving and then accelerates until it reaches the steady critical state (figure 9a,b). Since the beginning, the granular mass dilates (φ decreases and $\tan \psi > 0$) until it reaches the critical state (figure 9e,g). The excess pore pressure becomes negative during this transient regime (figure 9c,d) thus increasing the basal solid pressure (figure 29a,b). The positive dilatancy angle contributes to increase the effective friction coefficient μ at the beginning of the flow (figure 9g,h). These two effects contribute to increase the basal frictional shear stress, explaining why the mass takes time to start at the initial instants. Interestingly, since $\tan(\psi)$ decreases with time, dilatancy generates a friction weakening effect at the beginning of the flow that would not arise otherwise. Indeed, once $\tan(\psi)$ becomes very small after about 300 s for high viscosity and 20 s for low velocity, the friction coefficient increases, approaching to μ^{eq} , the evolution of which is dictated by the viscous-inertial number (figure 9g,h). Interestingly, the overall evolution of μ and $(p_{fm}^e)_b$ look very similar. This is partly related to the fact that $\dot{\gamma}$ is very small at the beginning (figure 29c,d) and thus the evolution of the two quantities follow the evolution of $\tan \psi$, while later on, $\dot{\gamma}$ increases and $\tan \psi$ becomes small so that $\dot{\gamma}$ controls their evolution as shown by the expression of μ and $(p_{fm}^e)_b$ in (2.4.3).

In the loose case, the mass starts to move at the beginning for the two viscosities. Let us first look at the behavior at high viscosity (dashed gray lines in the left column of figure 9). In that case, the mass acceleration is huge at the very beginning and then the velocity decreases until it reaches the steady critical state. Since the beginning, the granular mass compresses (φ increases and $\tan \psi < 0$) until it reaches the critical state. The excess pore pressure becomes positive during this transient regime thus significantly reducing the basal solid pressure p_{sb} (figure 29a,b) and therefore the basal frictional shear stress. This explain the higher velocity in the loose case compared to the dense case, despite the higher friction coefficient. Contrary to the dense case, φ approaches φ^{eq} at the very beginning since the negative dilatancy angle is very small, with a negligible contribution to the decrease of the effective friction coefficient μ (figure 9g). As a result μ is always very close to μ^{eq} . The friction coefficient is high at the beginning because of the high viscous-inertial number related to the high shear strain rate $\dot{\gamma}$ (figure 29c,d).

At first glance, it seems surprising that the behavior in the loose case is so different at low viscosity where the variables behave as in the dense case: increase of solid velocity, decrease of solid volume fraction and negative excess pore fluid pressure. In fact, the initial compaction in the so-called loose case in [43] is higher than the critical state solid volume fraction at equilibrium and thus could have been considered as dense. We still however keep calling this case loose in the following for consistency with [43] and [7]. Note that the granular compaction represented by $\text{div } v$ is one order of magnitude higher for low viscosity ($\sim 10^{-3}$) than for high viscosity ($\sim 10^{-4}$) (figure 29e,f).

5.1.3 Influence of the rheology

Figure 9 also makes it possible to compare the variables calculated with the rheology proposed here, the rheology used in [7] and the experimental data [43]. At low viscosity, the present rheology better fits the experiments for the solid velocity and the basal excess pore pressure, in both the so-called loose and dense cases (figure 9b,d). At high viscosity, the solid velocity with the present rheology is also closer to observations in the loose case (figure 9a). The maximum velocity with the proposed rheology is two times higher than with the rheology of [7]. In the dense case, the excess pore pressure is closer to the measurements with the rheology in [7] at the beginning, but its overall shape is better captured by the present rheology (figure 9c). The

greatest difference between the values of $(p_{f_m}^e)_b$ and φ calculated with the two rheologies is observed in the dense case, while they are very close in the loose case. Concerning the friction coefficient, the critical state friction coefficient μ^{eq} is constant in [7], *i.e.* it does not depend on the viscous-inertial number (this dependency was replaced by a viscous term that depends on $\dot{\gamma}$). In the dense case, the time t_{start} at which the granular layer starts to move is better reproduced by the rheology used in [7] but, afterwards, its evolution seems to be better captured with the present rheology.

In figure 10, we investigate the influence of the rheological parameters $\Delta\mu$ and b_φ on the flow variables for the two viscosities. For all cases, we observe that $\Delta\mu$ controls the long-term steady-state velocity even though the long-term values of φ are also controlled by b_φ . In the dense and loose cases, the initial value of the velocity is also significantly affected by b_φ . This would be expected since the compression/dilatation mainly occur during the first stage of the flow until about 300 s for high viscosity and 20 s for low viscosity. However, this tendency is not observed for the other variables. For example, in the dense case, it is rather $\Delta\mu$ that controls the first stage of variation of the excess pore fluid pressure and the absolute value of its maximum, the solid volume fraction φ and the friction coefficient μ . This is also the case of μ^{eq} , h_m , and $\text{div } v$ but not of $\tan \psi$ and $\dot{\gamma}$, not represented here. In the loose case, the variables are significantly different for the different values of $\Delta\mu$ and b_φ , right from the start.

After this first transient regime (> 300 s for high viscosity and > 20 s for low viscosity), the long-term values of the quantities are different for the different values of $\Delta\mu$ and b_φ for both the loose and dense cases. As observed above, the behavior of the friction coefficient μ is very similar to that of the excess pore fluid pressure as these quantities are related (see section (2.4.3)). In the dense case, the time needed for the mass to start moving t_{start} increases with increasing $\Delta\mu$ as the friction increases. For the same $\Delta\mu$, t_{start} increases with increasing b_φ .

As a result, the dependency of the variables on the rheological parameters is significant and very complex, showing the high sensitivity of the model to the rheological parameters, which are often difficult to constrain on the field scale.

5.2 Debris flow configuration - basal pressure

For the following tests, we consider grain-fluid flows with a free surface in the configuration shown in figure 1, mimicking the experiment developed in [25] and simulated in [18]. In this set-up, we compare the results from the series of models presented above, schematically represented in figure 3. For two layer models, we define the thickness of the initial fluid-only layer at the top as a fraction C_h of the mixture thickness $h_f^0 = C_h h_m^0$.

5.2.1 Physical and rheological parameters

We set the following initial data

$$h_m^0 = \begin{cases} 0.7169 \text{ m} & \text{loose,} \\ 0.65 \text{ m} & \text{dense,} \end{cases} \quad \varphi^0 = \begin{cases} 0.48 & \text{loose,} \\ 0.59 & \text{dense,} \end{cases} \quad h_f^0 = C_h h_m^0 \text{ m}, \quad u^0 = v^0 = u_f^0 = 0 \text{ m/s,}$$

with the slope angle of the bottom at $\theta = 13^\circ$ for the so-called loose and $\theta = 20^\circ$ for the dense cases. We consider the same mass for the mixture in the loose and dense cases so that $(\rho^0 h_m^0)_{\text{loose}} = (\rho^0 h_m^0)_{\text{dense}}$. For one-layer models, the virtual thickness is $H^0 = h_m^0 + \rho_f h_f^0 / \rho^0$, where $\rho^0 = \varphi^0 \rho_s + (1 - \varphi^0) \rho_f$ (see equation (2.1)). When the relaxation equation is used to solve the basal pressure, we assume that the excess pore pressure is zero at the beginning. As a result, the initial basal solid pressure is the hydrostatic pressure $p_{sb}^0 = \varphi^0 (\rho_s - \rho_f) g \cos \theta h_m^0$ for

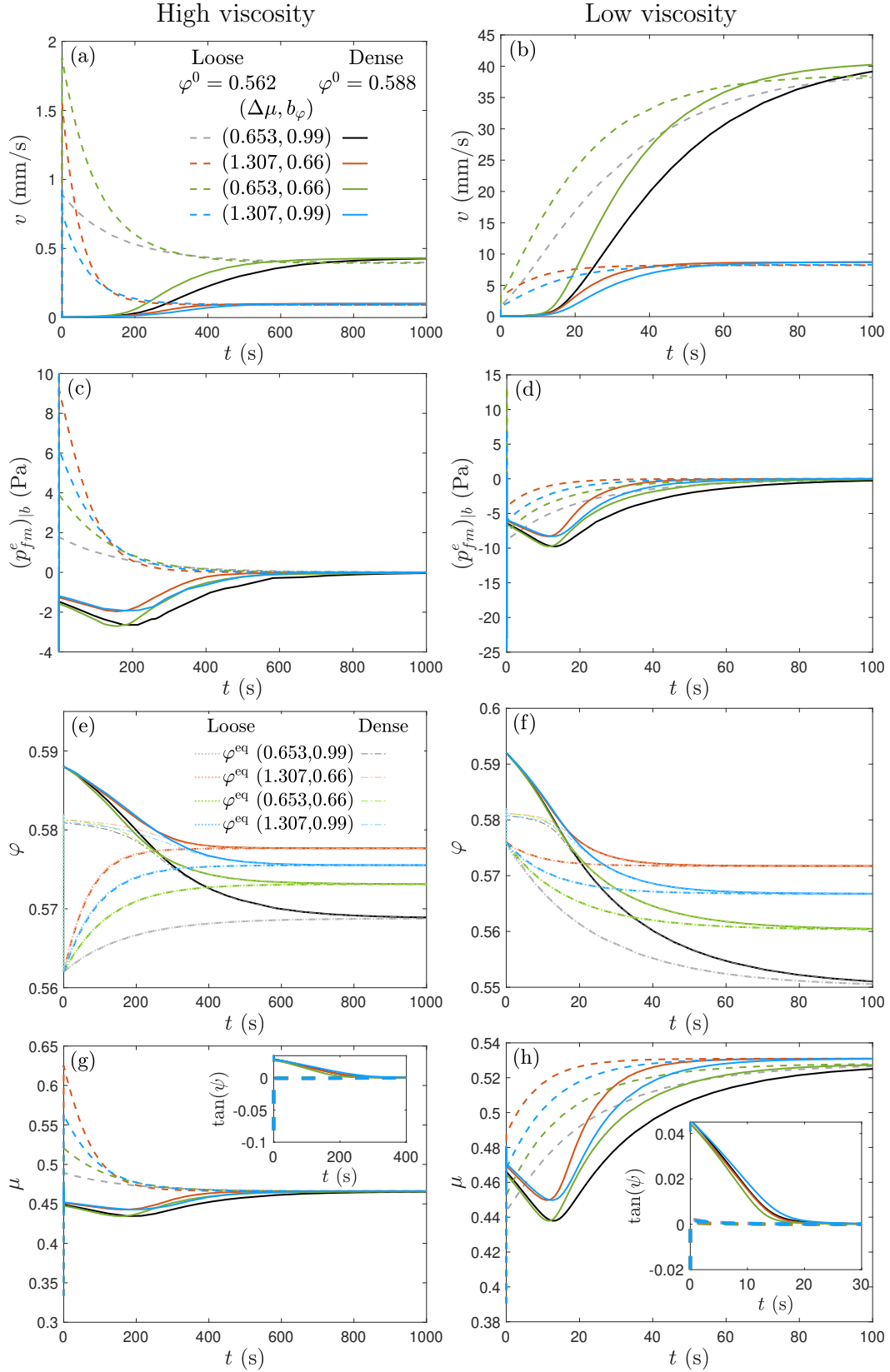


Figure 10: Test 1: Solid velocity v , basal excess pore pressure $(p_{f_m|b}^e)$, solid volume fraction φ , friction coefficient μ and tangent of the dilatancy angle ψ , for high viscosity (left column) and low viscosity (right column) and different values of $\Delta\mu$ and b_φ .

two-layer models and $p_{sb}^0 = \varphi^0(\rho_s - \rho_f)g \cos \theta H^0$ for one-layer models and for the Iverson-George model.

The material properties are

$$\rho_f = 1000 \text{ kg/m}^3, \quad \rho_s = 2700 \text{ kg/m}^3, \quad d = 10^{-3} \text{ m}, \quad \eta_f = 10^{-3} \text{ Pa s},$$

and the rheological parameters

$$\begin{aligned} \alpha_\varphi &= 0.1, & \alpha_\mu &= 0.0088, & b_\varphi &= 0.99, & I_0 &= 0.279, \\ \mu_c &= \tan 29^\circ, & \varphi_c &= 0.56, & a_\mu &= 5.645, & \Delta\mu &= \mu_c a_\mu I_0. \end{aligned} \quad (5.4)$$

Finally, we set $m_f = 1$ for the friction between the mixture and upper-fluid layer (equation (2.15)).

5.2.2 Computation of the solid pressure at the bottom

We compare here the two ways of calculating the basal solid pressure in the proposed models described in Section 2.3.2: either as the solution of the third-degree polynomial (2.24) or as the solution of the evolution equation (2.26) involving grain elasticity. For very large elastic solid bulk modulus, these equations are equivalent since (2.26) can be seen as a relaxation equation for the equation $\Phi = \dot{\gamma} \tan \psi$.

For this, we solve the full model (A1) with two layers and 3 velocities in the loose configuration with $C_h = 0.15$. For this value of C_h , the initial virtual thickness is $H^0 = 0.7762$ m, close to the mixture thickness $h_m^0 = 0.7169$ m. We test several values of B , varying from 10^6 Pa to 10^9 Pa as a typical value for glass beads ([4]). In figure 11(left), we represent the normalized difference between the solution without elasticity and the solution accounting for grain elasticity $|p_{sb}^{\text{pol}} - p_{sb}^{\text{eq}}|$. The difference between the two calculations is non-negligible for $B = 10^6$ Pa (50%), lower for $B = 10^7$ Pa (10%) and drops below 0.1% for $B = 10^9$ Pa. We also tested the value $B = 10^5$ Pa and the difference is greater than 50%. Note that these values occur at the beginning of the simulation ($t = 0.1$ s). After that, they are much smaller, less than 1% for the $B = 10^6$ Pa case. Figure 11(right) shows that for $B > 10^6$ Pa, the effect of elasticity on the basal excess pore pressure is very small and the difference in the solution of the pressure is not noticeable. As pointed out in remark 2 in appendix A.6, equation (2.26) is only valid for a small contribution of elastic effects. Otherwise, plastic expansion and contraction rates must be considered in the model. Thus, for the configuration here, the use of (2.26) to solve the solid pressure remains valid only for $B \leq 10^6$. Note that this value holds for several granular mixtures such as glass beads or sand-gravel. The elasto-plastic effects in debris flows models need further investigation that is outside the scope of this study. Nevertheless, the proposed evolution equation (2.26) provides an interesting alternative to compute the basal pressure, mainly from the numerical point of view as a relaxation equation for the dilatancy law, and is thus more suitable for more complex models, such as multilayer models, as discussed in section 2.3.2.

As discussed above, the same type of equation was proposed in the Iverson-George model to calculate the basal fluid pressure (see equation (3.16d)). In their equation $B = 1/\alpha$, where α is the elastic compressibility, that varies between $10^{-7} - 10^{-2} \text{ Pa}^{-1}$. Indeed, as described in detail in [23], nearly liquefied debris-flow slurries with $\varphi \geq 0.4$ generally exhibits behavior consistent with $\alpha \sim 10^{-5} \text{ Pa}^{-1}$. Compressibilities as large as $\alpha \sim 10^{-2} \text{ Pa}^{-1}$ are found for relatively dilute, mud-rich slurries and dredged sludges with $p_{sb} < 10^3$ Pa and $\varphi < 0.4$, whereas values of $\alpha \sim 10^{-7} \text{ Pa}^{-1}$ are more appropriate for loosely packed sand and sand-gravel mixtures. Iverson and George [23] proposed the empirical relation (see their equation 3.14)

$$\alpha = \frac{a}{\varphi(p_{sb} - \sigma_0)} \quad (5.5)$$

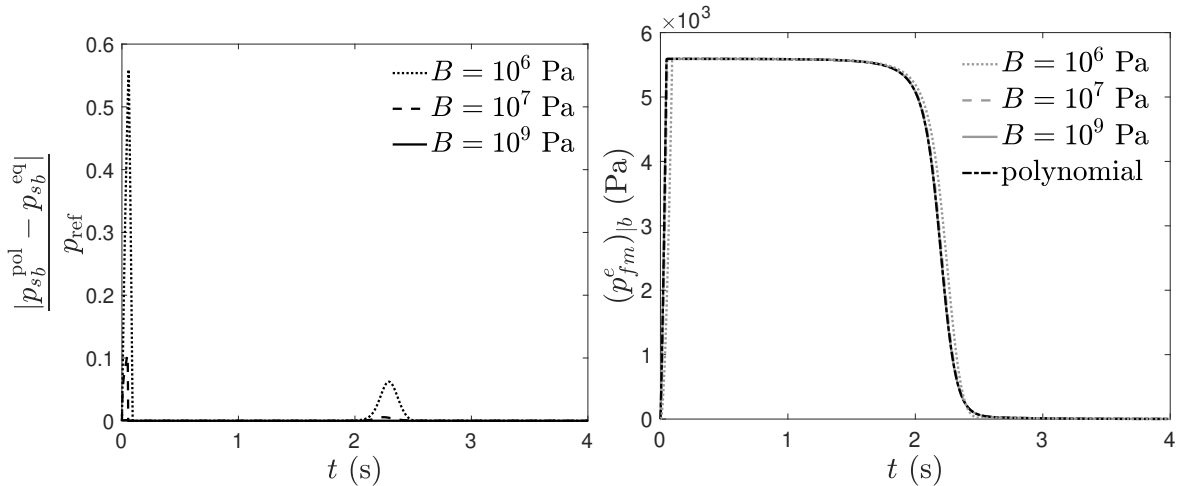


Figure 11: Values obtained for model(A1) ($[2\mathbf{L}: (\mathbf{u}, \mathbf{v}) | \mathbf{u}_f]$) for several values of the coefficient B . Left: Normalized absolute error obtained with the two options of computing basal solid pressure: p_{sb}^{pol} denotes the solution obtained when using the polynomial and p_{sb}^{eq} when using the relaxation equation. The reference pressure p_{ref} is the maximum of the solution p_{sb}^{pol} . Right: corresponding basal excess pore pressure $(p_{fm}^e)_b$ obtained using equation (2.26).

where a is a proportionality calibration coefficient ($a \sim 0.01 - 0.05$) and σ_0 a reference stress ($\sigma_0 \sim 10 - 1000$ Pa). In the uniform configuration solved in this paper, for $\sigma_0 = 1000$ Pa (typical for debris used in flume experiments), these values of a give $B \sim 10^5$. As shown above, this value is not small enough to neglect the elasticity in the model. We would have to decrease a to 10^{-3} to obtain $B \sim 10^7$.

5.3 Comparison of all the proposed models for debris flows

We will focus here on the differences between the models of various levels of complexity for both loose and dense cases. The configuration and parameters are the same as those described in Section 5.2.1. To provide deeper insight into the flow behavior, we compute the forces involved in the model, given by the different terms in the equations. These forces are specified in table 6 of Appendix H.2 for models written in conservative form. Note that for the two-phase models, the forces are plotted for the mixture layer by summing up the momentum equations for the solid and fluid phases.

5.3.1 One-layer models compared to Iverson-George and Meng-Wang models

Let us compare, in the uniform regime, our one layer models (C2), presented in section 3.2, and (C1), presented in section 4.3, with the Iverson-George and Meng-Wang models, respectively. All these models are defined in terms of a *virtual thickness*. The equations of these models in the uniform regime are given in Appendix G: equations (G.12) for (C2), (G.16) for Iverson-George, (G.11) for (C1) and (G.18) for Meng-Wang. We choose the loose case with data given in Section 5.2.1 and $C_h = 0.15$. The values of the constants involved in the Meng-Wang model are those given in their paper [35],

$$K_1 = 1.1, \quad K_2 = 3, \quad \alpha_s = 10 \text{ Ns/m}^3, \quad \alpha_f = 35 \text{ Ns/m}^3.$$

For these models the main difference lies in the rheological laws and in the definition of the permeability, which plays a key role in particular in the dilatancy function Φ in our model, Φ_{MW}

in the Meng-Wang model, and D in the Iverson-George model. It has a strong impact on the excess pore pressure and therefore on the basal solid pressure. In our model the permeability k is a function of φ and d the mean grain diameter. In the Iverson-George model k_{IG} , it is a function of φ , and in the Meng-Wang model k_{MW} is assumed to be constant:

$$k = \frac{(1 - \varphi)^3 d^2}{150\varphi^2}, \quad k_{\text{IG}} = k_0 e^{\frac{0.6 - \varphi}{0.04}}, \quad k_{\text{MW}} = 10^{-9} \text{m}^2,$$

with $k_0 \in 10^{-13} - 10^{-10} \text{m}^2$ a reference permeability (figure 12a). Depending on the value of the constants k_0 and k_{MW} , very different solutions are obtained, the models being highly sensitive to the permeability, as also discussed in [23]. To illustrate this sensitivity, we test two values of k_0 ($k_0 = 2.6 \times 10^{-11}$ considered in [18] and $k_0 = 5 \times 10^{-10}$) and two values of k_{MW} ($k_{\text{MW}} = 10^{-9}$ and $3 \times 10^{-9} \text{m}^2$). Figure 12 shows that the permeability obtained with the original values proposed for the Iverson-George model and the Meng-Wang model are quite far from the permeability k , especially k_{IG} that is one order of magnitude smaller. This induces strong differences between the calculated mixture velocity V_m and basal solid pressure. Our models (C1) and (C2) give almost the same results (the blue and the green lines are superimposed) because the solid and fluid velocities in the mixture become very close from the very beginning (figure 12b). With the proposed models (C1) and (C2) the maximum velocity is around 5 m/s while it reaches 80 m/s in the Iverson-George model and 15 m/s in the Meng-Wang model. The mass stops much later given that the maximum velocity increases. The velocity increases in the same way in all models but its decrease is controlled by the basal frictional shear stress and thus the basal solid pressure and the friction coefficient. Indeed, the velocity increases when $p_{s|b}$ is almost zero, because of the high excess pore pressure, and decreases when $p_{s|b}$ returns to hydrostatic pressure. For example, $p_{s|b}$ stays very low for a very long time in the Iverson-George model leading to this huge velocity (figure 12c).

The variation of the friction coefficient can only be observed at the very first instants (< 3 s), as shown in figure 12d. The alternative values $k_0 = 5 \times 10^{-10}$ and $k_{\text{MW}} = 3 \times 10^{-9} \text{m}^2$, plotted in dash lines, give a permeability closer to k , leading to very similar velocities and basal solid pressure (figures 12b,c) for all models. Interestingly, with these values, the Iverson-George model leads to a higher basal solid pressure than in our model but to a lower friction coefficient so that the velocities of the two models are the same. Even if the velocities are similar, the friction coefficient μ and the dilatancy $\tan \psi$ are not so close, because of the differences in the rheology.

5.3.2 Influence of grain diameter and drag force between the layers

We impose here $C_h = 0.15$ and compare the results for two values of the mean grain diameter $d = 10^{-3}$ m (left column of figure 13) and $d = 10^{-2}$ m (right column), for which the permeability is 100 times bigger (see equation (2.17)). Our first objective is to compare the models, denoted (1), that account for different solid and fluid velocities v and u in the mixture, and models, denoted (2), where $u = v$. For this, we plot both the mixture velocity V_m for the six models (first row of figure 13) and all the velocities involved in the models (second row).

We observe that the mixture velocities are 10 times higher for $d = 10^{-3}$ m than for $d = 10^{-2}$ m. For $d = 10^{-3}$ m, the mixture velocities are the same for the two models of each group A, B, C. Indeed, the calculated solid and fluid velocities in models (1) are almost identical. This is not the case for $d = 10^{-2}$ m where the drag coefficient β between the solid and fluid phases in the mixture is 100 times lower. In this case, we indeed observe very different solid and fluid velocities in the two-phase models (A1), (B1) and (C1) (figure 13d). For example, the fluid velocity u is about three times higher than the solid velocity v for models (A1) and (B1). As a

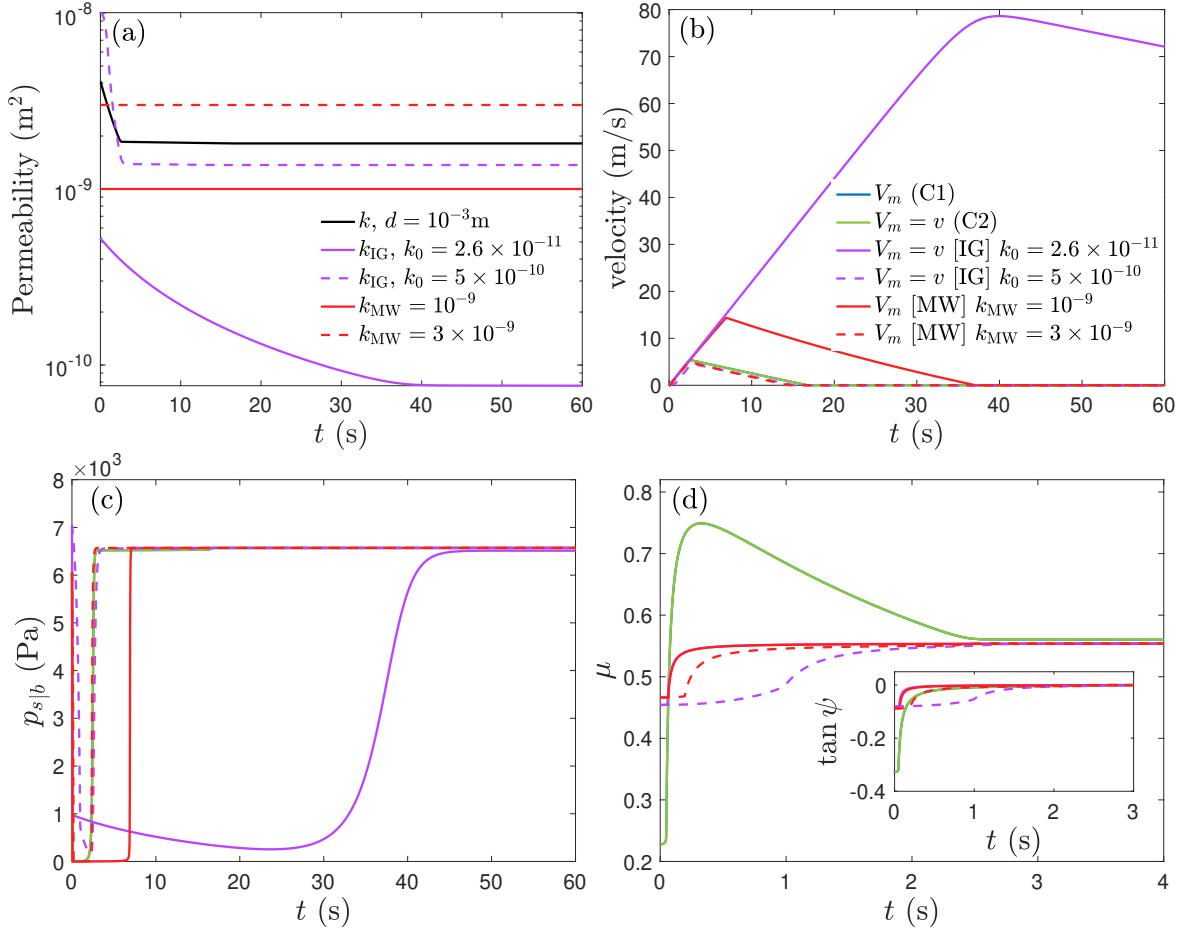


Figure 12: Comparison between our one layer models (C1)=[1L: (\mathbf{u}, \mathbf{v})] and (C2)=[1L: (\mathbf{v})] (lines are superimposed) and with the Iverson-George [IG] and Meng-Wang [MW] models. (a) Permeability for each model with two values of k_0 in the Iverson-George model and of k_{MW} in the Meng-Wang model, (b) velocity, (c) basal solid pressure and (d) friction coefficient.

result, these two-phase models give very different mixture velocities than the one-velocity models (A2), (B2) and (C2) (figure 13b). Furthermore, the behavior of models from groups A, B, and C is much more different than for lower permeability ($d = 10^{-3}$ m). Note that the velocity of the fluid-only upper layer is quite similar for the two-phase model (A1) and for (A2). As a result, for high permeability (here about 10^{-6} m²) we cannot assume $u = v$ in the mixture as done in the models of group (2) and in the Iverson-George model.

The behavior of the two layer models (groups A and B) is similar but with velocity differences which are small for $d = 10^{-3}$ m but can reach 25% for $d = 10^{-2}$ m (13a,b). The one-layer models (group C) have a significantly different behavior even for $d = 10^{-3}$ m since the mixture velocity decreases whereas it stays approximately constant for models of groups A and B. The difference between models (C1) and (C2) is greater than between models (1) and (2) of groups A and B (13b). Furthermore, for $d = 10^{-2}$ m, model (C2) stops, as does the solid phase in model (C1) too, whereas in all other models the mixture velocity only slightly decreases with time (13b,d). As a result, for high permeability, one-layer models with a virtual thickness, such as the Iverson-George model or the Meng-Wang model, may lead to significant errors in the prediction of flow dynamics and deposits.

Figure 13e shows that for $d = 10^{-3}$ m, the excess pore pressure nearly compensates the solid hydrostatic pressure at the beginning, so that $p_s|_b$ approaches zero. While the models from groups A and B give almost identical values of the basal solid pressure and friction coefficient, the models of group C predict a basal solid pressure that is close to zero for a longer time and then increases. This explains why the mixture velocity of models C increases for a longer time and thus decreases more rapidly. Models of groups A and B give also almost identical friction coefficients whereas models of group C give a higher friction coefficient. For $d = 10^{-2}$ m, the excess pore pressure (maximum 200 Pa) is much smaller than for $d = 10^{-3}$ m (maximum 6000 Pa) for all models so that the basal solid pressure only decreases by about 4 to 10 %. Slight differences are observed between models (1) and (2) of the three groups although they are much smaller than for the velocities. Again, models A and B are much closer than model C.

In the models of group A, there is a drag force between the mixture layer and the upper fluid layer. Taking a smaller drag $m_f = 0.1$ instead of $m_f = 1$ in equation (2.15) has almost no impact on the basal pressure or on the friction coefficient. It however significantly changes the velocities in the models as illustrated for $d = 10^{-2}$ m in figure 14c,d. Indeed, as the friction between the layers is smaller, the upper fluid moves faster and the mixture below moves slower. In this case, for $m_f = 0.1$, the granular phase stops after 2 s while it continues to move for $m_f = 1$ since it is entrained by the upper fluid. Similar behavior is observed for $d = 10^{-3}$ m. Interestingly, for $d = 10^{-2}$ m, the averaged velocity V_m in the two-layer models of group A with $m_f = 0.1$ is much closer to the one-layer models (group C) up to about 4 s. Afterwards V_m increases again for two-layer models as opposed to one-layer models (figure 14a,b).

Whatever the drag friction coefficient m_f , the forces are very similar in models (A1) and (A2) (figure 14e,f). At the beginning, the drag force between the layers is greater for $m_f = 1$ than for $m_f = 0.1$ but rapidly these forces reach about the same magnitude since even if $m_f = 0.1$ is smaller, the difference between the upper fluid and the mixture velocities is higher, leading to similar drag forces. As a result, even if the forces acting on the mixture layer are similar, the velocity distribution between the mixture and upper fluid layer is different for different m_f values. Figure 14e,f also clearly shows that the force related to the fluid exchange between the layers is small, but not negligible at the beginning of the flow.

For the dense case represented in figure 15, the differences between the model behaviors are qualitatively the same as in the loose case. However, more differences between models of group A and group B are observed for the basal solid pressure and for the friction coefficient

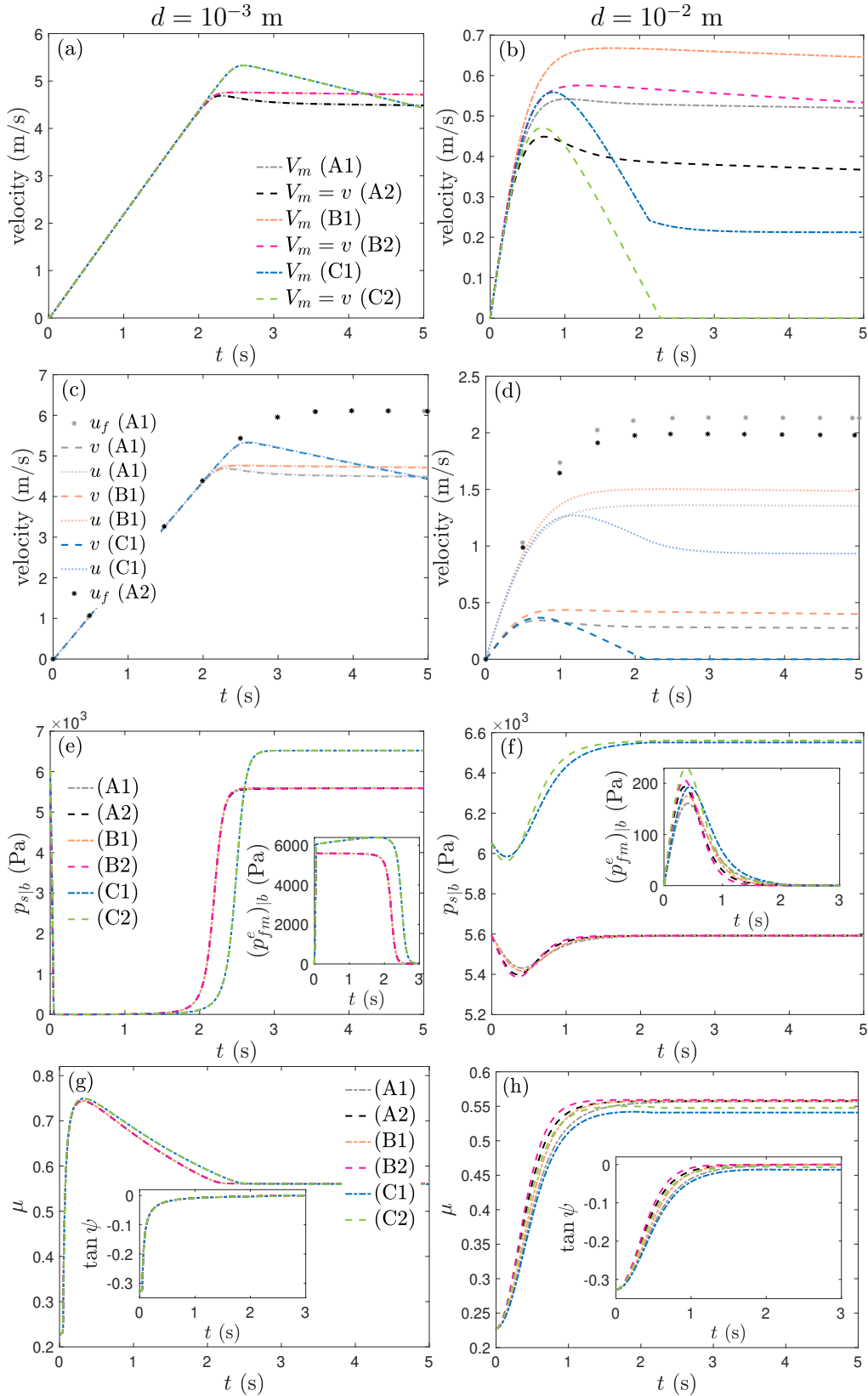


Figure 13: Loose case with slope angle $\theta = 13^\circ$ and for $C_h = 0.15$. Comparison between all the models: those accounting for two velocities u, v in the mixture ((A1), (B1), and (C1)) and those assuming $u = v$ ((A2), (B2), and (C2)), for two grain diameters (*i.e.* two permeabilities): $d = 10^{-3}$ m (left column) and $d = 10^{-2}$ m (right column). (a)-(b) mixture velocity, (c)-(d) all velocities, (e)-(f) basal solid pressure $p_{s|b}$ with basal excess pore pressure $(p_{fm}^e)_{|b}$, (g)-(h) friction coefficient μ with dilatancy $\tan \psi$.

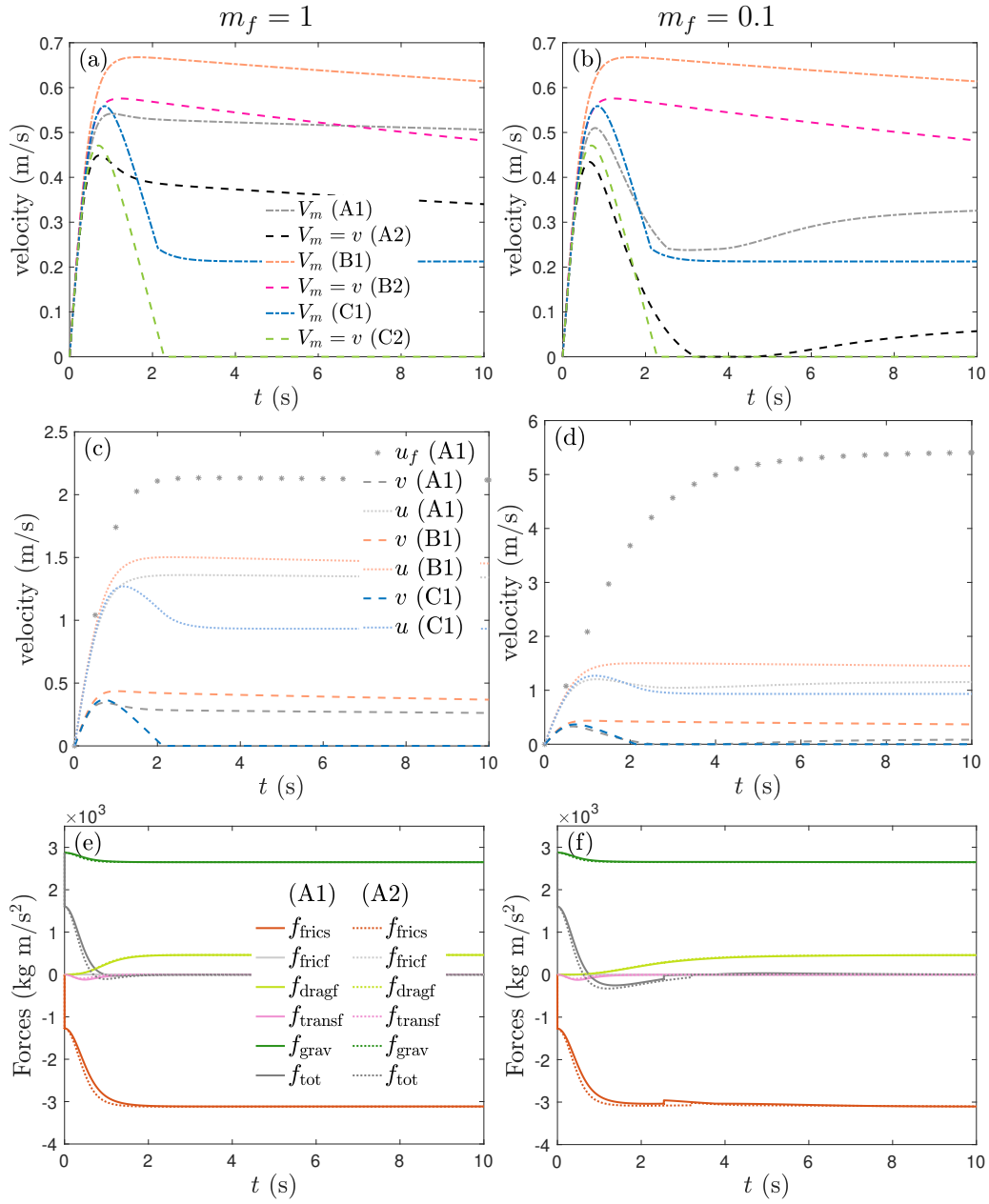


Figure 14: Loose case with slope angle $\theta = 13^\circ$ for $C_h = 0.15$ and $d = 10^{-2}$ m. Comparison between all the models: those accounting for two velocities u, v in the mixture ((A1), (B1), and (C1)) and those assuming $u = v$ ((A2), (B2), and (C2)), for two drag coefficients: $m_f = 1$ (left column) and $m_f = 0.1$ (right column). (a)-(b) mixture velocity, (c)-(d) all velocities, (e)-(f) forces.

for $d = 10^{-3}$. For $d = 10^{-2}$ m, we also observe greater differences between all the models for $p_{s|b}$ and μ (figure 15e-h). Interestingly, for $d = 10^{-3}$ m, the velocity of the upper fluid-only layer increases rapidly whereas the solid phase takes time to start because of the high friction coefficient and basal solid pressure (figure 15e). For higher permeability ($d = 10^{-2}$ m), the solid phase takes less times to start moving (figure 15d). During the time window shown here the velocity increases but, as the friction increases, the velocity subsequently stabilizes at around 300 s for $d = 10^{-2}$ m for two-layer models (groups A and B) but continuously increases and reaches unrealistic high values for one-layer models with a virtual thickness (group C and the Iverson-George and Meng-Wang models).

In the following subsections we set $d = 10^{-3}$ m. As shown above, the models denoted (1), with two velocities u and v in the mixture, and the models denoted (2), where $u = v$, give almost identical results. Therefore, from now on, we only present the results from the simpler models (A2), (B2) and (C2).

5.3.3 Influence of the thickness of the upper fluid layer

We investigate here the influence of the initial thickness of the fluid-only upper-layer $h_f^0 = C_h h_m^0$, by testing two values of C_h , 10^{-3} (very small fluid layer) and 0.5 (thick fluid layer). Indeed, the one-layer models with a virtual thickness (C1), (C2), and Iverson-George and Meng-Wang models are only valid if h_f is small (*i.e.* C_h is small), as demonstrated above.

In figure 16 the results corresponding to the loose case are represented for $C_h = 10^{-3}$ (left column) and $C_h = 0.5$ (right column). Figure 16a,b shows that the virtual thickness H computed by all the models are almost the same. This is the only thickness in the one-layer model (C2). For the two-layer models (A2) and (B2), the total thickness $h_m + h_f$ are the same as well as the mixture thickness h_m . However, the velocities calculated by the different models are significant. Models (A2) and (B2) are quite close whereas the velocity of the one-layer model (C2) decreases more rapidly in the case $C_h = 10^{-3}$. Even worth, in the case $C_h = 0.5$, it decreases while the velocity in the other models increases. The excess pore pressure in (C2) is higher and last longer, especially for $C_h = 0.5$, leading to a longer time where the basal solid pressure is almost zero and, afterwards the basal solid pressure is much higher for model (C2) leading to higher basal frictional stress (see figure 18), leading the mass velocity to decrease much faster than in the two-layer models. The solid volume fraction and friction coefficient are similar for all models with $C_h = 10^{-3}$, while with $C_h = 0.5$, φ is slightly lower and μ slightly larger in (C2) than in (A2) and (B2).

The same qualitative observation are observed in the dense case, with slightly larger differences between the one-layer model (C2) and the two-layer models (A2) and (B2) (figure 17). In particular, the time t_{start} at which the mass starts to move is much larger for model (C2), especially for $C_h = 0.5$ where t_{start} is about four times bigger (8 s instead of 2 s). Indeed, the friction coefficient is much higher which increases the basal frictional stress (see figure 18) even if the solid basal pressure is smaller than in models (A2) and (B2) at the beginning (figure 17e-h). The fact that the basal solid pressure and the friction coefficient stay large for a longer time in model (C2) explain why t_{start} is larger.

The behavior described above is well illustrated when looking at the forces at play (figure 18). We clearly see bigger differences between the forces in the one-layer model (C2) and the two-layer models (A2) and (B2) for $C_h = 0.5$. We also see the mass acceleration f_{tot} that is high at the beginning for the loose case and then decreases and become negative while it is almost zero in the dense case at the beginning and then increases to reach an almost constant value later on. In the dense case, we observe a much bigger basal frictional force with the model (C2) until about 10 s explaining the decrease of velocity described above. Note that the force associated

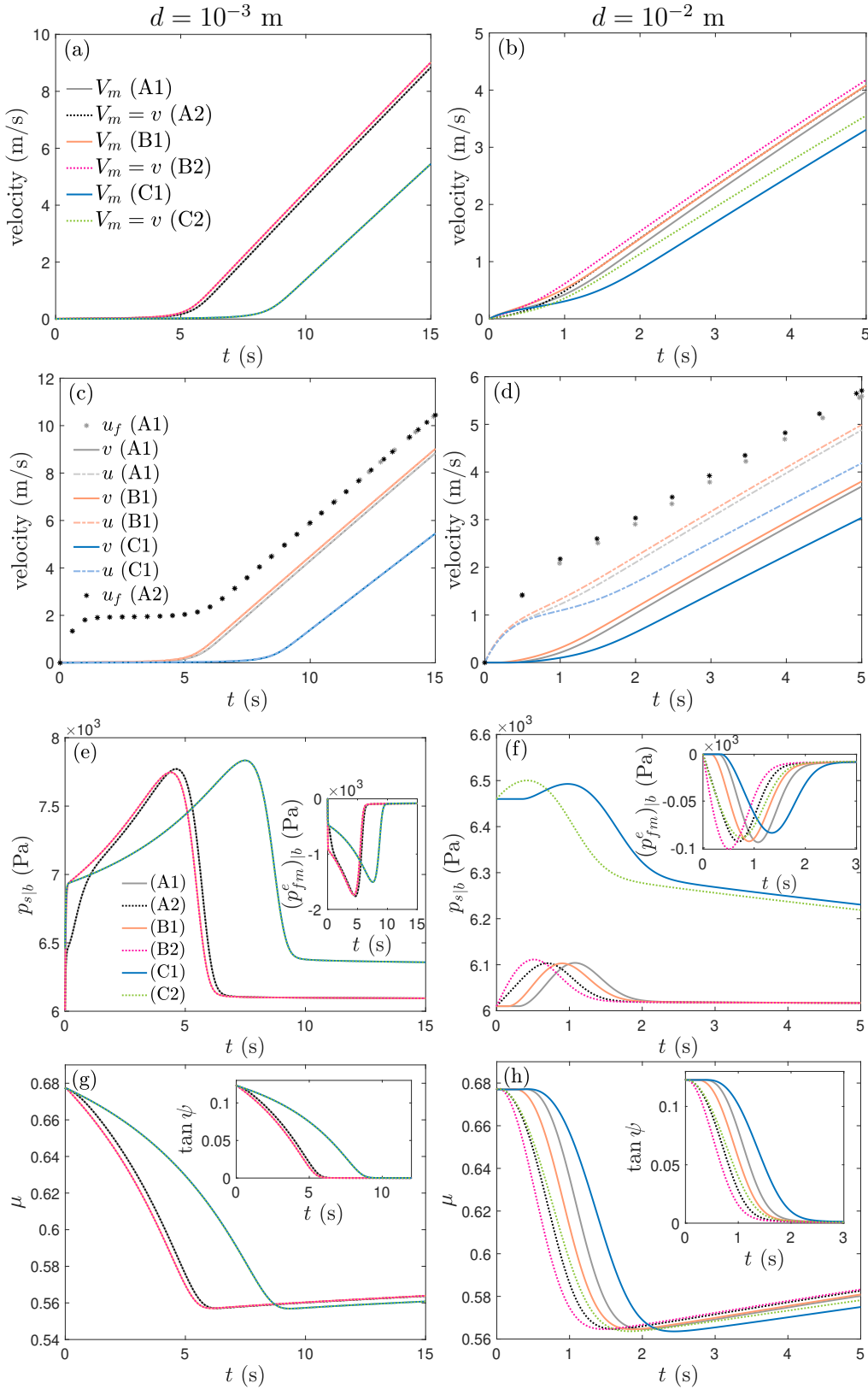


Figure 15: Dense case with slope angle $\theta = 20^\circ$ and for $C_h = 0.15$. Comparison between all the models: those accounting for two velocities u, v in the mixture ((A1), (B1), and (C1)) and those assuming $u = v$ ((A2), (B2), and (C2)), for two grain diameters (*e.g.* two permeabilities) $d = 10^{-3}$ m (left column) and $d = 10^{-2}$ m (right column). (a)-(b) mixture velocity, (c)-(d) all velocities, (e)-(f) basal solid pressure $p_{s|b}$ with basal excess pore pressure $(p_{fm}^e)_{|b}$, (g)-(h) friction coefficient μ with dilatancy $\tan \psi$.

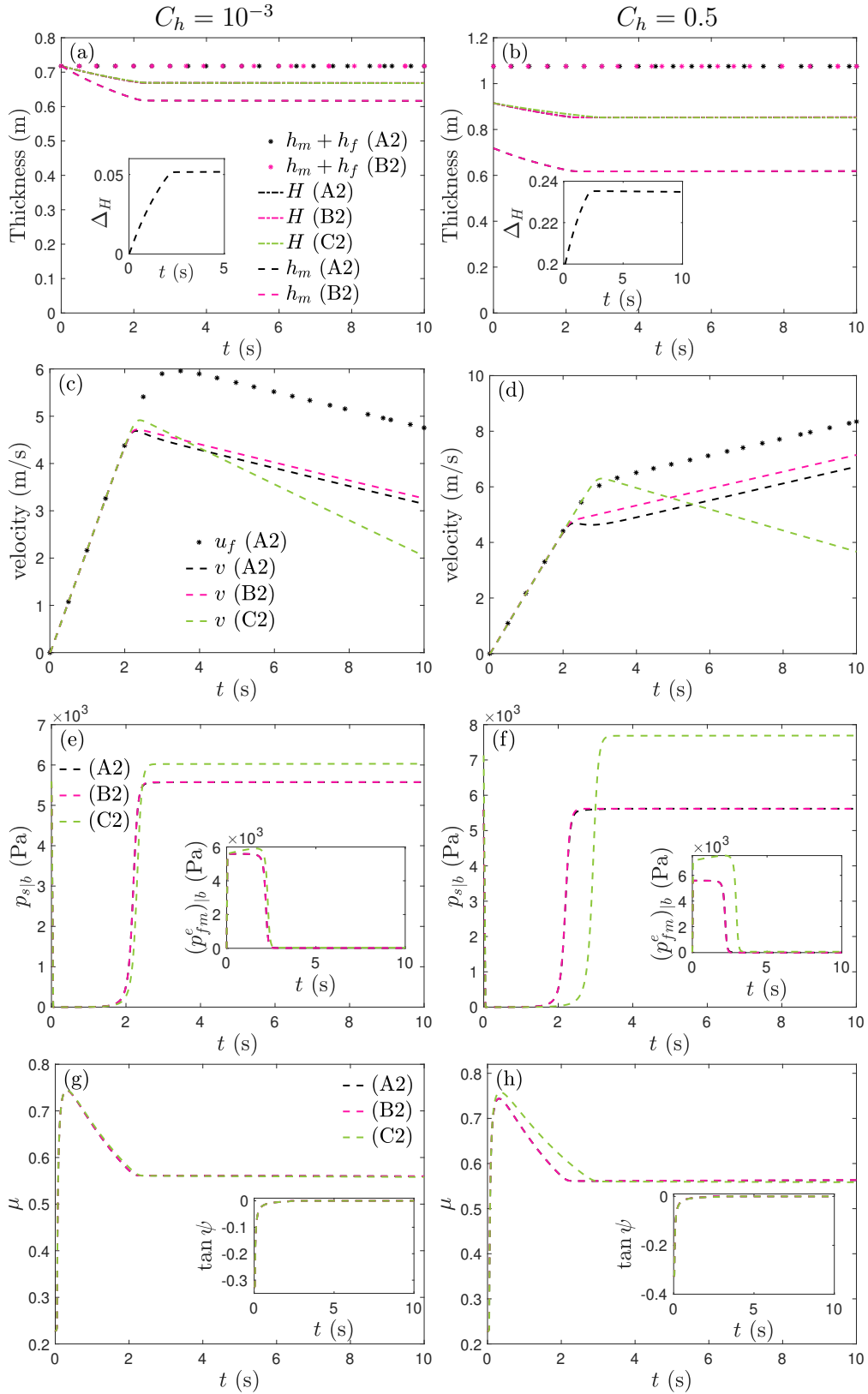


Figure 16: Loose case with slope angle $\theta = 13^\circ$ for $C_h = 10^{-3}$ (left column) and $C_h = 0.5$ (right column). Comparison between the models for which $u = v$ in the mixture: the two-layer models (A2), (B2) and the one-layer model with virtual thickness (C2). (a)-(b) Virtual thickness H for all models and, for (A2) and (B2), mixture thickness h_m and total thickness $h_m + h_f$, (c)-(d) mixture velocity $V_m = v$ and, for model (A1), velocity of the fluid upper-layer u_f , (e)-(f) basal solid pressure $p_{s|b}$ with basal excess pore pressure $(p_{f_m}^e)|_b$, and (g)-(h) friction coefficient μ with dilatancy $\tan \psi$.

with the fluid exchange at the mixture surface f_{transf} , calculated in model (A2), is small in all cases. The drag force between the mixture and the upper fluid is significant and the basal fluid friction is negligible.

5.3.4 Influence of φ^0 and η_f

The value $\varphi^0 = 0.48$ that we used in the previous tests is quite far from the critical state volume fraction $\varphi_c = 0.56$. Let us investigate what happens for closer values $\varphi^0 = 0.54$ or $\varphi^0 = 0.545$ (figure 19) in the loose case. The difference between the one-layer model (C2) and the two-layer models (A2) and (B2) is even greater. For example, for $\varphi^0 = 0.545$, the mass does not start to move with (C2) as opposed to the other models. Indeed, the basal excess pore pressure is almost equal to zero which is not the case for the other models. For $\varphi^0 = 0.54$, the behavior of the models is closer but the higher basal frictional stress makes the mass in model (C2) stop earlier. Note that the shift between the basal solid pressure is large between models (A2) and (B2) $\varphi^0 = 0.545$ (figure 19d).

In the tests in the debris flow configuration, we only considered the fluid viscosity $\eta_f = 10^{-3}$ Pa s. We also tested a larger value $\eta_f = 10^{-2}$ Pa s. The qualitative behavior of the results remains the same. However, the time evolution is longer for higher viscosity. For example, in the loose case, the excess pore pressure vanishes in 2 seconds for $\eta_f = 10^{-3}$ Pa s whereas it does not vanish until 20 seconds for $\eta_f = 10^{-2}$ Pa s. As a result, the velocity reaches its maximum at ~ 5 m/s for $\eta_f = 10^{-3}$ Pa s and ~ 35 m/s for high viscosity.

6 Conclusion

We propose here a depth-averaged shallow model with a mixture layer and a fluid-only upper layer that solves the solid (granular) and fluid velocities in the mixture as well as the upper layer velocity. This model, derived from [7], is supplemented by an improved rheology coming from the recent work of [55] and more general boundary conditions. It accounts for dilatancy in the granular mass (compression/dilatation), for its impact on the excess pore fluid pressure and the retro-action on the basal frictional stress experienced by the grains. Dilatancy is accounted for based on the concepts of critical state mechanics that describes the flow behavior as a function of its deviation from the critical state which is reached at the equilibrium. Dilatancy may drastically change the flow dynamics and deposits, as widely known, leading to very different behaviors for an initially loose (solid volume fraction lower than in the critical state) or an initially dense granular layer, as illustrated in our simulations. We also observed that, in some cases, dilatancy generates a friction weakening effect at the beginning of the flow that would not otherwise exist.

Based on this complete two-layer three-velocity model, we rigorously derive simpler models with different levels of complexity. We either reduce the two-layer model to one-layer models through the introduction of a virtual thickness, as in the Iverson and George [23] or Meng and Wang [35] models, or we assume that the solid and fluid velocities in the mixture are the same, as also done for example in the Iverson-George model. We clearly describe the assumptions made to obtain the resulting six models. We also discuss two different ways of calculating the excess pore fluid pressure, which is a key parameter in these models.

We show that one-layer models, such as the Iverson-George model, do not give any information on the conservation of the solid and fluid mass or volume since the virtual interface is not a real surface. Even if the total mass is conserved, the solid or the fluid may pass through the virtual surface during dilation or contraction [23]. It follows that we cannot ensure that

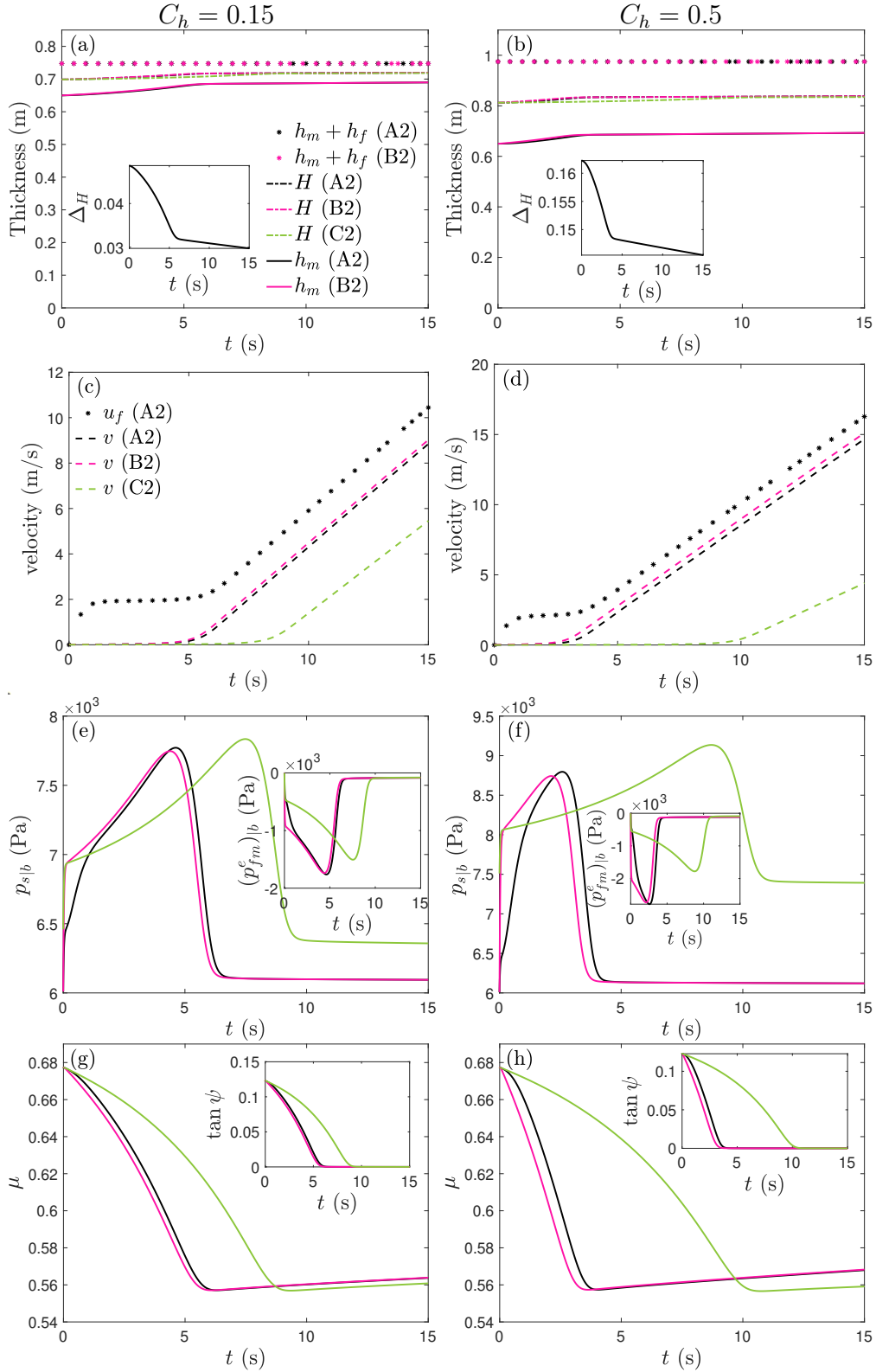


Figure 17: Dense case with slope angle $\theta = 20^\circ$ for $C_h = 0.15$ (left column) and $C_h = 0.5$ (right column). Comparison between the models for which $u = v$ in the mixture: the two-layer models (A2), (B2) and the one-layer model with virtual thickness (C2). (a)-(b) Virtual thickness H for all models and, for (A2) and (B2), mixture thickness h_m and total thickness $h_m + h_f$, (c)-(d) mixture velocity $V_m = v$ and, for model (A1), velocity of the fluid upper-layer u_f , (e)-(f) basal solid pressure $p_{s|b}$ with basal excess pore pressure $(p_{fm}^e)_{|b}$, and (g)-(h) friction coefficient μ with dilatancy $\tan \psi$.

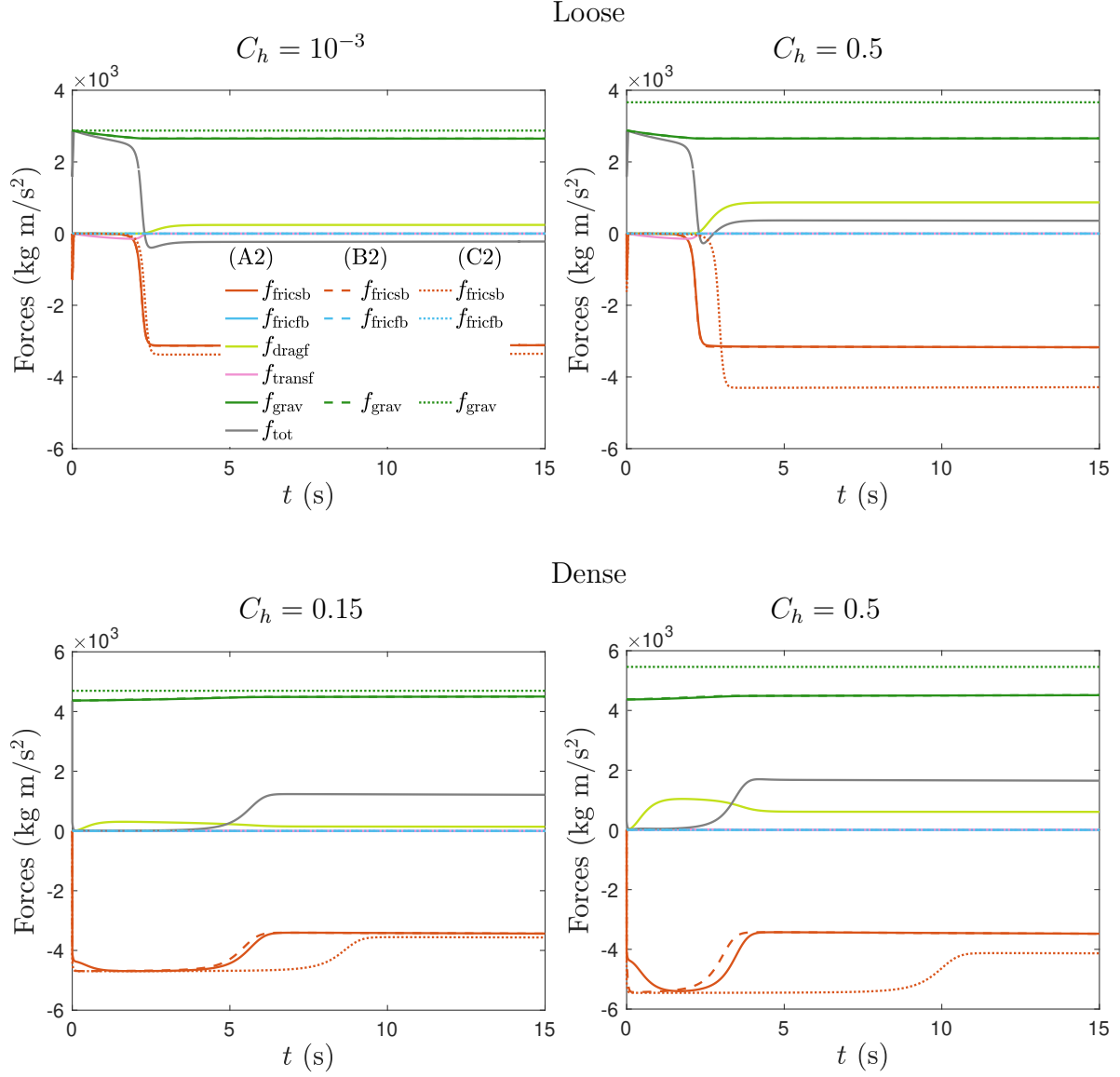


Figure 18: Forces involved in the model in the loose case with slope angle $\theta = 13^\circ$ (first row) and in the dense case with slope angle $\theta = 20^\circ$ (second row) for $C_h = 10^{-3}$ (left column) and $C_h = 0.5$ (right column). The forces are the basal solid friction f_{fricsb} , the basal fluid friction f_{fricfb} , the drag of the mixture with the upper fluid layer f_{dragf} , the force associated with the fluid transfer f_{transf} , the force of gravity f_{grav} , and the sum of all these forces f_{tot} representing the mass acceleration (see table 6).

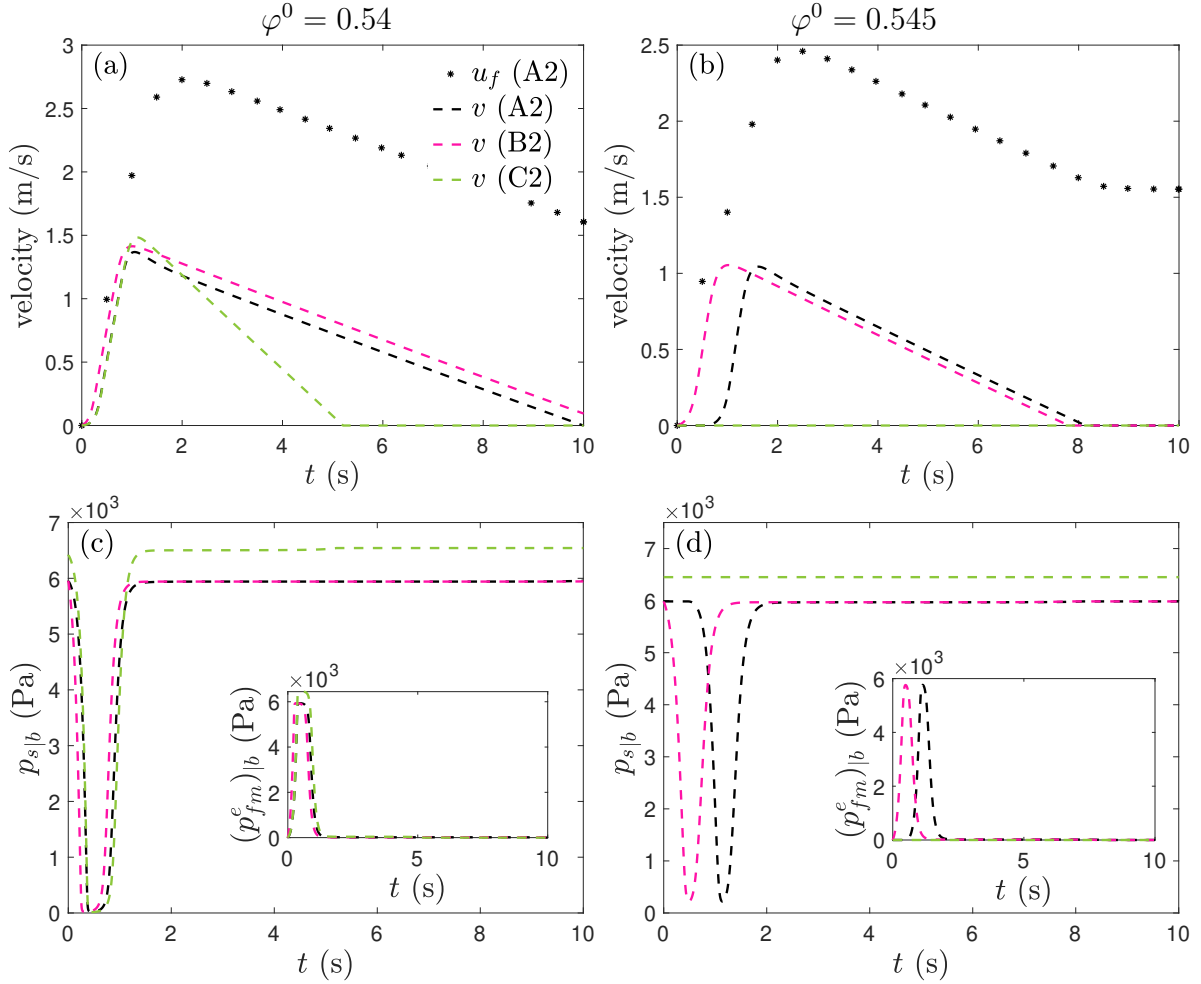


Figure 19: Loose case with slope angle $\theta = 13^\circ$ for $\varphi^0 = 0.54$ (left column) and $\varphi^0 = 0.545$ (right column). Comparison between the models for which $u = v$ in the mixture: the two-layer models (A2), (B2) and the one-layer model with virtual thickness (C2). (a)-(b) mixture velocity $V_m = v$ and, for model (A1), velocity of the fluid upper-layer u_f , (c)-(d) basal solid pressure $p_{s|b}$ with basal excess pore pressure $(p_{fm}^e)_{|b}$.

the total solid and fluid masses are conserved in the Iverson-George model. On the contrary, our two-layer models with either one or two velocities in the mixture naturally account for the fluid mass expelled by or sucked from the mixture and conserves the total solid and fluid masses. However these two-layer models are not valid when the water level is under the granular material upper surface (under-saturated case) while one-layer models with their virtual surface may in principle deal with this situation as claimed in [23]. Furthermore the equations of the one-layer model with equal solid and fluid velocity in the mixture are much simpler, which represents a strong advantage for their numerical implementation and for field applications.

We performed a series of simulations to compare all these models in a uniform configuration by varying the rheology and parameter sets in two cases with the objective of identifying the performance and limits of the simpler models. First, we simulated immersed granular flows, mimicking submarine landslides with an upper horizontal water surface, and then idealized debris flows with a fluid layer parallel to the mixture layer. A key conclusion of our work is that the models are extremely sensitive to the rheology and associated parameters, to the permeability (grain diameter and viscosity), and to the initial volume fraction. As a result, the flow behavior and in particular the velocities strongly depend on parameters that are very hard to measure in the field, showing that sensitivity analysis should be necessarily associated with field-scale simulations.

Comparison of two-layer models solving for the fluid and solid velocities in the mixture with models assuming equality of these velocities shows that such an assumption is only valid for low permeability (grain diameter $d = 10^{-3}$ m leading to permeability $k = 1.8 \times 10^{-9}$ m²). However, when the permeability is increased ($d = 10^{-2}$ m leading to 1.1×10^{-7} m²), we show that it is necessary to account for different solid and fluid velocities. For one-layer models, we observe far greater differences between the models with different or equal solid and fluid velocities in the mixture, even for low permeability. Assuming that the velocity in the upper fluid layer is related to the mixture velocity instead of calculating this velocity leads to comparable behavior when the permeability is low ($d = 10^{-3}$ m) but can lead a 25% of difference in the calculated velocities for $d = 10^{-2}$ m for example.

Another key point concerns the validity of one-layer models involving a virtual thickness, such as the Iverson and George and Meng and Wang models. We show here that the results can strongly differ from those of the complete model. For example, in some simulated cases, the friction in the one-layer one-velocity model is larger than in the two-layer one-velocity model, causing the mass to stop much earlier in the one-layer one-velocity model. The one-layer models however provide a rough approximation of the two-layer models when the permeability is low, the initial volume fraction is not too close to the critical volume fraction, and the upper fluid layer is very thin (for example 10^{-3} times the thickness of the mixture layer). As a result, for high permeability and/or when the upper layer is thick (for example 0.5 times the thickness of the mixture layer), one-layer models with a virtual thickness may lead to huge errors in the prediction of flow dynamics and deposits. In such cases, it is crucial to derive two-layer models that account for an upper layer made either of fluid or grains.

Our results demonstrate the huge challenge remaining before field-scale debris flows or submarine landslides can be simulated at a reasonable computational cost with depth-averaged models applicable at the field scale with a reasonable computational cost is still a huge challenge.

Acknowledgements

The authors warmly thank E. Guazzelli for fruitful discussions concerning the models. This work was possible thanks to IPGP and University Gustave-Eiffel financial supports for exchanges

between France and Spain. E.D. Fernández-Nieto and G. Narbona-Reina thank the National Spanish grant PID2022-137637NB-C22 funded by MCIN/AEI/10.13039/501100011033 and by “ERDF A way of making Europe”, for financial support. This work was also funded by ERC-CG-2013-PE10-617472 SLIDEQUAKES and DT-GEO European projects.

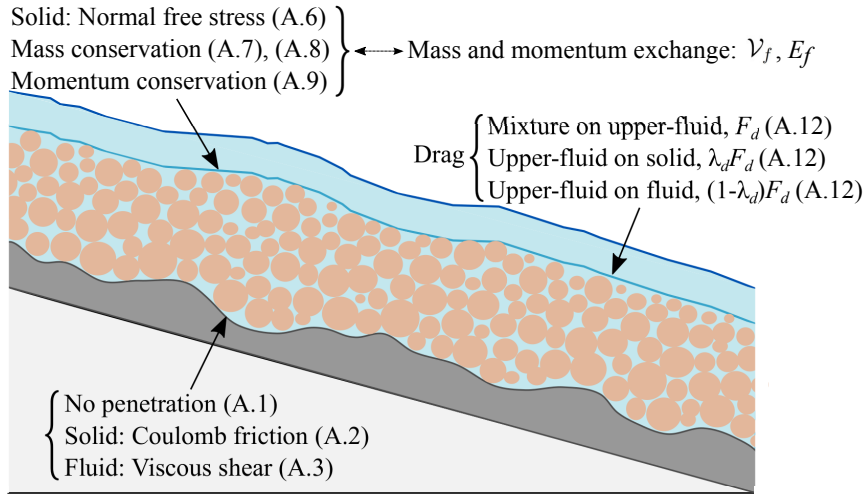


Figure 20: Summary of the boundary conditions at the bottom and at the interface between the mixture and upper fluid layers for the full two-layer model with three velocities (A1) and references to the corresponding equations. Additionally, a kinematic and stress-free condition for the upper-fluid is considered at the free surface, given in (A.4), (A.5).

A Two-layer three-velocity model (A1) modified from [7]

The models presented here are derived from our previous work [7] with slight modifications concerning the rheology and the boundary conditions at the bottom and at the interface between the mixture and the upper fluid layer. Note that the modification of the interface conditions does not affect the one velocity models presented in Section 3 since the associated terms disappear when the total momentum conservation is written. The updated rheology is presented in Section 2.2. We first summarize here the boundary conditions considered for the whole 3D problem and then we focus on the modified conditions at the bottom and at the interface. We also discuss different alternatives proposed in the literature for these boundary conditions. We then write the energy balance of the modified model. Finally, we develop the derivation of the pressure evolution equation (2.26) presented in section 2.3.2.

A.1 Summary of boundary conditions

A summary of the boundary conditions considered for the full two-layer model domain is depicted in figure 20. We use the bold font to denote 3D vectors and the subscript “tg” for the tangential projection of a vector, that is $\mathbf{w}_{\text{tg}} = \mathbf{w} - (\mathbf{w} \cdot \mathbf{N}_X)\mathbf{N}_X$, for any vector \mathbf{w} and any normal N_X . See notation in figure 21. Details are given below in Appendix sections A.2 and A.3.

At the bottom we impose a no-penetration condition for the two phases,

$$\mathbf{u} \cdot N_X^b = \mathbf{v} \cdot N_X^b = 0, \quad (\text{A.1})$$

together with a Coulomb type friction law for the solid and a viscous shear for the fluid,

$$(\sigma_s N_X^b)_{\text{tg}} = -\mu \text{sgn}(\mathbf{v})(\sigma_s N_X^b) \cdot N_X^b, \quad (\text{A.2})$$

$$(\sigma_{f_m} N_X^b)_{\text{tg}} = \frac{5}{2} \frac{\eta_e(1-\varphi)}{h_m} \mathbf{u}_{\text{tg}}, \quad (\text{A.3})$$

with $\eta_e = \eta_f(1 + \frac{5}{2}\varphi)$ the effective fluid viscosity.

At the free surface the kinematic condition is considered for the top fluid velocity

$$\partial_t(b + h_m + h_f) + \mathbf{u}_f \cdot N_X^{\text{surf}} = 0, \quad (\text{A.4})$$

and a stress-free condition

$$\sigma_f N_X^{\text{surf}} = 0. \quad (\text{A.5})$$

At the mixture/fluid interface we consider that the normal component of the normal stress vanishes and the kinematic conditions for the solid phase

$$(\sigma_s N_X^i) \cdot N_X^i = 0, \quad (\text{A.6})$$

$$\partial_t(b + h_m) + \mathbf{v} \cdot N_X^i = 0. \quad (\text{A.7})$$

The conservation of the fluid mass is given by the following relation where we also introduce the fluid transfer rate \mathcal{V}_f ,

$$\mathcal{V}_f \equiv \partial_t(b + h_m) + \mathbf{u}_f \cdot N_X^i = (1 - \varphi)(\partial_t(b + h_m) + \mathbf{u} \cdot N_X^i). \quad (\text{A.8})$$

We impose the total momentum conservation

$$\rho_f \mathcal{V}_f (\mathbf{u}_f - \mathbf{u}) + (\sigma_s + \sigma_{f_m}) N_X^i = \sigma_f N_X^i, \quad (\text{A.9})$$

where the stress tensors are $\sigma_j = -p_j \text{Id} + \sigma'_j$, for $j = s, f_m, f$. In order to determine the tangent component of the stress tensor at the interface for each constituent, two more conditions are needed. First we denote by E_f the tangential projection of the flux of fluid momentum through the interface appearing in the first term of (A.9),

$$E_f = \rho_f \mathcal{V}_f (\mathbf{u}_f - \mathbf{u})_{\text{tg}}. \quad (\text{A.10})$$

Then, we introduce a drag between the fluid in the upper layer and the mixture

$$F_d = k_f (\mathbf{u}_f - \mathbf{V}_m)_{\text{tg}}, \quad (\text{A.11})$$

where the 3D mixture velocity is $\mathbf{V}_m = \frac{1}{\rho}(\rho_s \varphi \mathbf{v} + \rho_f (1 - \varphi) \mathbf{u})$. The distribution of the fluid transfer (E_f) and of the drag (F_d) components is made through two distribution coefficients λ_f and λ_d respectively in such a way that

$$\begin{aligned} (\sigma_s N_X^i)_{\text{tg}} &= \lambda_d F_d, \\ (\sigma_{f_m} N_X^i)_{\text{tg}} &= (1 - \lambda_d) F_d - \lambda_f E_f, \\ (\sigma_f N_X^i)_{\text{tg}} &= F_d + (1 - \lambda_f) E_f. \end{aligned} \quad (\text{A.12})$$

They are defined as

$$\begin{aligned} \lambda_d &= \frac{\varphi \rho_s}{\rho}, \\ \lambda_f &= \frac{1}{2} - \frac{1}{2} \text{sgn}(\mathcal{V}_f) \delta_f, \quad \delta_f = \begin{cases} 0 & \text{centered distribution,} \\ 1 & \text{upwind distribution.} \end{cases} \end{aligned} \quad (\text{A.13})$$

To summarize, if $\delta_f = 0$ the fluid velocity at the interface is $(\mathbf{u} + \mathbf{u}_f)/2$, while if $\delta_f = 1$, it is given in terms of the sign of \mathcal{V}_f . Thus, if the fluid is expelled from the mixture (contraction), $\mathcal{V}_f > 0$, $\lambda_f = 0$ so that the velocity is \mathbf{u} . On the contrary, if the fluid is sucked into the mixture (dilation), $\mathcal{V}_f < 0$, $\lambda_f = 1$ and the velocity is \mathbf{u}_f .

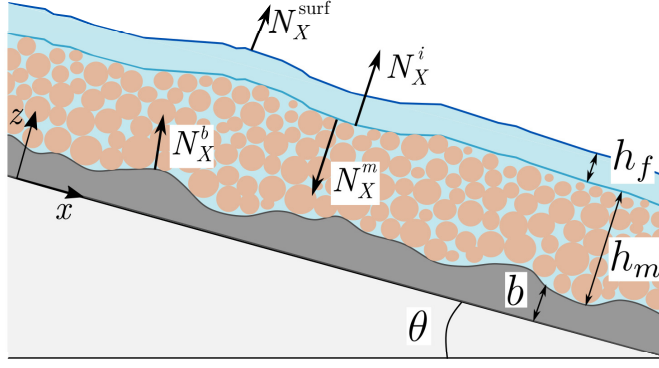


Figure 21: Notations for two-layer models (groups A and B).

A.2 Fluid viscous shear at the bottom

In the model proposed in [7], viscosity effects are neglected in the total stress tensor but are present in the form of a friction boundary condition specified in the xz component of the stress tensors at the base of the flow. On the contrary the Iverson-George model [23] considered the viscous stress at the bottom. The basal friction condition for the fluid phase used in [7] was established as

$$(\sigma_{f_m} N_X^b)_{\text{tg}} = k_b \mathbf{u}_{\text{tg}} + O(\epsilon^3) \quad \text{at the bottom.} \quad (\text{A.14})$$

If we consider $\sigma_{f_m} = -p_{f_m} \text{Id} + \sigma'_{f_m}$ with $\sigma'_{f_m} = 2(1 - \varphi)\eta_e D(\mathbf{u})$, for η_e the effective fluid viscosity and $D(\mathbf{u})$ the fluid strain rate tensor, we obtain that $(\sigma_{f_m} N_X^b)_{\text{tg}} = \sigma_{f_m}^{xz} = (1 - \varphi)\eta_e \partial_z u + O(\epsilon^3)$ when $\eta_e = O(\epsilon^2)$. By approximating $\partial_z u|_b \sim c_b u/h_m$, for some constant c_b we write

$$(1 - \varphi)\eta_e c_b \frac{u}{h_m} = k_b u + O(\epsilon^3) \quad \text{at the bottom,}$$

leading to $k_b = c_b \frac{\eta_e(1 - \varphi)}{h_m}$. This expression is similar to the one considered by Iverson and George in [23] given by τ_f in equation (3.17a) for $c_b = 2$ and $h_m \sim h$. For consistency with our approximation of the shear rate, we consider in this work $c_b = \frac{5}{2}$, then following (A.14) the coefficient k_b reads

$$k_b = \frac{5}{2} \frac{\eta_e(1 - \varphi)}{h_m}, \quad \text{with} \quad \eta_e = \eta_f(1 + \frac{5}{2}\varphi), \quad (\text{A.15})$$

that gives (A.3). We discuss other alternatives in section A.4.1.

Note that the effect of fluid viscosity is also present in the viscous number J . As the empirical relation defining J is usually built up from lab-scale experiments, it is hard to discriminate between the fluid viscous term and the solid-fluid drag. As a result as to whether this fluid friction has to be added in the equations involving a rheology with viscous-inertial numbers fitted on lab-experiments is still an open issue [E. Guazzelli, personal communication].

A.3 Drag at the upper-fluid/mixture interface

At the interface between the upper fluid layer and the mixture, exchange of fluid mass occurs and corresponds to \mathcal{V}_f . When $\mathcal{V}_f > 0$, the fluid is expelled from the mixture towards the fluid-only region. In figure 21 we specify the notation of the normal vectors in the domain. We remind that the 3D velocities are $\mathbf{v} = (v, v^z)$, $\mathbf{u} = (u, u^z)$, $\mathbf{u}_f = (u_f, u_f^z)$.

In [7] the drag between the two layers reduced to the drag force between the fluid phases in the

upper and mixture layers and it was written as $k_f(\mathbf{u}_f - \mathbf{u})$ with $k_f \geq 0$ a friction coefficient. It seems however more suitable to consider instead a drag between the upper fluid and the mixture as a whole. We thus specify

$$F_d = k_f(\mathbf{u}_f - \mathbf{V}_m)_{\text{tg}}, \quad (\text{A.16})$$

where $(\mathbf{V}_m)_{\text{tg}}$ is the value of the tangent component of the 3D velocity of the mixture at the interface. Note that we must decide which part of this drag stress is experienced by each of the phases in the mixture. Let us denote F_{d_s} and F_{d_f} , the drag exerted by the upper-fluid on the solid and fluid phase in the mixture, respectively. Then $F_d = F_{d_f} + F_{d_s}$ is split into these two components:

$$F_{d_s} = \lambda_d F_d \quad \text{and} \quad F_{d_f} = (1 - \lambda_d) F_d, \quad (\text{A.17})$$

for some non-negative coefficient λ_d . In order to obtain a dissipative contribution to the energy of the system (see (A.26)), this coefficient must be taken such that $\mathbf{V}_m = \lambda_d \mathbf{v} + (1 - \lambda_d) \mathbf{u}$. Then we propose to take the distribution parameter as the relative solid density,

$$\lambda_d = \frac{\varphi \rho_s}{\rho}. \quad (\text{A.18})$$

In this case, the contribution to the energy is given by the term, $-k_f |u_f - V_m|^2$. As in [7], the conservation of the total momentum is given in (A.9) and E_f in (A.10) is the tangential flux of fluid momentum through the interface. If we write the tangent component of (A.9) it reads

$$(\sigma_f N_X^i)_{\text{tg}} - (\sigma_s N_X^i)_{\text{tg}} - (\sigma_{f_m} N_X^i)_{\text{tg}} = E_f.$$

Taking into account $N_X^m = -N_X^i$ (see figure 21) it becomes

$$(\sigma_f N_X^i)_{\text{tg}} + (\sigma_s N_X^m)_{\text{tg}} + (\sigma_{f_m} N_X^m)_{\text{tg}} = E_f.$$

We see that there is a contribution to the shear stress due to the fluid flux at the interface related to E_f . How E_f should be distributed between the different fluid stresses $(\sigma_f N_X^i)_{\text{tg}}, (\sigma_{f_m} N_X^m)_{\text{tg}}$ is an open question and should be further studied. See discussion in section A.4.2. In general we consider a non-negative distribution coefficient λ_f in such a way that $(1 - \lambda_f) E_f$ is the part of the fluid flux applied by the upper-fluid on the whole mixture. Thus, we assume that the tangential stress applied by the upper-fluid to the mixture at the interface entails the drag stress and part of the fluid mass exchange given by $(1 - \lambda_f) E_f$:

$$\sigma_{\text{tg}}^{\text{on mix}} = (\sigma_f N_X^i)_{\text{tg}} = (\sigma_f N_X^i) - ((\sigma_f N_X^i) \cdot N_X^i) N_X^i = F_d + (1 - \lambda_f) E_f. \quad (\text{A.19a})$$

On the other hand, the stress exerted to the upper fluid layer by the mixture comes from the grain and fluid phases. The contribution of the fluid phase is given by the addition of the drag F_{d_f} and the corresponding fluid mass exchange to ensure (A.9),

$$\sigma_{\text{tg}}^{\text{on up fluid, f}} = (\sigma_{f_m} N_X^m)_{\text{tg}} = (\sigma_{f_m} N_X^m) - ((\sigma_{f_m} N_X^m) \cdot N_X^m) N_X^m = -(1 - \lambda_d) F_d + \lambda_f E_f. \quad (\text{A.19b})$$

The contribution of the solid phase at the interface in the tangent direction (considering $N_X^m = -N_X^i$) is instead just given by the corresponding drag F_{d_s} ,

$$\sigma_{\text{tg}}^{\text{on up fluid, s}} = (\sigma_s N_X^m)_{\text{tg}} = (\sigma_s N_X^m) - ((\sigma_s N_X^m) \cdot N_X^m) N_X^m = -\lambda_d F_d. \quad (\text{A.19c})$$

We notice that adding (A.19a), (A.19b) and (A.19c) we recover (A.9), taking into account that $N_X^m = -N_X^i$. Therefore only two of the three equations (A.19a), (A.19c), (A.19b) are necessary since the last one can be obtained from the tangent part of (A.9).

We will take here two possible distributions, called centered and upwind with respect to the sign of the fluid mass flux $\rho_f \mathcal{V}_f$ and defined by the distribution coefficient λ_f , that may depend on dilation/contraction, as

$$\lambda_f = \frac{1}{2} - \frac{1}{2} \operatorname{sgn}(\mathcal{V}_f) \delta_f, \quad \delta_f = \begin{cases} 0 & \text{centered distribution,} \\ 1 & \text{upwind distribution.} \end{cases} \quad (\text{A.20})$$

In figure 22 we present a schematic view of the implications of this definition.

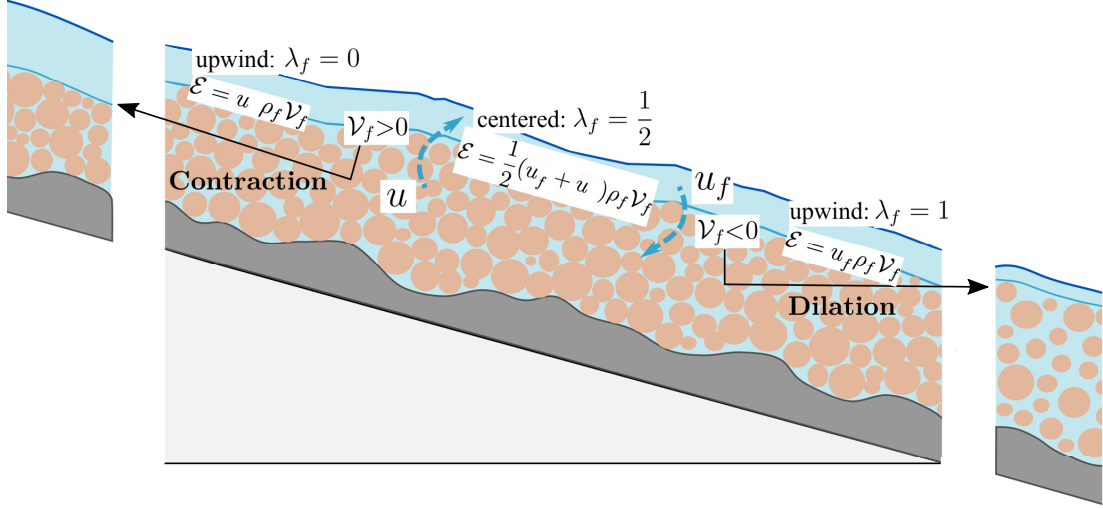


Figure 22: Tangent fluid momentum distribution at the interface. When $\mathcal{V}_f > 0$ the fluid is transferred from the mixture to the upper-fluid layer, thus the interface goes down (picture on the left). When $\mathcal{V}_f < 0$ the fluid is transferred from the upper-fluid layer to the mixture, and the interface goes up (picture on the right). $\mathcal{E} = ((1 - \lambda_f)u + \lambda_f u_f) \rho_f \mathcal{V}_f$ represents the term appearing in the momentum equation for each phase (see equations (2.14b) and (2.14c))

For the centered choice, $\lambda_f = 1/2$, the term E_f is equally distributed between the stresses exerted on both layers by one layer to the other. In the upwind approximation $\lambda_f = 0$ when $\mathcal{V}_f > 0$, *i.e.* in case of contraction when the fluid is transferred from the mixture to the upper fluid layer (picture on the left side in figure 22). The term E_f thus only contributes to the stress applied by the upper-fluid to the mixture at the interface and just appears in $\sigma_{\text{tg}}^{\text{on mix}} = (\sigma_f N_X^i)_{\text{tg}}$. On the contrary, when the granular mass dilates $\mathcal{V}_f < 0$ which means that the fluid is sucked by the mixture layer from the upper fluid layer, $\lambda_f = 1$ and thus the term E_f only contributes to the stress applied by the fluid mixture to the upper-fluid at the interface (picture on the right side in figure 22). As a result, it just appears in $\sigma_{\text{tg}}^{\text{on up fluid, f}} = (\sigma_{f_m} N_X^m)_{\text{tg}}$. The corresponding term appearing in the energy equation is calculated as

$$\left(\lambda_f - \frac{1}{2} \right) \rho_f \mathcal{V}_f |u_f - u|^2 = -\frac{1}{2} \delta_f \rho_f |\mathcal{V}_f| |u_f - u|^2. \quad (\text{A.21})$$

This choice thus ensures a dissipative contribution to the energy balance. In particular for the centered distribution no contribution is made to the energy since $\delta_f = 0$. Although to our knowledge, there is no measurements or physical reasons to choose one of these approximations (or even others), these choices lead to a dissipative or to no contribution in the energy balance of the derived model (see equation (A.26)).

The resulting term describing the fluid mass exchange in the depth-averaged model is given by $\mathcal{E} = ((1 - \lambda_f)u + \lambda_f u_f)\rho_f \mathcal{V}_f$, appearing in the momentum equations of the fluid in the mixture (2.14b) and in the upper layer (2.14c)). We see that the distribution coefficient λ_f finally describes the velocity at the interface, given as a convex combination of the fluid in the upper-fluid layer and the fluid in the mixture, $(1 - \lambda_f)u + \lambda_f u_f$, see figure 22. Under this interpretation, we think that the better choice is to consider the averaged velocity, that is, $\frac{1}{2}(u_f + u)$, given by the centered approximation $\lambda_f = \frac{1}{2}$, as in our previous work [7].

It should be pointed out here that the issue of prescribing physically meaningful conditions at this interface comes from the depth-averaged processes that requires to link discontinuous depth-averaged quantities at an interface (see figure 23). However, in a real 3D situation the fluid is a continuous media and there is no discontinuity of the velocity as illustrated in figure 23, that shows an example of a real velocity profile and of the averaged velocity of the fluid in the mixture u and in the upper-fluid layer u_f . A similar problem occurs when trying to describe erosion/deposition processes (static/flowing interface) in depth-averaged models (see *i.e.* [5]). For this reason, one-layer models that imply adding these interface conditions (they thus do not appear anymore), eliminate these approximations.

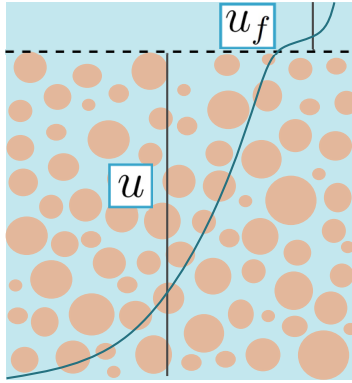


Figure 23: Illustration of the real velocity profile in the fluid phase in blue and depth-averaged fluid velocities u and u_f considered in the two-layer depth-averaged models.

A.4 Alternative descriptions proposed in the literature

We present here similar conditions considered in the literature, other than in the Iverson and George and Meng and Wang models that have been thoroughly analyzed in this paper (see also section D.2 for a detailed comparison of the boundary conditions with the Meng-Wang model). We analyze three descriptions that are relevant in the model, namely, the viscous shear, the drag and exchange conditions at the mixture/upper-fluid interface, and the inter-phase drag between solid and fluid phases in the mixture. In particular we study the works in [29, 34, 54, 4].

For the reader convenience we briefly remind the main characteristics of the models proposed in those papers. In [29] a 2D depth-averaged two-layer model for over-saturated debris flows taking into account the bottom curvature is presented. The model accounts for two velocities in the mixture and one independent velocity for the upper-fluid layer, as in our full model (A1). Nevertheless dilatancy effects and rheology are not considered. In [34] a 1D depth-averaged model for debris flows is proposed dealing with transitions from pure fluid/solid configurations to under-saturated or over-saturated mixture. This model also does not account for dilatancy, rheology nor mass exchange. In [54] a 1D depth-averaged two-phase model is presented for

submarine avalanches. This model takes into account the dilatancy and mass exchange, it considers one velocity for the mixture and an independent velocity for the upper-fluid layer, as in our model (A2). Finally, in [4] a 3D two-phase model for fluid saturated sediment is presented from the Jackson's equations. To close the system a thermodynamic analysis of a two-phase mixture, for elastic-plastic granular solid in a viscous fluid is performed. The model accounts for mixture rheology and dilatancy effects. This model is especially relevant for the closures of the 3D starting model (Jackson's model), namely the viscous tensor and the inter-phase friction. Moreover, as said in section 2.3.2, the evolution equation for the solid pressure presented here is inspired by this work.

A.4.1 Fluid viscous stress and basal fluid shear stress at the bottom

In section A.2 we introduced a way to take into account the fluid viscosity in our depth-averaged model through the approximation of the viscous fluid stress at the bottom in the corresponding boundary condition, as proposed in [23]. The total stress is defined as $\sigma_{f_m} = -p_{f_m}\text{Id} + \sigma'_{f_m}$ with $\sigma'_{f_m} = 2(1 - \varphi)\eta_e D(\mathbf{u})$, for η_e the effective fluid viscosity. The boundary condition then reading

$$(\sigma_{f_m} N_X^b)_{\text{tg}} = \frac{5(1 - \varphi)\eta_e}{2h_m} \mathbf{u}_{\text{tg}} \quad \text{at the bottom.}$$

In [29] the fluid viscosity is neglected and a quadratic friction law is considered at the bottom, namely $(\sigma_{f_m} N_X^b)_{\text{tg}} = c_b(1 - \varphi)\mathbf{u}\|\mathbf{u}\|$ with c_b a constant coefficient. In contrast, in models proposed in [34, 54] the downslope component of the fluid viscous stress is kept in the depth-averaged model, providing the term $\partial_x(h_m 2\eta_f(1 - \varphi)\partial_x u)$. In that case, the viscous shear at the bottom is not considered. In [54] no drag for the fluid at the bottom is considered, so this term is just neglected. In [34] the viscous shear at the bottom is replaced with a Chézy drag, $(\sigma_{f_m} N_X^b)_{\text{tg}} = C_{\text{Ch}}\rho_f\mathbf{u}\|\mathbf{u}\|$ with C_{Ch} a Chézy drag coefficient. As explained in section 4.4.2 this choice, also considered in [35], seems to be inconsistent when viscosity is taking into account in the model. The use of the effective viscosity in the stress tensor is also considered in [4] for their 3D model.

A.4.2 Drag and mass exchange at the interface

These interface conditions have been described and discussed in section A.3 (equations (A.10)-(A.13)). We present here alternative conditions considered in the literature for similar models, namely in [29, 34, 54].

Let us begin with the over-saturated mixture model proposed in [29]. At the interface, the conservation of the total momentum (A.9) is considered and in particular the stress of the upper layer is distributed in terms of the solid volume fraction, such that³

$$\sigma_{f_m} N_X^i = (1 - \varphi)(\sigma_f N_X^i) - \rho_f \mathcal{V}_f(\mathbf{u}_f - \mathbf{u}), \quad \sigma_s N_X^i = \varphi(\sigma_f N_X^i). \quad (\text{A.22})$$

Notice that, unlike in our model (equations (A.12)), the distribution is performed for the total stress and not only for the tangential component. This has an important impact on the calculated pressures, as detailed below. Additionally, the following friction law at the interface is proposed (see equation (103) in that paper)

$$(\sigma_f N_X^i)_{\text{tg}} = C|(\mathbf{u}_f - \mathbf{V})_{\text{tg}}|(\mathbf{u}_f - \mathbf{V})_{\text{tg}} = F_d^{\text{Luca}}$$

³With the notation in [29], $\mathcal{M}_{int} = \rho_f \mathcal{V}_f$, $v_2 = u_f$, $v = \varphi$, so $E_f = -\mathcal{M}_{int}(u - v_2)_{\text{tg}}$. See their equations (22)-(24) and (37)-(38).

for a constant coefficient C and with $\mathbf{V} = \varphi \mathbf{v} + (1 - \varphi) \mathbf{u}$, that also differs from our mixture velocity $\mathbf{V}_m = \frac{1}{\rho}(\rho_s \varphi \mathbf{v} + \rho_f (1 - \varphi) \mathbf{u})$. If we write the tangential components of these expressions we find that

$$\begin{aligned} (\sigma_s N_X^i)_{\text{tg}} &= \varphi F_d^{\text{Luca}}, \\ (\sigma_{f_m} N_X^i)_{\text{tg}} &= (1 - \varphi) F_d^{\text{Luca}} - E_f, \\ (\sigma_f N_X^i)_{\text{tg}} &= F_d^{\text{Luca}}. \end{aligned} \quad (\text{A.23})$$

When compared with our conditions (A.12), we find that $\lambda_d^{\text{Luca}} = \varphi$ and $\lambda_f^{\text{Luca}} = 1$. Their definition of the distribution parameter λ_d , representing the contribution of the drag to the solid phase, follows the same idea than in our equations (A.17)-(A.18). In our case $\lambda_d = \varphi \rho_s / \rho$ which is the coefficient related to the solid velocity \mathbf{v} in the expression of our mixture velocity \mathbf{V}_m . Analogously, $\lambda_d^{\text{Luca}} = \varphi$ corresponds to the coefficient before \mathbf{v} in their mixture velocity \mathbf{V} . This choice ensures a dissipative contribution to the energy in their model with the term $-C|u_f - V|^3$.

On the contrary, the choice $\lambda_f^{\text{Luca}} = 1$ does not ensure a dissipative contribution to the energy related to the fluid exchange. Following (A.21) the corresponding term appearing in the energy equation would be

$$\frac{1}{2} \rho_f \mathcal{V}_f |u_f - u|^2.$$

This term does not have a fixed sign since it depends on the sign of \mathcal{V}_f . Furthermore, in view of (A.23), the value λ_f^{Luca} does not distribute the fluid mass between the two fluid tangent tensors since it is only present in the mixture fluid tensor σ_{f_m} , thus preventing a description of the case where the fluid goes out from the mixture. Following (A.20) it seems that the only considered case is the dilation regime where the fluid is sucked by the mixture layer. The final model presented in [29] does not account for fluid exchange since they consider $\mathcal{V}_f = 0$. However, in section 4.2 of their paper, the authors discuss the need of an additional closure for this term since they do not consider dilatancy. In our model this closure is indeed given by the dilatancy law that allows to obtain the explicit expression of the fluid transfer rate \mathcal{V}_f .

Their conditions (A.22) have also an important consequence on the pressure of each phase. The layer above contributes with the quantity $(1 - \varphi)(\sigma_f N_X^i) N_X^i$ to the normal stress of the fluid phase in the mixture, but also with $\varphi(\sigma_f N_X^i) N_X^i$ to the normal stress of the solid phase. Namely, the pressures at the interface are given by (see equation 79 in [29]), $p_{s|b+h_m} = \frac{\rho_f}{\rho_s} \varphi p_{f|b+h_m}$, $p_{f_m|b+h_m} = (1 - \varphi) p_{f|b+h_m}$. These values affect the basal solid pressure and thus the Coulomb frictional stress. In [29], if we neglect the curvature effect, the solid pressure at the bottom reads⁴

$$p_{s|b}^{\text{Luca}} = \varphi g \cos \theta \rho_s (h_m + \frac{\rho_f}{\rho_s} h_f) = \varphi g \cos \theta (\rho_s h_m + \rho_f h_f) = \varphi g \cos \theta (\rho_s - \rho_f) h_m + \varphi g \cos \theta \rho_f (h_m + h_f)$$

This expression differs from ours since the authors add to the solid pressure the pressure applied by the fluid layer above while we consider that the separation of the fluid and solid stress tensors induces that the pressure from the upper fluid layer is only supported by the fluid phase.

On the contrary, in our model, we assume that the solid normal stress does not receive any contribution from the liquid layer above (see equations (A.6)). The weight of the upper fluid layer is thus supported by the fluid in the mixture, by assuming that the normal stress is continuous at the interface. The solid phase pressure is of course affected by the pressure of the fluid, but it appears in the buoyancy force given by the term $-\varphi \rho_f g \cos \theta h_m$, that is involved in the resulting solid pressure at the bottom

$$p_{s|b} = \varphi (\rho_s - \rho_f) g \cos \theta h_m - (p_{f_m}^e)_{|b}$$

⁴see equation 82 in that paper or the one dimensional model stated in section 5 of [29]

(see remark 1 below).

Let us now comment on the depth-averaged model for submarine avalanches presented in [54] where dilatancy and mass exchange are taken into account. Three different velocities are considered but the sediment layer is treated as a mixture with velocity V_m . The total momentum conservation is considered as in (A.9) and the friction at the interface reads

$$\begin{aligned} \rho_f \mathcal{V}_f(\mathbf{u}_f - \mathbf{u}) &= (\sigma_f - (\sigma_s + \sigma_{f_m}))N_X^i, \\ (\sigma_f N_X^i)_{\text{tg}} &= (\sigma_{f_m} N_X^i)_{\text{tg}} = C(\mathbf{u}_f - \mathbf{V}_m) = F_d^{\text{Sun}}. \end{aligned} \quad (\text{A.24})$$

where C is a coefficient depending on the permeability⁵. We combine these conditions to write the tangential components of these expressions,

$$\begin{aligned} (\sigma_s N_X^i)_{\text{tg}} &= -E_f, \\ (\sigma_{f_m} N_X^i)_{\text{tg}} &= F_d^{\text{Sun}}, \\ (\sigma_f N_X^i)_{\text{tg}} &= F_d^{\text{Sun}}. \end{aligned} \quad (\text{A.25})$$

Notice that since the sediment layer is considered as a whole, the total stress $\sigma_s + \sigma_{f_m}$ must be considered as the stress in this mixture layer. Hence an equivalence with our proposal in (A.12), gives $\lambda_d^{\text{Sun}} = 0$ and $\lambda_f^{\text{Sun}} = 1$. The first one tells that the solid phase does not experience any friction with the upper-fluid layer. The second one would be equivalent to the proposal in [29], written in (A.23), carrying the same non-dissipative term in the energy balance. Although it is not clearly exposed in [54], the authors consider the continuity of the fluid pressure at the interface, so the solid pressure at the bottom is correctly calculated (see equations B18-B19 in [54]). Nevertheless it is wrongly written in equation (46) of [54] where they present the final model.

Finally, in the debris flow model proposed in [34], these effects are neglected, even for the over-saturated case, and no mass exchange nor friction are considered at the interface.

Remark 1 (Meaning of the solid stress) *In several works in the literature dealing with two-phase flows, as for example in [4, 34, 54], the total solid stress tensor is defined as⁶*

$$\sigma_s^T = \sigma_s - \varphi p_{f_m} \text{Id},$$

where σ_s is called the effective solid stress. The second term holds the effect of the pore pressure exerted on the granular phase and it gives the buoyancy term in the Jackson equations. To quote [4],

The effective granular stress σ_s is the portion of the solid phase stress resulting from granular contact forces and from microscopic viscous stresses on grains from the fluid medium; it excludes the pressurization of the grains due to the pressure of the pore fluid.

Thus, when viscous effects are neglected, the stress tensor σ_s only contains the interaction effects between grains themselves without any influence of the fluid pressure. Therefore it is natural to assume that the solid phase pressure does not receive any contribution of the fluid layer above since it is taken by the pore pressure and the effect of the pore fluid is already present in the buoyancy force.

⁵This term is never explicitly stated in the paper, since it is neglected arguing that this friction effect is not important for the performed applications

⁶In [34] it is said that this notation was originally introduced in [13]

A.4.3 Inter-phase friction

The inter-phase drag force in the mixture is already present in the 3D Jackson system. Besides the pure friction effect between phases –that for example disappear when only one velocity is considered for the mixture, as in [23, 54] or for our models (A2), (B2), (C2)– this term is directly related to the dilatancy through the pore fluid pressure $p_{f_m}^e$, therefore appearing in the model if dilatancy is considered (see section 2.4).

In our 3D starting model this term, taken from [43], is given by

$$\beta(\mathbf{v} - \mathbf{u}), \quad \text{with} \quad \beta = (1 - \varphi)^2 \frac{\eta_f}{k} \quad \text{and} \quad k = \frac{(1 - \varphi)^3 d^2}{150\varphi^2},$$

k being the permeability, leading to the coefficient (see equation (2.17))

$$\beta = \frac{150\varphi^2}{(1 - \varphi)d^2} \eta_f.$$

Notice that in the depth-averaged model presented in section 2.3, this term is kept with the downslope velocities, $\beta(v - u)$, and the vertical component appears in the excess pore pressure. We present here different proposed values of the coefficient β [29, 34, 54, 4].

In the model proposed in [29], β is assumed to be constant. We have seen however here how much its value that depend on the grain diameter may change the flow behavior. For the submarine avalanches model in [54], the expression of [43] is adopted for the 3D system, as in our case. Nevertheless, since only one velocity is considered in the mixture, the force $\beta(v - u)$ does not appear in the final depth-averaged model.

In their debris flows model [34] used

$$\beta^{\text{Meng}} = (1 - \varphi)^2 \frac{\eta_f}{k^{\text{Meng}}} \quad \text{and} \quad k^{\text{Meng}} = \frac{(1 - \varphi)^3 d^2}{180\varphi^2}.$$

The only difference with our model is the coefficient 180 instead of 150. In fact, this value can be deduced from the 3D model proposed in [4]. In this paper, the inter-phase friction coefficient reads (see equation 2.17 in [4])

$$\beta(\hat{F}) = \frac{18\varphi(1 - \varphi)}{d^2} \eta_f \hat{F},$$

where \hat{F} is a function depending on the volume fraction and the Reynolds number. This function is defined as follows for $0.1 < \varphi < 0.6$ and for low Reynolds number,

$$\hat{F} = \frac{10\varphi}{(1 - \varphi)^2} + (1 - \varphi)^2 \left(1 + \frac{3}{2}\sqrt{\varphi} \right).$$

Equivalently, we can also write the corresponding permeability for the model in [4] as

$$k(\hat{F}) = \frac{(1 - \varphi)d^2}{18\varphi\hat{F}}, \quad \text{for} \quad \beta(\hat{F}) = (1 - \varphi)^2 \frac{\eta_f}{k(\hat{F})}$$

The second term of \hat{F} that we denote $\hat{F}_2 = (1 - \varphi)^2 (1 + \frac{3}{2}\sqrt{\varphi})$ is small compared to the first one $\hat{F}_1 = \frac{10\varphi}{(1 - \varphi)^2}$ for high values of φ (see inset figure in figure 24a), hence a good approximation would be

$$\hat{F} \simeq \hat{F}_1 = \frac{10\varphi}{(1 - \varphi)^2}, \quad \text{that leads to} \quad \beta(\hat{F}) \simeq \beta(\hat{F}_1) = \frac{180\varphi^2}{(1 - \varphi)d^2} \eta_f.$$

This coefficient thus coincides with the one proposed in [34], that is, $\beta^{\text{Meng}} = \beta(\hat{F}_1)$ and $k^{\text{Meng}} = k(\hat{F}_1)$. In figure 24a we show the values of these different coefficients that are pretty close. As observed in our numerical simulations in section 5.3.1 the models are very sensitive to the permeability. The values of the permeability in the models discussed here do not differ too much except for small volume fraction as shown in figure 24b. In contrast, the values proposed by Iverson and George in [23] are at least two orders of magnitude bigger (figure 6).

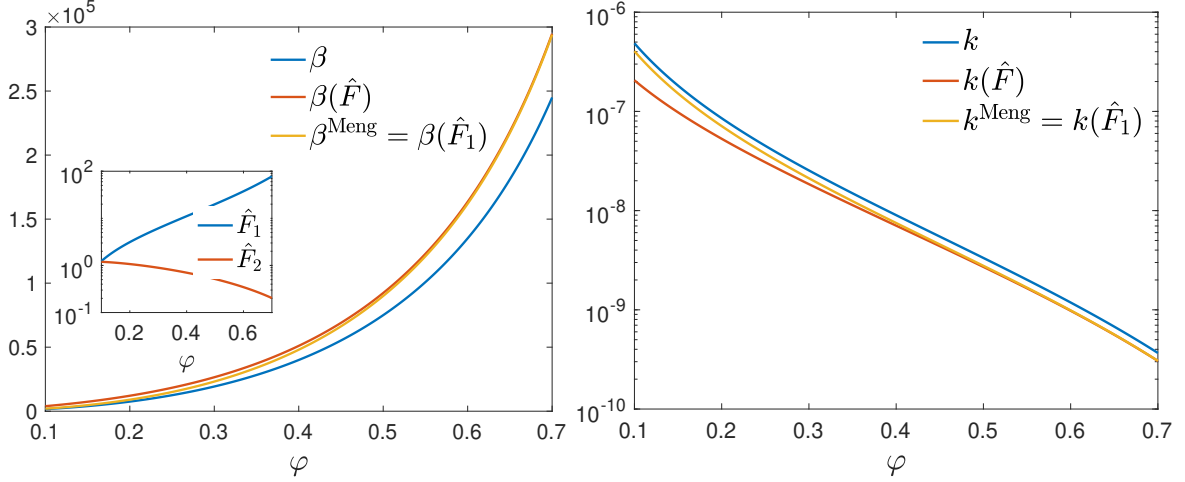


Figure 24: Illustration of the inter-phase drag friction coefficients considered here and in [4, 34], as a function of the solid volume fraction φ and for $d = 10^{-3}\text{m}$ and $\eta_f = 10^{-3}\text{Pa s}$. Left: Friction coefficients β , $\beta(\hat{F})$ and β^{Meng} . Inset figure: Functions $\hat{F}_1 = \frac{10\varphi}{(1-\varphi)^2}$ and $\hat{F}_2 = (1-\varphi)^2 (1 + \frac{3}{2}\sqrt{\varphi})$. Right: Permeability for the three models.

More complex expression for β can be found in the recent papers [38, 37] where a 3D model for immersed granular avalanches with dilatancy is proposed. A quadratic friction is considered here, namely

$$\beta^{\text{Mont.}} = (1-\varphi)^2 \frac{\eta_f}{k^{\text{Mont.}}} \quad \text{with} \quad k^{\text{Mont.}} = \frac{(1-\varphi)^2 d^2}{\alpha_E \varphi^2} + \frac{(1-\varphi)^3 d \eta_f}{\beta_E \rho_f |\mathbf{v} - \mathbf{u}|},$$

where the permeability is originally proposed in [16]. The calibration parameters α_E varies from 780 to 1500 or more and β_E from 1.8 to 3.6 or more. In [37] the authors show the influence of the permeability in their model through numerical results. Notice that if we neglect the second term in the permeability $k^{\text{Mont.}}$ that provides the quadratic friction, we find

$$\beta^{\text{Mont.}} \simeq \frac{\alpha_E \varphi^2}{d^2} \eta_f$$

Compared to our coefficient $\beta = \frac{150\varphi^2}{(1-\varphi)d^2} \eta_f$, a factor $(1-\varphi)$ is missing, but these expression can roughly coincide for values of α_E of the order of $150/(1-\varphi)$, even though the φ -dependency may be important.

A.5 Energy balance

The energy balance of the system (2.12)-(2.22) is slightly modified from the original one presented in [7], related to the boundary condition modification and reads

$$\begin{aligned}
& \partial_t \left(\rho_s \varphi h_m \frac{|v|^2}{2} + \rho_f (1 - \varphi) h_m \frac{|u|^2}{2} + \rho_f h_f \frac{|u_f|^2}{2} \right. \\
& \quad + g \cos \theta \left(\rho_s \varphi h_m + \rho_f ((1 - \varphi) h_m + h_f) \right) (b + \tilde{b}) \\
& \quad \left. + (\rho_s - \rho_f) g \cos \theta \varphi \frac{h_m^2}{2} + \rho_f g \cos \theta \frac{(h_m + h_f)^2}{2} \right) \\
& + \nabla \cdot \left(\rho_s \varphi h_m \frac{|v|^2}{2} v + \rho_f (1 - \varphi) h_m \frac{|u|^2}{2} u + \rho_f h_f \frac{|u_f|^2}{2} u_f \right. \\
& \quad + g \cos \theta \left(\rho_s \varphi h_m v + \rho_f ((1 - \varphi) h_m u + h_f u_f) \right) (b + \tilde{b} + h_m) \\
& \quad \left. + \rho_f g \cos \theta \left(\varphi h_m v + (1 - \varphi) h_m u + h_f u_f \right) h_f + (1 - \varphi) h_m \overline{p_{f_m}^e} (u - v) \right) \\
& \leq \frac{1}{2} (\rho_s - \rho_f) \varphi g \cos \theta h_m^2 \Phi + R_e - \frac{\delta_f}{2} |u_f - u|^2 \rho_f |\mathcal{V}_f| \\
& \quad - \beta h_m |u - v|^2 - |v| \mu \left(\varphi (\rho_s - \rho_f) g \cos \theta h_m - (p_{f_m}^e)_{|b} \right) - k_f |u_f - V_m|^2 - \frac{5}{2} \frac{\eta_e (1 - \varphi)}{h_m} |u|^2,
\end{aligned} \tag{A.26}$$

with

$$R_e = h_m \overline{p_{f_m}^e} \nabla \cdot \left((1 - \varphi) (u - v) \right) - (1 - \varphi) (p_{f_m}^e)_{|b} (u - v) \cdot \nabla b.$$

A.6 Derivation of a pressure evolution equation

In section 2.3.2 we introduced a new approach to solve the basal solid pressure for our depth-averaged model. The proposed equation is deduced from a 3D evolution equation for the solid pressure that we derive from [4]. We give here the details of this approach. In this work the solid stress tensor $\sigma_s = -p_s \text{Id} + \sigma'_s$ is solved through an evolution equation taking into account plastic effects (see equation 2.25 in [4]). This equation reads⁷

$$\partial_t \sigma_s + \mathbf{v} \cdot \nabla \sigma_s = 2G D_{e0} + B \text{tr}(D_e) \text{Id} + W_s \sigma_s - \sigma_s W_s$$

where G and B are the solid shear and bulk modulus respectively, $B = \frac{E}{3(1-2\nu)}$, $G = \frac{E}{2(1+\nu)}$ with E the Young's modulus and ν the Poisson's ratio. The solid strain rate $D(\mathbf{v}) = \frac{1}{2}(\nabla \mathbf{v} + \nabla \mathbf{v}^t)$ is decomposed into an elastic strain rate D_e and a plastic contribution D_p , $D(\mathbf{v}) = D_e + D_p$ with D_p given by

$$D_p = \frac{\dot{\gamma}}{\sqrt{2}} \frac{\sigma_{s0}}{\|\sigma_{s0}\|} + \frac{1}{3} (\dot{\gamma} \tan \psi + \dot{\xi}_1 + \dot{\xi}_2) \text{Id}$$

where σ_{s0} is the initial stress and $\dot{\xi}_1, \dot{\xi}_2$ are the rate of plastic expansion and compaction, respectively. D_{e0} represents the initial elastic strain rate. Finally, W_s is the rotational rate tensor (skew part of the velocity gradient), that is, $W_s = \frac{1}{2}(\nabla \mathbf{v} - \nabla \mathbf{v}^t)$.

The solid pressure is defined as $p_s = -\frac{1}{3} \text{tr}(\sigma_s)$, so a transport equation for it may be deduced by

⁷For simplicity we will use the same gradient notation for 3D and 2D functions. It must be understood as $\nabla \mathbf{f} = (\partial_x \mathbf{f}, \partial_y \mathbf{f}, \partial_x \mathbf{f})$, for any function $\mathbf{f}(t, x, y, z)$, or as $\nabla f = (\partial_x f, \partial_y f)$ for any function $f(t, x, y)$.

taking the trace of the previous equation for σ_s . We neglect purely plastic effects, $\dot{\xi}_1 = \dot{\xi}_2 = 0$, and we assume a symmetric velocity gradient (symmetric solid plastic flow), $W_s = 0$. The equation for the solid pressure then reads

$$\partial_t p_s + \mathbf{v} \cdot \nabla p_s = -\frac{1}{3}(2G \operatorname{tr}(D_{e0}) + 3B \operatorname{tr}(D_e)).$$

Assuming that the solid phase begins in a stress-free state, $\sigma_{s0} = 0$, the plastic stress yields

$$D_p = \frac{1}{3}\dot{\gamma} \tan \psi \operatorname{Id}.$$

Then the trace of the elastic stress $D_e = D(\mathbf{v}) - D_p$ is

$$\operatorname{tr}(D_e) = \nabla \cdot \mathbf{v} - \dot{\gamma} \tan \psi.$$

If we assume that at the initial state the solid phase satisfies $\operatorname{tr}(D_{e0}) = 0$, what just means that the relation $\nabla \cdot \mathbf{v} = \dot{\gamma} \tan \psi$ is satisfied at the initial time, the pressure equation becomes

$$\partial_t p_s + \mathbf{v} \cdot \nabla p_s = -B(\nabla \cdot \mathbf{v} - \dot{\gamma} \tan \psi). \quad (\text{A.27})$$

The equation (A.27) replaces the closure $\Phi = \dot{\gamma} \tan \psi$ in [7] in the starting two-phase 3D model given by the Jackson's equations. In order to obtain the depth-averaged model we must apply the shallow approximation and the depth-averaging process. Let us see in the next lines how to obtain (2.26) from (A.27). Firstly we remind that the 3D velocity is denoted by $\mathbf{v}(t, x, y, z) = (v(t, x, y), v^z(t, x, y, z))$.

We first use $\nabla \cdot \mathbf{v} = \Phi$ to write $\partial_z v^z = \Phi - \nabla \cdot v$, then (A.27) yields

$$\partial_t p_s + v \cdot \nabla p_s + \partial_z(v^z p_s) = p_s(\Phi - \nabla \cdot v) - B(\Phi - \dot{\gamma} \tan \psi).$$

As in [7], we use the approximations

$$v \sim \bar{v} + O(\epsilon^2), \quad \varphi \sim \bar{\varphi} + O(\epsilon^2), \quad \Phi \sim \bar{\Phi} + O(\epsilon^2), \quad \dot{\gamma} \sim \bar{\dot{\gamma}} + O(\epsilon^2), \quad \tan \psi \sim \tan \bar{\psi} + O(\epsilon^2),$$

to write

$$\partial_t p_s + \bar{v} \cdot \nabla p_s + \partial_z(v^z p_s) = p_s(\bar{\Phi} - \nabla \cdot \bar{v}) - B(\bar{\Phi} - \bar{\dot{\gamma}} \tan \bar{\psi}) + O(\epsilon^2). \quad (\text{A.28})$$

We integrate this equation in $[b, b + h_m]$. Using

$$p_s = \bar{\varphi}(\rho_s - \rho_f)g \cos \theta (b + h_m - z) - p_{f_m}^e$$

we write

$$h_m \bar{p}_s \equiv \int_b^{b+h_m} p_s dz = \frac{h_m^2}{2} \bar{\varphi}(\rho_s - \rho_f)g \cos \theta - h_m \overline{p_{f_m}^e}$$

with $\overline{p_{f_m}^e} = \frac{1}{h_m} \int_b^{b+h_m} p_{f_m}^e dz$ and then $\bar{p}_s = \frac{h_m}{2} \bar{\varphi}(\rho_s - \rho_f)g \cos \theta - \overline{p_{f_m}^e}$. The integral of the left hand side of (A.28), using the Leibniz rule gives

$$\begin{aligned} & \int_b^{b+h_m} (\partial_t p_s + \bar{v} \cdot \nabla p_s) dz + (v^z p_s)|_{b+h_m} - (v^z p_s)|_b \\ &= \partial_t (h_m \bar{p}_s) + \bar{v} \cdot \nabla (h_m \bar{p}_s) - p_s(b + h_m)(\partial_t(b + h_m) + \bar{v} \cdot \nabla(b + h_m) - v^z(b + h_m)) \\ &+ p_s(b)(\partial_t b + \bar{v} \cdot \nabla b - v^z(b)) \\ &= \partial_t (h_m \bar{p}_s) + \bar{v} \cdot \nabla (h_m \bar{p}_s). \end{aligned}$$

In the last equality we used the definition of p_s and the boundary condition at the bottom that give $p_s(b + h_m) = 0$, and $v^z(b) = v_{|b} \cdot \nabla b \sim \bar{v} \cdot \nabla b$. From the mass equations we have

$$\partial_t h_m + \nabla \cdot (h_m \bar{v}) = h_m \bar{\Phi},$$

hence

$$\begin{aligned} \partial_t (h_m \bar{p}_s) + \bar{v} \cdot \nabla (h_m \bar{p}_s) &= h_m (\partial_t \bar{p}_s + \bar{v} \cdot \nabla \bar{p}_s) + \bar{p}_s (\partial_t h_m + \bar{v} \cdot \nabla h_m) \\ &= h_m (\partial_t \bar{p}_s + \bar{v} \cdot \nabla \bar{p}_s) + \bar{p}_s (h_m \bar{\Phi} - h_m \nabla \cdot \bar{v}). \end{aligned}$$

According to the asymptotic approximation, the second term on the right-hand side of the equation (A.28) does not depend on z up to ϵ^2 , thus we obtain

$$h_m (\partial_t \bar{p}_s + \bar{v} \cdot \nabla \bar{p}_s) + \bar{p}_s h_m (\bar{\Phi} - \nabla \cdot \bar{v}) = h_m \bar{p}_s (\bar{\Phi} - \nabla \cdot \bar{v}) - B h_m (\bar{\Phi} - \bar{\gamma} \tan \bar{\psi}).$$

Then the depth-averaged equation for the averaged solid pressure writes

$$\partial_t \bar{p}_s + \bar{v} \cdot \nabla \bar{p}_s = -B (\bar{\Phi} - \bar{\gamma} \tan \bar{\psi}). \quad (\text{A.29})$$

We can write the basal solid pressure in terms of the averaged \bar{p}_s as

$$p_{s|b} = h_m \bar{\varphi} (\rho_s - \rho_f) g \cos \theta - p_{f_m|b}^e = 2(\bar{p}_s + \overline{p_{f_m}^e}) - p_{f_m|b}^e.$$

This adds a new unknown $p_{f_m|b}^e$, but we can use the approximations found in [7] to write $p_{f_m|b}^e = \frac{3}{2} \overline{p_{f_m}^e}$ and then, using again $\overline{p_{f_m}^e} = -\bar{p}_s + \frac{h_m}{2} \bar{\varphi} (\rho_s - \rho_f) g \cos \theta$ we write

$$p_{s|b} = 2\bar{p}_s - \frac{1}{2} \overline{p_{f_m}^e} = \frac{3}{2} \bar{p}_s - \frac{h_m}{4} \bar{\varphi} (\rho_s - \rho_f) g \cos \theta,$$

hence we find the relation between the basal and the averaged solid pressure,

$$\bar{p}_s = \frac{2}{3} p_{s|b} + \frac{h_m}{6} \bar{\varphi} (\rho_s - \rho_f) g \cos \theta.$$

We embed this relation in (A.29) to write the evolution equation for the basal solid pressure

$$\frac{2}{3} (\partial_t p_{s|b} + \bar{v} \cdot \nabla p_{s|b}) + \frac{1}{6} (\rho_s - \rho_f) g \cos \theta (\partial_t (h_m \bar{\varphi}) + \bar{v} \cdot \nabla (h_m \bar{\varphi})) = -B (\bar{\Phi} - \bar{\gamma} \tan \bar{\psi}).$$

Therefore using (2.12a),

$$\partial_t p_{s|b} + \bar{v} \cdot \nabla p_{s|b} = \frac{1}{4} (\rho_s - \rho_f) g \cos \theta \bar{\varphi} h_m \nabla \cdot \bar{v} - \frac{3}{2} B (\bar{\Phi} - \bar{\gamma} \tan \bar{\psi}). \quad (\text{A.30})$$

The averaged excess pore pressure appearing in the system is recovered through

$$\overline{p_{f_m}^e} = \frac{2}{3} p_{f_m|b}^e = \frac{2}{3} (-p_{s|b} + h_m \bar{\varphi} (\rho_s - \rho_f) g \cos \theta).$$

Later in section C.2 we develop a comparison with the equation proposed in [23] to solve the basal pressure.

Remark 2 *We would like to point out that equation (A.27) is obtained by neglecting the rates of plastic expansion and compaction $\dot{\xi}_1, \dot{\xi}_2$. As said in [4] in most granular materials, the elastic deformation are extremely small compared to plastic deformation, the latter being even more important when the solid phase is flowing. Then our approximation (A.27) and the derived depth-averaged equation (2.26) are only valid when the elastic contribution is small (high solid bulk modulus B).*

Remark 3 Other alternatives can be found in the literature where a pressure evolution equation taking into account dilatancy, is used to close the two-phase 3D system. Let us mention the papers [27, 38, 37] where 3D models are proposed to solve immersed granular flows. In the work [27] the following equation for the pressure is considered:

$$\partial_t p_s + \mathbf{v} \cdot \nabla p_s = 2K\varphi\dot{\gamma}(p_s^{\text{eq}} - p_s) - K_2\varphi\nabla \cdot \mathbf{v} - K_3 p_s \mathcal{H}(\varphi_0 - \varphi) \quad (\text{A.31})$$

where the constants are: K (from the dilatancy law in [43], $\tan \psi = K(\varphi - \varphi^{\text{eq}})$), $K_3 = 100s^{-1}$, $\varphi_0 = 0.55$ (random loose packing), $\varphi_c = 0.576$,

$$K_2 = \begin{cases} a_e E & \varphi \geq \varphi_c \\ a_e E \frac{\varphi - \varphi_0}{\varphi_c - \varphi_0} & \varphi_0 \geq \varphi < \varphi_c \\ 0 & \varphi < \varphi_0 \end{cases}$$

with $a_e = 0.1$, and E is the Young modulus (10^6 Pa). The Heaviside function $\mathcal{H}(x)$ is 0 for negative values and 1 for positive or zero values.

As it was exposed in section 2.4 of [7], for a linear approximation we can establish the following relation

$$K(\varphi - \varphi^{\text{eq}}) \sim K_p(p_s^{\text{eq}} - p_s),$$

and then the equation becomes

$$\partial_t p_s + \mathbf{v} \cdot \nabla p_s = -K_2\varphi \left(\nabla \cdot \mathbf{v} - \frac{2K}{K_2 K_p} \dot{\gamma}(\varphi - \varphi^{\text{eq}}) \right) - K_3 p_s \mathcal{H}(\varphi_0 - \varphi). \quad (\text{A.32})$$

In the case $\varphi > \varphi_0$, the Heaviside function vanishes and this equation has the same form as the simplified equation from [4], considered here in (A.27).

In [38] a simpler equation has been considered by taking

$$\partial_t p_s + \mathbf{v} \cdot \nabla p_s = K\varphi\dot{\gamma}(p_s^{\text{eq}} - p_s), \quad (\text{A.33})$$

so only the first term in (A.31) is kept. Using the same approach, it can be written as

$$\partial_t p_s + \mathbf{v} \cdot \nabla p_s = -\frac{K}{K_p} \varphi \dot{\gamma}(\varphi - \varphi^{\text{eq}}). \quad (\text{A.34})$$

The main difference is that this equation does not have the divergence term.

B Equivalence of notations in our model and in Iverson and George [23, 18] and Meng and Wang [35]

In order to easily track the models' comparison we briefly summarize the equivalence between our notation and those used in the Iverson-George model (table 4), and in the Meng-Wang model (table 5), respectively. Note that we only display the variables that have a different notations in the models.

Variable	Here	Iverson-George [23]
Solid volume fraction	φ	m
Depth-averaged velocity	v	(u, v)
Basal fluid pressure	$(p_{f_m}) _b$	p_b
Excess pore fluid pressure	$p_{f_m}^e$	p_e
Effective fluid viscosity	η_e	μ
Internal friction angle	δ	ϕ
Dilatancy angle	ψ_{IG}	ψ
Static volume fraction	φ_c	m_{crit}
Critical-state compacity	φ_{IG}^{eq}	m_{eq}
Viscous dimensionless number	J	I_v
Stokes number	St	S

Table 4: Equivalence between our notations and those used in the Iverson-George model [23, 18]. Note that in [18] the “bar” notation is removed in the depth-averaged velocity.

Variable	Here	Meng & Wang [35]
Solid density	$\varphi\rho_s$	ρ_s
Fluid density	$(1 - \varphi)\rho_f$	ρ_f
Material density ($j = s, f$)	ρ_j	$\tilde{\rho}_j$
Dynamic fluid viscosity	η_f	μ_f
Solid volume fraction	φ	ν_s
Fluid volume fraction	$1 - \varphi$	ν_f
Solid velocity (3d)	$v = (v^x, v^z)$	$\mathbf{v}_s = (u_s, v_s, w_s)$
Fluid velocity (3d)	$u = (u^x, u^z)$	$\mathbf{v}_f = (u_f, v_f, w_f)$
Solid velocity (averaged)	v	u_s
Fluid velocity (averaged)	u	u_f
Solid stress tensor	$\varphi\sigma_s$	$\boldsymbol{\sigma}_e$
Fluid stress tensor	$(1 - \varphi)\sigma_{f_m}$	$\boldsymbol{\sigma}_f$
Shear fluid stress tensor	σ'_{f_m}	$\boldsymbol{\tau}_f$
Mixture velocity	V_m	\mathbf{v}_m
Normal vector at the bottom	n	$\mathbf{n}^{(b)}$
Normal vector at the virtual surface	–	$\mathbf{n}^{(s)}$
Normal vector at the free surface	\tilde{N}_X	–
Normal vector at the interface	\tilde{N}_X	–
Excess pore fluid pressure (averaged)	$p_{f_m}^e$	p_e
Solid pressure (averaged)	p_s	$\sigma_0 = \sigma_{e(zz)}$
Mass exchange term (flux of the granular mass)	$\tilde{\mathcal{J}}$	\mathcal{J}
Mass exchange distribution coeff.	λ_f	λ
Solid friction coef.	–	α_s
Fluid friction coef.	$\frac{5}{2} \frac{\eta_e}{h_m}$	α_f
Coulomb friction coef.	μ	μ_s

Table 5: Equivalence between our notations and those used in the Meng-Wang model [35]

C Comparison with the Iverson-George model: further details

C.1 Details of calculations

We claimed that the Iverson-George model is equivalent to our oversimplified mixture model (C2) (equations (3.14)) which has been deduced from our two-layer mixture model (B2) (equations (3.1)) under the hypothesis $\Delta_H \ll 1$. In this section we detail the comparison between (3.1) and the Iverson-George model (3.16) as well as the hypotheses making it possible to recover the Iverson-George model from our model.

In view of the conservation laws (3.16b) and (3.1a), we see that the virtual thickness h in the Iverson-George model corresponds to our H . From (3.1a) and (3.3) (or equivalently (2.23)) we obtain the continuity equation for the virtual thickness H since

$$\partial_t H + \nabla \cdot (Hv) = \frac{\rho - \rho_f}{\rho} H\Phi.$$

This equation coincides with equation (3.16a) in the Iverson-George model when

$$D = h\Phi,$$

as claimed in (3.19). Our equation for the upper fluid layer thickness (3.1b) obviously does not appear in the Iverson-George model.

Then we have to compare the momentum equations (3.9d) and (3.16c). Instead of the equation (3.16c) on hv , let us write it on ρhv

$$\begin{aligned} \partial_t(\rho hv) + \nabla \cdot (\rho hv \otimes v) + \kappa g \cos \theta \nabla \left(\frac{1}{2} \rho h^2 \right) + \kappa g \cos \theta \frac{h^2}{2} \nabla \rho + h(1 - \kappa) \nabla p_b \\ = -\rho h g \cos \theta \nabla b - \rho g h \sin \theta \mathbf{e}_x - \mu_{\text{IG}} \operatorname{sgn}(v) (\rho g \cos \theta h - p_b) - \frac{2\eta_e}{h} (1 - \varphi) v, \end{aligned} \quad (\text{C.1})$$

where we replaced τ_s and τ_f using (3.17a)-(3.17b). We rewrite (3.9d) here using (3.11)-(3.12) to make the comparison easier:

$$\begin{aligned} \partial_t(\rho H v) + \nabla \cdot (\rho H v \otimes v) + g \cos \theta \nabla \left(\frac{1}{2} \rho \left(H^2 + \frac{\rho - \rho_f}{\rho_f} \Delta_H^2 \right) \right) \\ = -\rho H g \cos \theta \nabla b - \rho H g \sin \theta \mathbf{e}_x - \mu \operatorname{sgn}(v) (\rho g \cos \theta H - (p_{f_m})|_b) - \frac{5\eta_e(1 - \varphi)}{2H - \Delta_H} v. \end{aligned} \quad (\text{C.2})$$

Firstly, we notice that the term $\kappa g \cos \theta \frac{h^2}{2} \nabla \rho$ in (C.1) does not appear in (C.2). This term can be neglected in the model as the authors argue in [18] under the assumption of small gradient in ρ . Secondly, in order to make these momentum equations look the same, we have to set $\kappa = 1$, that is, we assume isotropy of normal stresses. Notice that the convective terms are the same in the two models with $h = H$ but it is not the case for the pressure terms and the basal shear for the fluid. Under the condition

$$\Delta_H = H - h_m \ll H \quad (\text{C.3})$$

the pressure term $g \cos \theta \nabla(\rho h^2/2)$ in (C.1) identifies with the equivalent pressure term in (C.2) and the shear term becomes the same, $\frac{2\eta_e(1-\varphi)}{H}$, except for the coefficient coming from the approximation of the strain shear rate, 2 for the Iverson-George model and 5/2 for our model.

We now focus on the friction term at the bottom which involves the basal pressure and the friction coefficient $\mu = (\mu^{\text{eq}} + \tan \psi)_+$ for us and $\mu_{\text{IG}} = \tan(\delta + \psi_{\text{IG}})$ in the Iverson-George model. Assuming a linearization of the tangent, we write

$$\mu_{\text{IG}} \simeq \tan \delta + \tan \psi_{\text{IG}}.$$

As we said in section 3.4.2, the main difference is that the friction coefficient in the critical state $\mu_c = \tan \delta$ is thus constant while it depends on the inertial and viscous numbers in our model $\mu^{\text{eq}}(\mathcal{J}_\mu)$ (see equations (2.7) and (2.11)). We would like to make a more detailed analysis of the rheology: for us it is given by (2.9), (2.7) and for Iverson-George by (3.17f). An explicit comparison has been summarized in table 3. The form of the dimensionless parameter N in (3.17f) is obtained as a generalization of the viscous number $J = \frac{\eta_f \dot{\gamma}}{\sigma_e}$ taking into account a collision term $\rho_s d^2 \dot{\gamma}^2$, that helps to avoid the division by zero in case of vanishing pressure σ_e , that is

$$N = \frac{\eta_e \dot{\gamma}}{\sigma_e + \rho_s d^2 \dot{\gamma}^2}.$$

Notice that in this definition the fluid viscosity η_f in J has been replaced by the effective shear viscosity η_e , even if later in the paper [23] it is assumed as a constant, considering the pore fluid as a Newtonian viscous material. Dividing by the pressure σ_e we find the inertial number I^2 in the denominator of N as shown in (3.17f). In our model we do not consider the collision term but a combined inertial-viscous number \mathcal{J}_φ . Notice that the approximation of the shear rate $\dot{\gamma}$ also differs, given by (2.10) and (3.17e), respectively. The coefficient 2 in (3.17e) is related to a particular shape of the velocity profile. Indeed, the detailed study of [10] shows that a coefficient 3 corresponds to the viscous regime (used for example in [43]) and a more general coefficient 5/2 is compatible with the free fall or inertial regimes (used for example in [8]), which is also the choice made here (2.10). Beside the coefficient, in our approximation it is the thickness of the mixture which is involved in the shear rate and not the virtual thickness H as discussed in Section 3.3.

The basal pressure in the Coulomb law is represented by σ_e in the Iverson-George model (3.17b) and by $p_{s|b}$ for us (3.11)

$$\sigma_e = \rho g \cos \theta h - p_b, \quad p_{s|b} = \rho g \cos \theta H - (p_{f_m})|_b.$$

If we assume $h = H$, the hydrostatic contribution is the same in the two models. In the Iverson-George model the basal excess fluid pressure p_b is the solution of equation (3.16d). If we assume $\alpha \rightarrow 0$, this equation reduces to

$$D = 2|v| \tan \psi_{\text{IG}}, \tag{C.4}$$

and the pressure p_b , obtained in the Iverson-George model by inverting (3.17d), is

$$p_b = \rho_f g \cos \theta h - \frac{\eta_e}{2k_{\text{IG}}} h D. \tag{C.5}$$

By considering (3.19) we can write

$$p_b = \rho_f g \cos \theta h - \frac{\eta_e}{2k_{\text{IG}}} h^2 \Phi. \tag{C.6}$$

In our model the basal excess fluid pressure is given in equation (3.12)

$$(p_{f_m})|_b = \rho_f g \cos \theta \left(H + \frac{\rho - \rho_f}{\rho_f} \Delta_H \right) + (p_{f_m}^e)|_b.$$

The hydrostatic part would then coincide under (C.3). Now we have to compare the last term coming from the excess pore pressure, that reads $-\frac{\eta_e}{2k_{\text{IG}}}h^2\Phi$ for the Iverson-George model and $(p_{f_m}^e)_|b$ for our model. According to (3.10a) and to the value of β in (2.17),

$$(p_{f_m}^e)_|b = -\frac{\eta_f}{k} \frac{h_m^2}{2} \Phi = -\frac{\eta_f}{k} \frac{(H - \Delta_H)^2}{2} \Phi, \quad (\text{C.7})$$

and then both definitions are the same under (C.3) for k and k_{IG} denoting both the hydraulic permeability, calculated differently in the two models in (2.17) and (3.17d) respectively, and assuming a constant effective fluid viscosity $\eta_e = \eta_f$.

We conclude that the limit $\alpha \rightarrow 0$ in the Iverson-George model with $\kappa = 1$ and neglecting the term $g \cos \theta \frac{h^2}{2} \nabla \rho$ in (C.1) can be considered as a simplification of our one velocity two-layer (3.1) under the assumption (C.3) and with $h = H$. In these conditions, the Iverson-George model corresponds to our one-layer model one-velocity model (3.14).

C.2 Comparison of the basal pore pressure equation

We compare here the equations for the solid basal pressure proposed in this paper (2.26) and in the Iverson-George model (3.16d). First let us briefly remind how equation (3.16d) is obtained in the Iverson-George model, from a Darcy law and dilatancy relations, following [23]. The same notation as in section A.6 is used here, namely, 3D velocity is denoted by $\mathbf{v}(t, x, y, z) = (v(t, x, y), v^z(t, x, y, z))$ and the same gradient notation is used for both, 3D and 2D functions. Moreover the material derivative is $D_t(\xi) = \partial_t(\xi) + \mathbf{v} \cdot \nabla(\xi)$, for any function ξ . In particular, the 3D dilatancy law is given by

$$\dot{\gamma} \tan \psi_{\text{IG}} = \alpha D_t \sigma_e - \frac{1}{\varphi} D_t \varphi$$

where the first term on the r.h.s. accounts for the elasticity effect. The evolution of the volume fraction, appearing in the last term, is related to the divergence of the solid velocity and the apparent fluid velocity $\mathbf{q} = (1 - \varphi)(\mathbf{u} - \mathbf{v})$ through the relation,

$$\frac{1}{\varphi} D_t \varphi = -\nabla \cdot \mathbf{v} = \nabla \cdot \mathbf{q}.$$

The dilatancy law then reads as in (2.25)

$$\alpha D_t \sigma_e = -\nabla \cdot \mathbf{v} + \dot{\gamma} \tan \psi_{\text{IG}}, \quad (\text{C.8})$$

when $\alpha = 1/B$. The Darcy law is given by

$$\mathbf{q} = -\frac{k_{\text{IG}}}{\eta_e} \nabla p_e.$$

Considering that the mean total normal stress is defined as $\sigma = p_f + \sigma_e$, combining these equations leads to

$$\alpha D_t (p_f - \sigma) = \nabla \cdot \left(\frac{k_{\text{IG}}}{\eta_e} \nabla p_e \right) - \dot{\gamma} \tan \psi_{\text{IG}},$$

In depth-averaging this equation, several hypothesis are considered to finally achieve (3.16d). as summarized in the following lines

- Shallow flow assumption is considered and the equation is approximated at first order in $\epsilon = H/L$,

$$\alpha D_t(p_f - \sigma) = \partial_z \left(\frac{k_{\text{IG}}}{\eta_e} \partial_z p_e \right) - \dot{\gamma} \tan \psi_{\text{IG}}.$$

- $\frac{k_{\text{IG}}}{\eta_e}$ does not depend on z (no material property varies in z). Notice that since $p_f = p_h + p_e$ and $p_h = \rho_f g \cos \theta (h - z)$, we have $\partial_z^2 p_e = \partial_z^2 p_f$. Then

$$\alpha D_t(p_f - \sigma) = \frac{k_{\text{IG}}}{\eta_e} \partial_z^2 p_f - \dot{\gamma} \tan \psi_{\text{IG}}.$$

- A linear profile in z is assumed for the vertical velocity. Using $v^z(z=0) = 0$ and the kinematic condition $v^z(z=h) = \partial_t h + v \cdot \nabla h$, then v^z is approximated by $v^z = \frac{z}{h} \bar{D}_t h$, with $\bar{D}_t h = \partial_t h + v \cdot \nabla h$. As a consequence, $D_t(\xi) \sim \bar{D}_t(\xi) + v \cdot \nabla(\xi) + \frac{z}{h} \bar{D}_t h \partial_z(\xi)$. The equation becomes,

$$\alpha \left(\bar{D}_t(p_f - \sigma) + \frac{z}{h} \bar{D}_t h \partial_z(p_f - \sigma) \right) = \frac{k_{\text{IG}}}{\eta_e} \partial_z^2 p_f - \dot{\gamma} \tan \psi_{\text{IG}}.$$

- Boundary conditions for the pressure: At the free surface, traction free for solid and fluid phases are considered, $p_f|_{z=h} = \sigma_e|_{z=h} = 0$. At the bottom, hydrostatic pore pressure gradient is assumed, $\partial_z p_f|_{z=0} = -\rho_f g \cos \theta$. The depth-averaging of previous equation yields

$$\alpha h \bar{D}_t(\bar{p}_f - \bar{\sigma}) = \frac{k_{\text{IG}}}{\eta_e} (\partial_z p_f|_{z=h} + \rho_f g \cos \theta) - h \bar{\gamma} \tan \bar{\psi}_{\text{IG}},$$

where for clarity in the exposition we used the ‘‘overline’’ notation for the depth-averaged quantities, that is, for any f , $\bar{f} = \frac{1}{h} \int_0^h f dz$. It is assumed that α is constant in z , $v \sim \bar{v}$, $\bar{\gamma} \sim \dot{\gamma}_{\text{IG}} = \frac{2|\bar{v}|}{h}$, $\tan \bar{\psi}_{\text{IG}}$ is defined as in (3.17f) for $\bar{\varphi}$.

- A quadratic profile in z is specified for the pore fluid pressure, $\partial_z^2 p_f = C$ (cst. in z), that thanks to previous boundary condition gives

$$p_f = p_b \left(1 - \frac{z^2}{h^2} \right) - \rho_f g \cos \theta h \left(\frac{z}{h} - \frac{z^2}{h^2} \right).$$

This expression is used to find \bar{p}_f and $\partial_z p_f|_{z=h}$ to be replaced in the pressure equation, leading to

$$\alpha h \bar{D}_t \left(\frac{2}{3} p_b - \frac{1}{6} \rho_f g \cos \theta h - \bar{\sigma} \right) = \frac{k_{\text{IG}}}{\eta_e} \left(\rho_f g \cos \theta - 2 \frac{p_b}{h} + \rho_f g \cos \theta \right) - h \bar{\gamma} \tan \bar{\psi}_{\text{IG}}.$$

- Depth-averaged total normal stress is defined as $\bar{\sigma} = \frac{1}{2} \rho g \cos \theta h$ (half of the basal total normal traction). The equation becomes

$$\alpha h \bar{D}_t \left(\frac{2}{3} p_b - \frac{1}{2} g \cos \theta h \left(\frac{1}{3} \rho_f + \rho \right) \right) = \frac{2k_{\text{IG}}}{\eta_e} \left(\rho_f g \cos \theta - \frac{p_b}{h} \right) - h \bar{\gamma} \tan \bar{\psi}_{\text{IG}},$$

and developing the first term,

$$\frac{2}{3} \alpha h \bar{D}_t p_b - \frac{1}{2} \alpha h g \cos \theta \left(\frac{1}{3} \rho_f \bar{D}_t h + \bar{D}_t(\rho h) \right) = \frac{2k_{\text{IG}}}{\eta_e} \left(\rho_f g \cos \theta - \frac{p_b}{h} \right) - h \bar{\gamma} \tan \bar{\psi}_{\text{IG}}.$$

Mass equations (4.5 and 4.6 in [23]) give respectively $\bar{D}_t(\rho h) = -\rho h \nabla \cdot \bar{v}$ and $\bar{D}_t h = \frac{\rho - \rho_f}{\rho} D - h \nabla \cdot \bar{v}$.

Embedding these expressions in the previous equation, we finally write the pressure equation as

$$\bar{D}_t p_b + \frac{1}{4} g \cos \theta \left((\rho_f + 3\rho) h \nabla \cdot \bar{v} - \rho_f \frac{\rho - \rho_f}{\rho} D \right) = \frac{3}{2\alpha} \left(\frac{2k_{\text{IG}}}{\eta_e h^2} (\rho_f g \cos \theta h - p_b) - \bar{\gamma} \tan \bar{\psi}_{\text{IG}} \right).$$

Using expressions (3.17c) and (3.17d) in the first term on the r.h.s. we find (3.16d),

$$\partial_t p_b + \bar{v} \cdot \nabla p_b = -\frac{1}{4} g \cos \theta \left((\rho_f + 3\rho) h \nabla \cdot \bar{v} - \rho_f \frac{\rho - \rho_f}{\rho} D \right) + \frac{3}{2\alpha} \left(\frac{D}{h} - \bar{\gamma} \tan \bar{\psi} \right). \quad (\text{C.9})$$

To derive the expression of the dilatancy term D in (3.17d), defined as $D = \int_0^h \nabla \cdot \mathbf{v} dz$, one uses again the hypothesis above. Namely, thanks to the dilatancy relations,

$$D = \int_0^h \nabla \cdot \mathbf{v} dz = \int_0^h \nabla \cdot \left(\frac{k_{\text{IG}}}{\eta_e} \nabla p_e \right) dz \sim \int_0^h \frac{k_{\text{IG}}}{\eta_e} \partial_z^2 p_f dz.$$

where we used the shallow approximation, that $\frac{k_{\text{IG}}}{\eta_e}$ does not depend on z and $\partial_z^2 p_e = \partial_z^2 p_f$. Finally, the quadratic profile of p_f gives $\partial_z^2 p_f = \frac{2}{h^2} (\rho_f g \cos \theta h - p_b)$, so

$$D = \frac{2k_{\text{IG}}}{\eta_e h} (\rho_f g \cos \theta h - p_b).$$

Comparison with our proposal (2.26)

Firstly we remark that the 3D equations for the pressure are the same in both models, (2.25) for our model and (C.8) for the Iverson-George model, under $\alpha = 1/B$. However the depth-averaging process is developed differently. We compare here the resulting depth-averaged equations, (2.26) and (3.16d).

Notice that in the Iverson-George model the evolution equation is established for the basal fluid pressure, while our proposal (2.26), developed in section A.6, is derived for the basal solid pressure. Let us then write our equation (A.30) in terms of the fluid pressure by using the relation $p_{s|b} = -p_{f_m|b} + g \cos \theta (\rho_f h_f + \rho h_m)$. First we compute the following transport term by using mass equations (2.12) and (2.21).

$$\begin{aligned} \partial_t (\rho_f h_f + \rho h_m) + \bar{v} \cdot \nabla (\rho_f h_f + \rho h_m) &= \partial_t (\rho_f h_f + \rho h_m) + \nabla \cdot ((\rho_f h_f + \rho h_m) \bar{v}) - (\rho_f h_f + \rho h_m) \nabla \cdot \bar{v} \\ &= \rho_f (\mathcal{V}_f - h_f \nabla \cdot \bar{v}) + \nabla \cdot (\rho_f h_f (\bar{v} - \bar{u}_f)) + \rho_f h_m \bar{\Phi} - \rho h_m \nabla \cdot \bar{v} \\ &= -(\rho_f h_f + \rho h_m) \nabla \cdot \bar{v} + \rho_f \nabla \cdot ((1 - \varphi) h_m (\bar{v} - \bar{u}) + h_f (\bar{v} - \bar{u}_f)). \end{aligned}$$

The equation (2.26) reads

$$\begin{aligned} \partial_t p_{f_m|b} + \bar{v} \cdot \nabla p_{f_m|b} &= -\frac{1}{4} g \cos \theta ((5\rho - \rho_f) h_m + 4\rho_f h_f) \nabla \cdot \bar{v} + \frac{3}{2} B (\bar{\Phi} - \bar{\gamma} \tan \bar{\psi}) \\ &\quad + \rho_f g \cos \theta \nabla \cdot \left((1 - \varphi) h_m (\bar{v} - \bar{u}) + h_f (\bar{v} - \bar{u}_f) \right). \end{aligned} \quad (\text{C.10})$$

Let us compare equations (C.9) and (C.10) under $\alpha = 1/B$ and $D = h\bar{\Phi}$. Notice that for a unique velocity $\bar{u} = \bar{v} = \bar{u}_f$ the last term in (C.10) vanishes. The additional term in the Iverson-George model equation (C.9) related to D , $\frac{1}{4} g \cos \theta \rho_f \frac{\rho - \rho_f}{\rho} D$, comes from the mass equations written in terms of the virtual surface – equations (4.5) and (4.6) in [23] – that read

$$\partial_t (\rho h) + \nabla \cdot (\rho h \bar{v}) = 0, \quad \partial_t h + \nabla \cdot (h \bar{v}) = \frac{\rho - \rho_f}{\rho} D.$$

These equations are used during the integration procedure providing the additional term in the Iverson-George model equation (C.9). In our case the depth-averaging is made in $[0, h_m]$ instead of $[0, H]$, so we use the corresponding mass equation ,

$$\partial_t h_m + \nabla \cdot (h_m \bar{v}) = h_m \bar{\Phi}.$$

Finally, the different coefficients of the densities that go with $\nabla \cdot \bar{v}$ in the first term on the r.h.s., come from the particular parabolic profile of the pressure assumed in [23], as shown above. The corresponding term in (C.10) is also written as

$$-\frac{1}{4}g \cos \theta ((5\rho - \rho_f)H - (\rho - \rho_f)\Delta_H) \nabla \cdot \bar{v}$$

so even neglecting Δ_H these coefficients do not coincide.

D Comparison with the Meng-Wang model: further details

D.1 Details of calculations

In section 4.4.2 we summarized the hypothesis under which the Meng-Wang model becomes our model (C1). Here we give a detailed explanation of this comparison in order to conclude that the equivalence is achieved under condition (3.13), $\Delta_H \ll 1$, as for the Iverson-George model.

The total mass conservation is given in (4.10) for our model and, for the Meng-Wang model it is obtained as the sum of the mass equations in (4.16)

$$\partial_t(\rho h) + \nabla \cdot (\rho h V_m) = 0.$$

This leads to the same conclusion than for the Iverson-George model, that is, the equivalence between the virtual surface h and our virtual thickness H . Under this identification we recover the equivalence of the mass equations of the two systems (4.11a), (4.11b) and (4.16b), (4.16a) with \mathfrak{J} in (4.16e), bridging the difference between the dilatancy laws. The equation of the upper fluid layer is neglected under (3.13) which also implies that $\mathcal{V}_f \ll 1$. But contrarily to the Iverson-George model case, this assumption not only implies $|\Phi| \ll 1$, but also that $u - v \ll 1$ from the definition of \mathcal{V}_f in (4.11f). As in the precedent case, we will keep however this effect in the system, together with two different velocities. Under $\Delta_H \ll 1$, we find the following equivalence between \mathfrak{J} and \mathcal{V}_f ,

$$\mathfrak{J} = \varphi \frac{\rho_f \rho_s}{\rho} \mathcal{V}_f \simeq \varphi \frac{\rho_f \rho_s}{\rho} \mathcal{V}_f^*. \quad (\text{D.1})$$

with \mathcal{V}_f^* in (4.14).

Now we compare the momentum equations. Since we do not kept the viscous terms in the stress tensor, we must neglect the last term in (4.16d). We notice that $h = H$ is not enough to obtain the equivalence of the convective terms, and we must use again (3.13). We look carefully at the rest of the terms: pressure, mass exchange and friction.

Let us start with the pressure terms. Under $b = 0$, the equivalence of the hydrostatic pressure terms is found under (3.13). Regarding the excess pore pressure terms, in the solid and fluid equations it appears

$$\begin{aligned} \text{for Meng-Wang (4.16):} & \quad (1 - \varphi) \nabla (h p_e), \\ \text{for our model (4.11):} & \quad (1 - \varphi) (H - \Delta_H) \overline{\nabla p_{f_m}^e}, \end{aligned}$$

where $\overline{\nabla p_{f_m}^e}$ is given by (4.5). Notice that p_e and $\overline{p_{f_m}^e}$ represent the depth-averaged excess pore pressures for each model. We will consider the bold notation for the z -dependent pressures in this section to avoid confusion. From the definition of these averages we have $\nabla(hp_e) = \nabla\left(\int_b^{b+h} \mathbf{p}_e\right)$ and

$$\overline{\nabla p_{f_m}^e} = \frac{1}{h_m} \int_b^{b+h_m} \nabla \mathbf{p}_{f_m}^e = \frac{1}{h_m} \left(\nabla \int_b^{b+h_m} \mathbf{p}_{f_m}^e - (\mathbf{p}_{f_m}^e)_{|b+h_m} \nabla(b+h_m) + (\mathbf{p}_{f_m}^e)_{|b} \nabla b \right),$$

which gives (4.5a) since $(\mathbf{p}_{f_m}^e)_{|b+h_m} = 0$ from its definition (2.28). Using that $h_m = H - \Delta_H$, both expressions coincide in the case $b = 0$ and $\Delta_H \ll 1$. Despite the equivalence of the definitions, the approximations of the pore pressure given by (4.16h) for the Meng-Wang model and (4.5) for our model, differs in the explicit quantities:

$$\begin{aligned} \text{for Meng-Wang:} \quad \nabla(hp_e) &= \nabla \left(-\frac{h^3}{3} \frac{\beta}{(1-\varphi)^2} \left(\Phi_{\text{MW}} + \nabla((1-\varphi)(u-v)) \right) \right), \\ \text{for our model:} \quad (H - \Delta_H) \overline{\nabla p_{f_m}^e} &= \nabla \left(-\frac{(H-\Delta_H)^3}{3} \frac{\beta}{(1-\varphi)^2} \Phi \right). \end{aligned}$$

Indeed the term appearing in the Meng-Wang model corresponds to the case of $\beta \sim O(1)$ studied in [7], where the values of $\overline{p_{f_m}^e}$ and $(p_{f_m}^e)_{|b}$ are given in equations (3.58)-(3.59) of that paper matching with (4.16h) for $b = 0$.

Let us continue with the mass exchange term that reads

$$\begin{aligned} \text{for Meng-Wang (4.16):} \quad & ((1-\lambda)u + \lambda v) \mathfrak{J}, \\ \text{for our model (4.11):} \quad & \frac{\rho_s \varphi}{\rho} ((1-\lambda_f)u + \lambda_f V_m) \rho_f \mathcal{V}_f. \end{aligned}$$

Assuming the equivalence in (D.1), and again $\Delta_H \ll 1$ a simple calculation leads to match

$$\lambda = \frac{\varphi \rho_s}{\rho} \lambda_f \simeq \frac{\varphi \rho_s}{\rho} \lambda_f^*. \quad (\text{D.2})$$

There are three friction terms. The one with the relative velocity, $\beta(u-v)$, is equivalent under $h = H$. The basal solid friction reads

$$\begin{aligned} \text{for Meng-Wang (4.16):} \quad & -\text{sgn}(v) \mu_{\text{MW}} \left(\varphi(\rho_s - \rho_f) h g \cos \theta - (p_e)_{|b} \right) - \alpha_s \varphi v \\ \text{for our model (4.11):} \quad & -\text{sgn}(v) \mu \left(\varphi(\rho_s - \rho_f) g \cos \theta (H - \Delta_H) - (p_{f_m}^e)_{|b} \right) \end{aligned}$$

and the basal fluid friction,

$$\begin{aligned} \text{for Meng-Wang (4.16):} \quad & -\alpha_f (1-\varphi) u, \\ \text{for our model (4.11):} \quad & -\frac{5}{2} \frac{\eta_e (1-\varphi)}{h_m} u. \end{aligned}$$

Thus it is easy to conclude that for a complete equivalence α_s must vanish and $\alpha_f = \frac{5}{2} \frac{\eta_e}{h_m}$. The difference in the approximation of the excess pore pressure indicated before also affects the Coulomb friction term. The remaining differing terms appearing in our model (4.11) are the last ones in momentum equations that are neglected again under $\Delta_H \ll 1$.

Therefore, as for the Iverson-George model the equivalence $h \simeq H$ and the condition (3.13) are needed to identify the systems.

D.2 Comparison of the boundary conditions

As discussed in Section 4.4, the Meng-Wang model is a depth-averaged model based on the 3D Jackson's equations. The concept of the virtual surface, introduced by Iverson and George [23],

is used to derive the model, thereby the real free surface is not solved. In contrast to the Iverson-George model, the Meng-Wang model solves for two velocities, one for each phase (as in our (C1) model, see figure 3C1). Additionally, the flux of granular or liquid mass through the virtual surface is quantified in the model through specific boundary conditions at the virtual surface level. Since this is not a trivial matter, we present here the boundary conditions considered in [35] and highlight the main similarities and differences with respect to the ones considered for our model, in Section A.1. Note that in our case the configuration is different because instead of the virtual surface, we have the free surface $b + h_m + h_f$ and the interface $b + h_m$ that separate the mixture layer from the upper fluid layer (see figure 1).

The virtual surface in the Meng-Wang model is driven following the mixture velocity through the kinematic condition

$$\partial_t(b + h) + \mathbf{V}_m \cdot N_X^{vs} = 0, \quad (\text{D.3})$$

where N_X^{vs} is the normal vector to the virtual surface. This condition seems reasonable, considering that the virtual surface can be defined by both the solid and liquid phases. In our configuration, the free surface moves with velocity \mathbf{u}_f , (A.4), and the interface moves with solid velocity \mathbf{v} (A.7).

To introduce the flux through the interface, Meng and Wang consider a zero momentum jump at the virtual surface that is calculated from the momentum equations of the 3D system,

$$(\sigma_s + \sigma_{f_m})N_X^{vs} = \rho_s \varphi (\mathbf{v} - \mathbf{u}) \left((\mathbf{v} - \mathbf{V}_m) \cdot N_X^{vs} \right). \quad (\text{D.4})$$

Then \mathfrak{J} is introduced as the flux of granular mass through the interface in terms of the solid velocity,

$$\mathfrak{J} = -\rho_s \varphi (\partial_t(b + h) + \mathbf{v} \cdot N_X^{vs}). \quad (\text{D.5})$$

But using previous condition (D.3) and the definition of \mathbf{V}_m , \mathfrak{J} is equivalently defined as

$$\mathfrak{J} = \rho_f (1 - \varphi) (\partial_t(b + h) + \mathbf{u} \cdot N_X^{vs}). \quad (\text{D.6})$$

So \mathfrak{J} can also be interpreted as the flux of the fluid mass through the virtual surface. Notice that (D.6) is equivalent to our definition of the fluid mass flux at the interface $\rho_f \mathcal{V}_f$ introduced in (A.8), for $h = h_m$. As detailed in equation (D.1), we can identify $\rho_f \mathcal{V}_f$ and \mathfrak{J} up to a coefficient. Nevertheless, instead of (D.5) we have (A.7) and (A.8), where we establish that the fluid mass flux is exactly balanced by the upper fluid layer and that the solid phase does not leave the mixture layer. In the Meng-Wang model the flux \mathfrak{J} describes both the solid entering the mixture and the fluid expelled or the contrary. By using again the kinematic condition (D.3) it is possible to write the following alternative expression

$$\mathfrak{J} = -\rho_s \varphi (\mathbf{v} - \mathbf{V}_m) \cdot N_X^{vs}, \quad (\text{D.7})$$

hence the momentum condition (D.4) is equivalently written as

$$(\sigma_s + \sigma_{f_m})N_X^{vs} = -(\mathbf{v} - \mathbf{u}) \mathfrak{J}. \quad (\text{D.8})$$

Besides the different velocities, this condition looks similar to the total momentum conservation (A.9) where σ_f is neglected. As we discussed in section A.3 this quantity must be distributed among the phases in order to have complete boundary conditions. In [35] this distribution is made through the coefficient $\lambda = 1 - \varphi$ as follows

$$\begin{aligned} \sigma_s N_X^{vs} &= -(1 - \lambda) (\mathbf{v} - \mathbf{u}) \mathfrak{J}, \\ \sigma_{f_m} N_X^{vs} &= -\lambda (\mathbf{v} - \mathbf{u}) \mathfrak{J}. \end{aligned} \quad (\text{D.9})$$

By denoting E_f^{MW} the corresponding tangential projection of the flux as in (A.10), $E_f^{\text{MW}} = (\mathbf{v} - \mathbf{u})_{\text{tg}} \mathfrak{J}$, the tangent component of previous relations reads

$$\begin{aligned} (\sigma_s N_X^{vs})_{\text{tg}} &= -(1 - \lambda) E_f^{\text{MW}}, \\ (\sigma_{f_m} N_X^{vs})_{\text{tg}} &= -\lambda E_f^{\text{MW}}. \end{aligned} \quad (\text{D.10})$$

So they also follow the same form as in (A.12), where F_d (drag term) is neglected. Again, this highlights that, due to the virtual surface, the solid that enters the mixture replaces the equivalent mass of fluid in the mixture while the solid expelled from the mixture is replaced by the equivalent mass of fluid.

E Calculation details of the two-phase model (B1)

The model (B1) presented in section 4 is based on the assumption that the upper-fluid layer moves with the mixture velocity V_m assuming $k_f \rightarrow \infty$ in the full model (A1). The combination of momentum equations can not a priori be written in a conservative form and some calculations are needed to obtain the proposed equations (4.4). Here we detail such calculation.

The total momentum conservation equation, as the sum of equations in (2.14), reads

$$\begin{aligned} &\partial_t \left((\rho h_m + \rho_f h_f) V_m \right) + \nabla \cdot \left(\rho_s \varphi h_m v \otimes v + \rho_f (1 - \varphi) h_m u \otimes u + \rho_f h_f V_m \otimes V_m \right) \\ &= -g \cos \theta \nabla \left((\rho_s - \rho_f) \varphi \frac{h_m^2}{2} + \rho_f \frac{(h_m + h_f)^2}{2} \right) \\ &\quad - \text{sgn}(v) \mu \left(\varphi (\rho_s - \rho_f) g \cos \theta h_m - (p_{f_m}^e)_{|b} \right) - \frac{5 \eta_e (1 - \varphi)}{2 h_m} u - (\rho h_m + \rho_f h_f) (g \cos \theta \nabla b + g \sin \theta \mathbf{e}_x). \end{aligned} \quad (\text{E.1})$$

The combination of the fluid equations (2.14b) + $\frac{\rho_f(1-\varphi)}{\rho} \times$ (2.14c) gives

$$\begin{aligned} &\partial_t (\rho_f (1 - \varphi) h_m u) + \nabla \cdot (\rho_f (1 - \varphi) h_m u \otimes u) + \frac{\rho_f (1 - \varphi)}{\rho} (\partial_t (\rho_f h_f V_m) + \nabla \cdot (\rho_f h_f V_m \otimes V_m)) \\ &= -(1 - \varphi) \frac{\rho h_m + \rho_f h_f}{\rho} \rho_f g \cos \theta \nabla (b + h_m + h_f) - (1 - \varphi) h_m \overline{\nabla p_{f_m}^e} - \beta h_m (u - v) \\ &\quad - \frac{\rho_s \varphi}{\rho} ((1 - \lambda_f) u + \lambda_f V_m) \rho_f \mathcal{V}_f - \frac{5 \eta_e (1 - \varphi)}{2 h_m} u - (1 - \varphi) \frac{\rho h_m + \rho_f h_f}{\rho} \rho_f g \sin \theta \mathbf{e}_x. \end{aligned} \quad (\text{E.2})$$

We work on (E.2) to find a conservative formulation. Notice that

$$\frac{\rho_f (1 - \varphi)}{\rho} \partial_t (\rho_f h_f V_m) = \partial_t \left(\frac{\rho_f (1 - \varphi)}{\rho} \rho_f h_f V_m \right) + \frac{\rho_f^2 \rho_s}{\rho^2} h_f V_m \partial_t \varphi$$

and

$$\frac{\rho_f (1 - \varphi)}{\rho} \nabla \cdot (\rho_f h_f V_m \otimes V_m) = \nabla \cdot \left(\frac{\rho_f (1 - \varphi)}{\rho} \rho_f h_f V_m \otimes V_m \right) + \frac{\rho_f^2 \rho_s}{\rho^2} h_f (V_m \otimes V_m) \nabla \varphi$$

where we used $\phi \nabla \cdot (w_1 \otimes w_2) = \nabla \cdot (\phi w_1 \otimes w_2) - (w_1 \otimes w_2)^t \nabla \phi$ for any scalar ϕ and any vectors w_1, w_2 .

Now we use (4.3) to write the two terms on φ , using also that $(w_1 \otimes w_2)\nabla\phi = w_1(w_2 \cdot \nabla\phi)$,

$$\frac{\rho_f^2 \rho_s}{\rho^2} h_f (V_m \partial_t \varphi + (V_m \otimes V_m) \nabla \varphi) = \frac{\rho_f^2 \rho_s}{\rho^2} h_f V_m (-\varphi \Phi + (V_m - v) \cdot \nabla \varphi).$$

Hence (E.2) finally reads as in (4.4b)

$$\begin{aligned} & \partial_t \left(\rho_f (1 - \varphi) \left(h_m u + \frac{\rho_f h_f}{\rho} V_m \right) \right) + \nabla \cdot \left(\rho_f (1 - \varphi) \left(h_m u \otimes u + \frac{\rho_f h_f}{\rho} V_m \otimes V_m \right) \right) \\ &= -(\rho h_m + \rho_f h_f) \frac{\rho_f (1 - \varphi)}{\rho} g \cos \theta \nabla (b + h_m + h_f) - (1 - \varphi) h_m \overline{\nabla p_{f_m}^e} \\ & \quad - \beta h_m (u - v) - \frac{\rho_s \varphi}{\rho} ((1 - \lambda_f) V_m + \lambda_f u) \rho_f \mathcal{V}_f - \frac{5 \eta_e (1 - \varphi)}{2 h_m} u \\ & \quad - (\rho h_m + \rho_f h_f) \frac{\rho_f (1 - \varphi)}{\rho} g \sin \theta \mathbf{e}_x + \frac{\rho_f^2 \rho_s}{\rho^2} h_f V_m (\varphi \Phi + (v - V_m) \cdot \nabla \varphi). \end{aligned} \tag{E.3}$$

An alternative momentum equation is found by subtracting equation (E.3) from the total one (E.1), thus obtaining an equation involving the solid phase velocity (4.4a).

Notice that neither (E.2) nor (4.4a) are the conservation momentum equation for the solid and fluid phases because they have been obtained as a special combination of the original equations. These equations are written straightforward in terms of the virtual thickness H yielding (4.11d) and (4.11e).

Let us detail the writing of the solid mass equation (4.11a) in terms of H for the readers' convenience. Those for the fluid phase being equivalent. From the solid mass equation (4.1a) using the definition of H we write

$$\partial_t(\varphi H) + \nabla \cdot (\varphi H v) = \partial_t \left(\frac{\rho_f}{\rho} \varphi h_f \right) + \nabla \cdot \left(\frac{\rho_f}{\rho} \varphi h_f v \right).$$

Now we use the equation of h_f to write

$$\partial_t \left(\frac{\rho_f}{\rho} \varphi h_f \right) = \frac{\rho_f}{\rho} \left(\varphi \mathcal{V}_f - \frac{\rho_f}{\rho} h_f \varphi \Phi - \varphi \nabla \cdot (h_f V_m) - \frac{\rho_f}{\rho} h_f v \cdot \nabla \varphi \right)$$

and we develop

$$\nabla \cdot \left(\frac{\rho_f}{\rho} \varphi h_f v \right) = \frac{\rho_f}{\rho} h_f v \cdot \nabla \varphi + \varphi \nabla \cdot \left(\frac{\rho_f}{\rho} h_f v \right).$$

Using the expression of \mathcal{V}_f in (4.2) and rearranging terms we find

$$\partial_t(\varphi H) + \nabla \cdot (\varphi H v) = -\frac{\rho_f}{\rho} \varphi H \Phi - \frac{\rho_f}{\rho} \varphi \nabla \cdot (h_m (1 - \varphi) (u - v) + h_f (V_m - v)).$$

Notice that from the definition of the mixture velocity V_m we write $V_m - v = \frac{\rho_f (1 - \varphi) (u - v)}{\rho}$, then it yields (4.11a).

F Alternative simplified models

In this section we present other simplified versions of the full model (A1) by considering different ideas. Namely we propose a one-layer one-velocity model where the solid mass is conserved instead of the total mass. Next two options already presented in previous works for two-layers two-velocities models are summarized. For the first one, originally presented in [14], the phases in the mixture are supposed to have the same velocity leading to the (A2) model (figure 3A2). The second one, presented in [7], is obtained by considering that the fluid phases (in the mixture and in the upper layer) move with the same velocity (see figure 25).

F.1 One-layer one-velocity model with solid mass conservation

We present here an alternative one-velocity model to the oversimplified model (C2) presented in Section 3. The idea is to preserve the conservation of solid mass instead of total mass, and to use the acceleration equation instead of total momentum conservation. With this choice, we do not preserve the total mass or the fluid mass. The interpretation of such a system could be to consider a mixture layer of fluid and granular material with an 'infinite' fluid layer above, from which we can always expel some fluid when contraction occurs, and from where we can always absorb some fluid when dilation occurs. The dilatancy effect in the model is retained, as in model (3.14), appearing in the continuity equation of the volume fraction and as a part of the friction law through the excess pore pressure p_{fm}^e .

As in section 3.2, we aim to find a model with a unique thickness and one velocity. In model (C2), we preserved the total mass conservation ρH with the objective of finding the Iverson-George model. However, as mentioned in Section 3.2, for that choice, neither the solid mass nor the fluid mass are preserved. In the model proposed here, we maintain h_m as the unique thickness of the model, and we neglect h_f in the system. Consequently, similar to model (C2), we do not solve equation (3.1b). The proposed alternative mixture model for unknowns h_m, φ, v is given by the following equations

$$\partial_t(\varphi h_m) + \nabla \cdot (\varphi h_m v) = 0, \quad (\text{F.1a})$$

$$\partial_t \varphi + v \cdot \nabla \varphi = -\varphi \Phi, \quad (\text{F.1b})$$

$$\begin{aligned} \partial_t(\rho h_m v) + \nabla \cdot (\rho h_m v \otimes v) + g \cos \theta \nabla \left(\rho \frac{h_m^2}{2} \right) - \rho_f h_m v \Phi \\ = -\rho h_m g \cos \theta \nabla b - \rho h_m g \sin \theta \mathbf{e}_x - \text{sgn}(v) \mu \left((\rho - \rho_f) g \cos \theta h_m - (p_{fm}^e)_{|b} \right) - \frac{5 \eta_e (1 - \varphi)}{2 h_m} v, \end{aligned} \quad (\text{F.1c})$$

together with relations in (2.18) and (2.16b) for the dilatancy law and the pore pressure. Notice that the term $\rho_f h_m v \Phi$ in the momentum equation must be added to be consistent with the considered mass equations.

As we mentioned before, the model (F.1) conserve solid mass and volume, but it does not preserve the total mass and the fluid mass and neither their associated volumes. If we write them from (F.1) we find the following equations for the volumes,

$$\begin{aligned} \text{total volume:} \quad & \partial_t h_m + \nabla \cdot (h_m v) = h_m \Phi, \\ \text{fluid volume:} \quad & \partial_t((1 - \varphi)h_m) + \nabla \cdot ((1 - \varphi)h_m v) = h_m \Phi, \end{aligned}$$

and for the masses

$$\begin{aligned} \text{total mass:} \quad & \partial_t(\rho h_m) + \nabla \cdot (\rho h_m v) = \rho_f h_m \Phi, \\ \text{fluid mass:} \quad & \partial_t(\rho_f(1 - \varphi)h_m) + \nabla \cdot (\rho_f(1 - \varphi)h_m v) = \rho_f h_m \Phi. \end{aligned} \quad (\text{F.2})$$

As for the model (C2), these equations show that the conservation of volume and mass are recovered at the order of the dilatancy Φ (supposed to be small in this case).

F.2 Two layer model with one velocity in the mixture and one velocity in the upper-fluid layer (A2)

This model, presented in [14], is obtained as the limit of the complete model when the friction coefficient between the two phases in the mixture β tends to infinity, that leads $u = v$ as we

did to obtain the model (C1). We thus consider that the fluid and solid phases in the mixture moves with the same velocity, that also equals the velocity of the mixture $V_m = v$. Nevertheless we keep a different velocity for the fluid upper layer, u_f (see figure 3A2).

We write the obtained model for unknowns $h_m, h_f, \varphi, v, u_f$. The mass equations read

$$\partial_t h_m + \nabla \cdot (h_m v) = -\mathcal{V}_f, \quad (\text{F.3a})$$

$$\partial_t h_f + \nabla \cdot (h_f u_f) = \mathcal{V}_f, \quad (\text{F.3b})$$

$$\partial_t \varphi + v \cdot \nabla \varphi = -\varphi \Phi. \quad (\text{F.3c})$$

The momentum conservation equation for the mixture is the sum of (2.14a) and (2.14b),

$$\begin{aligned} \partial_t(\rho h_m v) + \nabla \cdot (\rho h_m v \otimes v) &= -\rho h_m g \cos \theta \nabla(b + h_m) - \rho_f h_m g \cos \theta \nabla h_f \\ &\quad -(\rho_s - \rho_f) g \cos \theta \frac{h_m^2}{2} \nabla \varphi - ((1 - \lambda_f)v + \lambda_f u_f) \rho_f \mathcal{V}_f \\ &\quad - \text{sgn}(v) \mu (\varphi(\rho_s - \rho_f) g \cos \theta h_m - (p_{f_m}^e)|_b) \\ &\quad + k_f(u_f - v) - \frac{5}{2} \frac{\eta_e(1 - \varphi)}{h_m} v - \rho h_m g \sin \theta \mathbf{e}_x. \end{aligned} \quad (\text{F.4a})$$

Finally the momentum equation for the upper fluid layer does not change and it is given by (2.14c),

$$\begin{aligned} \partial_t(\rho_f h_f u_f) + \nabla \cdot (\rho_f h_f u_f \otimes u_f) &= -\rho_f h_f g \cos \theta \nabla(b + h_m + h_f) \\ &\quad + ((1 - \lambda_f)v + \lambda_f u_f) \rho_f \mathcal{V}_f - k_f(u_f - v) \\ &\quad - \rho_f h_f g \sin \theta \mathbf{e}_x. \end{aligned} \quad (\text{F.4b})$$

The fluid transfer rate in (2.21) gives $\mathcal{V}_f = -h_m \Phi$. Notice that the excess pore pressure only appear in the friction term at the bottom. The closures are the same as for the original model in (2.16b)-(2.22).

F.3 Two-layer model with one velocity for each phase

This simplification was already presented in Section 4.3 of [7], but we include it here for the sake of completeness for our hierarchy of models. Remember that in [7] the friction between the layers at the interface was taken proportional to $(u_f - u)$. This model was thus obtained as the limit of an infinity friction between the layers, that leads to equal velocity of the fluid phase in the mixture and in the upper-fluid layer $u_f = u$ (see figure 25).

The resulting model with unknowns h_m, h_f, φ, u, v states as follows. The mass equations read

$$\partial_t(\varphi h_m) + \nabla \cdot (\varphi h_m v) = 0, \quad (\text{F.5a})$$

$$\partial_t((1 - \varphi)h_m + h_f) + \nabla \cdot (((1 - \varphi)h_m + h_f)u) = 0, \quad (\text{F.5b})$$

$$\partial_t \varphi + v \cdot \nabla \varphi = -\varphi \Phi. \quad (\text{F.5c})$$

The momentum conservation equations are

$$\begin{aligned} \partial_t(\rho_s \varphi h_m v) + \nabla \cdot (\rho_s \varphi h_m v \otimes v) &= -\varphi h_m g \cos \theta (\rho_s \nabla(b + h_m) + \rho_f \nabla h_f) \\ &\quad -(\rho_s - \rho_f) g \cos \theta \frac{h_m^2}{2} \nabla \varphi + (1 - \varphi) h_m \overline{\nabla p_{f_m}^e} \\ &\quad - \text{sgn}(v) \mu (\varphi(\rho_s - \rho_f) g \cos \theta h_m - (p_{f_m}^e)|_b) \\ &\quad + \beta h_m (u - v) - \varphi h_m \rho_s g \sin \theta \mathbf{e}_x, \end{aligned} \quad (\text{F.5d})$$

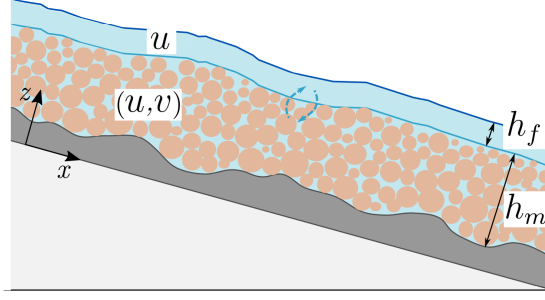


Figure 25: Sketch for the two-layer model with two velocities in the mixture and the upper-fluid velocity u .

$$\begin{aligned}
\partial_t(\rho_f((1-\varphi)h_m + h_f)u) &+ \nabla \cdot (\rho_f((1-\varphi)h_m + h_f)u \otimes u) \\
&= -((1-\varphi)h_m + h_f)\rho_f g \cos \theta \nabla(b + h_m + h_f) \\
&\quad - (1-\varphi)h_m \overline{\nabla p_{fm}^e} - \frac{5\eta_e(1-\varphi)}{2h_m}u \\
&\quad - \beta h_m(u-v) - ((1-\varphi)h_m + h_f)\rho_f g \sin \theta \mathbf{e}_x.
\end{aligned} \tag{F.5e}$$

Notice that the exchange term no longer appears in this two-velocity model. The closures are the same as for the original model, given by equations (2.16a)-(2.20). The energy balance of this model has been already presented in [7].

G Models in uniform regime

In this section a summary of the models in uniform configuration is presented. First we present our series of models, accordingly to the classification made in figure 3, then we write the Iverson-George model and the Meng-Wang model.

G.1 Our hierarchy of models in uniform regime

(A1) Two-layer model with three velocities

The complete model (2.12)-(2.21) for unknowns $h_m, h_f, \varphi, v, u, u_f$ in uniform regime, taking into account that $\mathcal{V}_f = -h_m\Phi$, reads as follows.

$$\partial_t h_m = h_m \Phi, \tag{G.1a}$$

$$\partial_t h_f = -h_m \Phi, \tag{G.1b}$$

$$\partial_t \varphi = -\varphi \Phi, \tag{G.1c}$$

$$\partial_t v = -\mu \operatorname{sgn}(v) \frac{p_{s|b}}{\rho_s \varphi h_m} + \frac{\beta}{\rho_s \varphi} (u-v) + \frac{k_f}{\rho h_m} (u_f - V_m) - g \sin \theta \mathbf{e}_x, \tag{G.1d}$$

$$\partial_t u = -\lambda_f \frac{\Phi}{(1-\varphi)} (u - u_f) - \frac{\beta}{\rho_f (1-\varphi)} (u-v) + \frac{k_f}{\rho h_m} (u_f - V_m) - \frac{5}{2} \frac{\eta_e}{\rho_f h_m^2} u - g \sin \theta \mathbf{e}_x, \tag{G.1e}$$

$$\partial_t u_f = -(1-\lambda_f) \frac{h_m \Phi}{h_f} (u - u_f) - \frac{k_f}{\rho_f h_f} (u_f - V_m) - g \sin \theta \mathbf{e}_x, \tag{G.1f}$$

together with the following closures

$$\beta = \frac{150\eta_f\varphi^2}{(1-\varphi)d^2}, \quad k_f = \frac{\rho h_m \rho_f h_f}{\rho h_m + \rho_f h_f} |u_f - V_m|, \quad \lambda_f = \frac{1}{2} + \frac{1}{2} \operatorname{sgn}(\Phi) \delta_f, \quad \delta_f = \begin{cases} 0 & \text{centered dist.}, \\ 1 & \text{upwind dist.}, \end{cases} \quad (\text{G.2a})$$

and the effective viscosity $\eta_e = \eta_f(1 + \frac{5}{2}\varphi)$. The friction coefficient is

$$\mu = (\mu^{\text{eq}} + K(\varphi - \varphi^{\text{eq}}))_+. \quad (\text{G.2b})$$

The rheological laws give

$$\begin{aligned} \varphi^{\text{eq}} &= \frac{\varphi_c}{1 + b_\varphi \mathcal{J}_\varphi^{1/2}} \quad \text{with} \quad \mathcal{J}_\varphi = \alpha_\varphi I^2 + J, \\ \mu^{\text{eq}} &= \mu_c + \frac{\Delta\mu}{1 + I_0/\mathcal{J}_\mu^{1/2}} \quad \text{with} \quad \mathcal{J}_\mu = \alpha_\mu I^2 + J, \\ \text{where} \quad I &= \frac{d\dot{\gamma}}{\sqrt{p_{s|b}/\rho_s}}, \quad J = \frac{\eta_f \dot{\gamma}}{p_{s|b}}, \quad \dot{\gamma} = \frac{5|v|}{2h_m}. \end{aligned} \quad (\text{G.2c})$$

As we discussed previously, there are two options to set the definition of the basal solid pressure.

Option 1 for the computation of $p_{s|b}$. The first option is done by the definition of the basal solid pressure $p_{s|b}$ as $p_{s|b} = \varphi(\rho_s - \rho_f)g \cos \theta h_m - (p_{f_m}^e)_{|b}$, with $(p_{f_m}^e)_{|b} = -\frac{\beta}{(1-\varphi)^2} \frac{h_m^2}{2} \Phi$, where the dilatancy function (G.1) is given by

$$\Phi = \dot{\gamma} K(\varphi - \varphi^{\text{eq}}). \quad (\text{G.3a})$$

Note that taking into account the definition of φ^{eq} , it implies an implicit definition of $p_{s|b}$. Namely, as explained in Section 2.3.2, it can be seen that $\sqrt{p_{s|b}}$ is a root of a third order polynomial,

$$\begin{aligned} &(\sqrt{p_{s|b}})^3 + A_2(\sqrt{p_{s|b}})^2 \\ &- (\varphi(\rho_s - \rho_f)g \cos \theta h_m + A_1(\varphi - \varphi_c))(\sqrt{p_{s|b}}) - A_2(\varphi(\rho_s - \rho_f)g \cos \theta h_m + \varphi A_1) = 0 \end{aligned} \quad (\text{G.3b})$$

with coefficients $A_1 = \frac{\beta}{(1-\varphi)^2} \frac{h_m^2}{2} \dot{\gamma} K$, $A_2 = b(\alpha_\varphi d^2 \dot{\gamma}^2 \rho_s + \eta_f \dot{\gamma})^{1/2}$.

Option 2 for the computation of $p_{s|b}$ The basal solid pressure is the solution of the following equation

$$\partial_t p_{s|b} = -\frac{3}{2} B(\Phi - \dot{\gamma} K(\varphi - \varphi^{\text{eq}})), \quad (\text{G.4a})$$

with B the solid bulk modulus. In this case, the dilatancy function Φ is written in terms of the basal solid pressure using the expression of $(p_{f_m}^e)_{|b}$ that gives

$$\Phi = \frac{2(1-\varphi)^2}{\beta h_m^2} (p_{s|b} - \varphi(\rho_s - \rho_f)g \cos \theta h_m). \quad (\text{G.4b})$$

(A2) Two-layer model with one velocity in the mixture and an independent velocity in the upper-layer

The model with two velocities and an upper fluid layer in Appendix F.2, with unknowns $h_m, h_f, \varphi, u_f, v$ given in (F.3)-(F.4) reads

$$\partial_t h_m = h_m \Phi, \quad (\text{G.5a})$$

$$\partial_t h_f = -h_m \Phi, \quad (\text{G.5b})$$

$$\partial_t \varphi = -\varphi \Phi, \quad (\text{G.5c})$$

$$\partial_t v = \frac{\rho_f}{\rho} \lambda_f \Phi (u_f - v) - \mu \operatorname{sgn}(v) \frac{p_{s|b}}{\rho h_m} + \frac{k_f}{\rho h_m} (u_f - v) - \frac{5 \eta_e (1 - \varphi)}{2 \rho h_m^2} v - g \sin \theta \mathbf{e}_x, \quad (\text{G.5d})$$

$$\partial_t u_f = (1 - \lambda_f) \frac{h_m \Phi}{h_f} (u_f - v) - \frac{k_f}{\rho_f h_f} (u_f - v) - g \sin \theta \mathbf{e}_x, \quad (\text{G.5e})$$

together with the following closures

$$\lambda_f = \frac{1}{2} + \frac{1}{2} \operatorname{sgn}(\Phi) \delta_f, \quad \delta_f = \begin{cases} 0 & \text{centered distribution,} \\ 1 & \text{upwind distribution,} \end{cases} \quad (\text{G.6a})$$

$k_f = \frac{\rho h_m \rho_f h_f}{\rho h_m + \rho_f h_f} |u_f - v|$ and $\eta_e = \eta_f (1 + \frac{5}{2} \varphi)$. The friction coefficient is

$$\mu = (\mu^{\text{eq}} + K(\varphi - \varphi^{\text{eq}}))_+. \quad (\text{G.6b})$$

The rheological laws are

$$\begin{aligned} \varphi^{\text{eq}} &= \frac{\varphi_c}{1 + b_\varphi \mathcal{J}_\varphi^{1/2}} \quad \text{with} \quad \mathcal{J}_\varphi = \alpha_\varphi I^2 + J, \\ \mu^{\text{eq}} &= \mu_c + \frac{\Delta \mu}{1 + I_0 / \mathcal{J}_\mu^{1/2}} \quad \text{with} \quad \mathcal{J}_\mu = \alpha_\mu I^2 + J, \\ \text{where} \quad I &= \frac{d \dot{\gamma}}{\sqrt{p_{s|b} / \rho_s}}, \quad J = \frac{\eta_f \dot{\gamma}}{p_{s|b}}, \quad \dot{\gamma} = \frac{5 |v|}{2 h_m}. \end{aligned} \quad (\text{G.6c})$$

The basal solid pressure $p_{s|b}$ is defined as $p_{s|b} = \varphi(\rho_s - \rho_f)g \cos \theta h_m - (p_{f_m}^e)_{|b}$, with $(p_{f_m}^e)_{|b} = -\frac{\beta}{(1-\varphi)^2} \frac{h_m^2}{2} \Phi$. We also consider two possible computation.

Option 1. The basal solid pressure is calculated as the solution of the polynomial

$$(\sqrt{p_{s|b}})^3 + A_2 (\sqrt{p_{s|b}})^2 - \left(\varphi(\rho_s - \rho_f)g \cos \theta h_m + A_1 (\varphi - \varphi_c) \right) \sqrt{p_{s|b}} - A_2 (\varphi(\rho_s - \rho_f)g \cos \theta h_m + A_1 \varphi) = 0 \quad (\text{G.7a})$$

with coefficients $A_1 = \frac{\beta}{(1-\varphi)^2} \frac{h_m^2}{2} \dot{\gamma} K$, $A_2 = a(\alpha_\varphi d^2 \dot{\gamma}^2 \rho_s + \eta_f \dot{\gamma})$. The dilatancy function in equations (G.1) is given by

$$\Phi = \dot{\gamma} K(\varphi - \varphi^{\text{eq}}). \quad (\text{G.7b})$$

Option 2. The basal solid pressure is the solution of the following equation,

$$\partial_t p_{s|b} = -\frac{3}{2} B (\Phi - \dot{\gamma} K(\varphi - \varphi^{\text{eq}})), \quad (\text{G.8a})$$

with B the solid bulk modulus. The dilatancy function Φ is written in terms of the basal solid pressure using the expression of $(p_{f_m}^e)_{|b}$ that gives

$$\Phi = \frac{2(1-\varphi)^2}{\beta h_m^2} (p_{s|b} - \varphi(\rho_s - \rho_f)g \cos \theta h_m). \quad (\text{G.8b})$$

(B1) Two-layer model with two velocities in the mixture

The model with two velocities and an upper fluid layer with unknowns h_m, h_f, φ, u, v given in (4.1)-(4.4) reads

$$\partial_t h_m = h_m \Phi, \quad (\text{G.9a})$$

$$\partial_t h_f = -h_m \Phi, \quad (\text{G.9b})$$

$$\partial_t \varphi = -\varphi \Phi, \quad (\text{G.9c})$$

$$\begin{aligned} \partial_t (h_m v + \frac{\rho_f}{\rho} h_f V_m) = & -\mu \operatorname{sgn}(v) \frac{p_{s|b}}{\rho_s \varphi} + \frac{\beta}{\rho_s \varphi} h_m (u - v) - (h_m + \frac{\rho_f}{\rho} h_f) g \sin \theta \mathbf{e}_x \\ & - \frac{\rho_f}{\rho} ((1 - \lambda_f) u + \lambda_f V_m) h_m \Phi + \left(h_m v + (1 - \frac{\rho_f}{\rho}) \frac{\rho_f}{\rho} h_f V_m \right) \Phi, \end{aligned} \quad (\text{G.9d})$$

$$\begin{aligned} \partial_t (h_m u + \frac{\rho_f}{\rho} h_f V_m) = & -\frac{5}{2} \frac{\eta_e}{\rho_f h_m} u - \frac{\beta}{\rho_f (1 - \varphi)} h_m (u - v) - (h_m + \frac{\rho_f}{\rho} h_f) g \sin \theta \mathbf{e}_x \\ & + \frac{\rho_s \varphi}{\rho (1 - \varphi)} ((1 - \lambda_f) u + \lambda_f V_m) h_m \Phi - \left(h_m u + (1 - \frac{\rho_f}{\rho}) \frac{\rho_f}{\rho} h_f V_m \right) \frac{\varphi}{1 - \varphi} \Phi. \end{aligned} \quad (\text{G.9e})$$

Closures for β , $p_{s|b}$ and Φ are the same given above in (G.2) and (G.3) or (G.4). Denoting $Q_v = h_m v + \frac{\rho_f}{\rho} h_f V_m$ and $Q_u = h_m u + \frac{\rho_f}{\rho} h_f V_m$, the primitive phases velocities u, v are recovered as follows

$$v = \frac{h_m Q_v + \frac{\rho_f^2}{\rho^2} h_f (Q_v - Q_u)}{h_m (h_m + \frac{\rho_f}{\rho} h_f)}, \quad u = \frac{Q_u - m v}{h_m + \frac{\rho_f^2}{\rho^2} h_f},$$

with $m = \frac{\rho_f \rho_s \varphi}{\rho^2} h_f$.

(B2) Two-layer model with one velocity

The model with an upper fluid layer (3.1) or equivalently (3.9)-(3.10) for unknowns h_m, h_f, φ, v reads

$$\partial_t h_m = h_m \Phi, \quad (\text{G.10a})$$

$$\partial_t h_f = -h_m \Phi, \quad (\text{G.10b})$$

$$\partial_t \varphi = -\varphi \Phi, \quad (\text{G.10c})$$

$$\partial_t v = -\mu \operatorname{sgn}(v) \frac{p_{s|b}}{\rho h_m + \rho_f h_f} - \frac{5}{2} \frac{\eta_e (1 - \varphi)}{(\rho h_m + \rho_f h_f) h_m} v - g \sin \theta \mathbf{e}_x. \quad (\text{G.10d})$$

Closures for $p_{s|b}$ and Φ are the same given above in (G.2) and (G.3) or (G.4).

(C1) One-layer model with two velocities

The two-velocity model with one layer with unknowns H, φ, u, v given in (4.12) becomes

$$\partial_t H = \frac{\varphi(\rho_s - \rho_f)}{\rho} H \Phi^*, \quad (\text{G.11a})$$

$$\partial_t \varphi = -\varphi \Phi^*, \quad (\text{G.11b})$$

$$\partial_t v = -\mu \operatorname{sgn}(v) \frac{p_{s|b}^*}{\rho_s \varphi H} + \frac{\beta}{\rho_s \varphi} (u - v) - \frac{\rho_f}{\rho} ((1 - \lambda_f^*)u + \lambda_f^* V_m - v) \Phi^* - g \sin \theta \mathbf{e}_x, \quad (\text{G.11c})$$

$$\partial_t u = -\frac{5}{2} \frac{\eta_e}{\rho_f H^2} u - \frac{\beta}{\rho_f (1 - \varphi)} (u - v) + \frac{\rho_s \varphi}{\rho (1 - \varphi)} ((1 - \lambda_f^*)u + \lambda_f^* V_m - u) \Phi^* - g \sin \theta \mathbf{e}_x. \quad (\text{G.11d})$$

Closures for $\beta, \mu, p_{s|b}^*, \Phi^*$ are given in (G.13) and (G.14) or (G.15). The coefficient λ_f^* is defined analogously as

$$\lambda_f^* = \frac{1}{2} + \frac{1}{2} \operatorname{sgn}(\Phi^*) \delta_f, \quad \delta_f = \begin{cases} 0 & \text{centered distribution,} \\ 1 & \text{upwind distribution.} \end{cases}$$

(C2) One-layer model with one velocity

The model with 1 layer (3.14)-(3.15) with unknowns H, φ, v becomes

$$\partial_t H = \frac{\varphi(\rho_s - \rho_f)}{\rho} H \Phi^*, \quad (\text{G.12a})$$

$$\partial_t \varphi = -\varphi \Phi^*, \quad (\text{G.12b})$$

$$\partial_t v = -\mu^* \operatorname{sgn}(v) \frac{p_{s|b}^*}{\rho H} - \frac{5}{2} \frac{\eta_e (1 - \varphi)}{\rho H^2} v - g \sin \theta \mathbf{e}_x. \quad (\text{G.12c})$$

The closures in this case are analogous to (G.2) and they read as follows. The friction coefficient is

$$\mu^* = (\mu^{\text{eq}*} + K(\varphi - \varphi^{\text{eq}*}))_+. \quad (\text{G.13a})$$

The rheological laws are

$$\begin{aligned} \varphi^{\text{eq}*} &= \frac{\varphi_c}{1 + b_\varphi (\mathcal{J}_\varphi^*)^{1/2}} \quad \text{with} \quad \mathcal{J}_\varphi^* = \alpha_\varphi (I^*)^2 + J^*, \\ \mu^{\text{eq}*} &= \mu_c + \frac{\Delta \mu}{I_0 + (\mathcal{J}_\mu^*)^{1/2}} (\mathcal{J}_\mu^*)^{1/2} \quad \text{with} \quad \mathcal{J}_\mu^* = \alpha_\mu (I^*)^2 + J^*, \\ \text{where} \quad I^* &= \frac{d\dot{\gamma}^*}{\sqrt{p_{s|b}^*/\rho_s}}, \quad J^* = \frac{\eta_f \dot{\gamma}^*}{p_{s|b}^*}, \quad \dot{\gamma}^* = \frac{5}{2} \frac{|v|}{H}. \end{aligned} \quad (\text{G.13b})$$

We also have in this case two option to compute the basal solid pressure, denoted by $p_{s|b}^*$.

Option 1 for the computation of $p_{s|b}^*$. For this first option $p_{s|b}^*$ is defined by $p_{s|b}^* = \varphi(\rho_s - \rho_f)g \cos \theta H - (p_{f_m}^e)_{|b}^*$, with $(p_{f_m}^e)_{|b}^* = -\frac{\beta}{(1-\varphi)^2} \frac{h_m^2}{2} \Phi^*$, what implies again an implicit definition. The basal solid pressure is calculated as the rooth of a third order polynomial,

$$(\sqrt{p_{s|b}^*})^3 + A_2 (\sqrt{p_{s|b}^*})^2 - \left(\varphi(\rho_s - \rho_f)g \cos \theta H + A_1 (\varphi - \varphi_c) \right) \sqrt{p_{s|b}^*} - A_2 (\varphi(\rho_s - \rho_f)g \cos \theta H + \varphi A_1) = 0 \quad (\text{G.14a})$$

with coefficients $A_1 = \frac{\beta}{(1-\varphi)^2} \frac{h_m^2}{2} \dot{\gamma}^* K$, $A_2 = b(\alpha_\varphi d^2 (\dot{\gamma}^*)^2 \rho_s + \eta_f \dot{\gamma}^*)^{1/2}$. The dilatancy function is given by

$$\Phi^* = \dot{\gamma}^* K (\varphi - \varphi^{\text{eq}*}). \quad (\text{G.14b})$$

Option 2 for the computation of $p_{s|b}^*$. The basal solid pressure is the solution of the following equation,

$$\partial_t p_{s|b}^* = -\frac{3}{2} B (\Phi^* - \dot{\gamma}^* K (\varphi - \varphi^{\text{eq}*})), \quad (\text{G.15a})$$

with B the solid bulk modulus. The dilatancy function Φ^* is

$$\Phi^* = \frac{2(1-\varphi)^2}{\beta H^2} (p_{s|b}^* - \varphi(\rho_s - \rho_f) g \cos \theta H). \quad (\text{G.15b})$$

G.2 Other models in uniform regime

Iverson-George model [IG]

Finally we write the Iverson-George model given in equations (3.16) in the uniform regime with unknowns h, φ, v, p_b .

$$\partial_t h = \frac{\varphi(\rho_s - \rho_f)}{\rho} D, \quad (\text{G.16a})$$

$$\partial_t \varphi = -\varphi \frac{D}{h}, \quad (\text{G.16b})$$

$$\partial_t v = -\frac{\tau_s + \tau_f}{\rho h} - g \sin \theta \mathbf{e}_x. \quad (\text{G.16c})$$

$$\partial_t p_b = \frac{1}{4} g \cos \theta \rho_f \frac{\rho - \rho_f}{\rho} D + \frac{3}{2\alpha} \left(\frac{D}{h} - \dot{\gamma}_{\text{IG}} \tan \psi_{\text{IG}} \right). \quad (\text{G.16d})$$

The closures are given as in (3.17a)-(3.17f) that read

$$\tau_f = (1-\varphi)\eta_e \frac{2v}{h}, \quad \tau_s = \mu_{\text{IG}} \frac{v}{|v|} \sigma_e, \quad \mu_{\text{IG}} = \tan(\delta + \psi_{\text{IG}}), \quad (\text{G.17a})$$

$$\sigma_e = \rho g \cos \theta h - p_b, \quad p_b = \rho_f g \cos \theta h + p_e. \quad (\text{G.17b})$$

The dilatancy function is

$$D = -\frac{2k_{\text{IG}}}{h\eta_e} p_e, \quad k_{\text{IG}} = k_0 e^{\frac{0.6-\varphi}{0.04}}, \quad (\text{G.17c})$$

and finally the rheological relations are

$$\tan \psi_{\text{IG}} = \varphi - \varphi_{\text{IG}}^{\text{eq}}, \quad \varphi_{\text{IG}}^{\text{eq}} = \frac{\varphi_c}{1 + \sqrt{N}}, \quad N = \frac{J}{1 + I^2}, \quad \dot{\gamma}_{\text{IG}} = \frac{2|v|}{h}. \quad (\text{G.17d})$$

Meng-Wang model [MW]

Lastly, we write the Meng-Wang model with unknowns h, φ, u, v given in (4.16) in the uniform regime. We use that

$$\mathfrak{J} = -\varphi \frac{\rho_f \rho_s}{\rho} h \Phi_{\text{MW}}.$$

So it reads

$$\partial_t h = \frac{\varphi(\rho_s - \rho_f)}{\rho} h \Phi_{\text{MW}}, \quad (\text{G.18a})$$

$$\partial_t \varphi = -\varphi \Phi_{\text{MW}}, \quad (\text{G.18b})$$

$$\partial_t v = -\text{sgn}(v) \mu_{\text{MW}} \frac{p_{s|b}}{\rho_s \varphi h} + \frac{\beta_{\text{MW}}}{\rho_s \varphi} (u - v) - g \sin \theta \mathbf{e}_x - (1 - \lambda)(u - v) \frac{\rho_f}{\rho} \Phi_{\text{MW}} - \frac{\alpha_s}{\rho_s h} v, \quad (\text{G.18c})$$

$$\partial_t u = -\frac{\alpha_f}{\rho_f h} u - \frac{\beta_{\text{MW}}}{\rho_f (1 - \varphi)} (u - v) - g \sin \theta \mathbf{e}_x - \lambda (u - v) \frac{\varphi \rho_s}{\rho (1 - \varphi)} \Phi_{\text{MW}}. \quad (\text{G.18d})$$

The closures are given in (4.16e)-(4.16i) and read

$$\begin{aligned} \Phi_{\text{MW}} &= \dot{\gamma}_{\text{MW}} \tan \psi_{\text{MW}}, \quad \tan \psi_{\text{MW}} = K_1 (\varphi - \varphi_{\text{MW}}^{\text{eq}}), \quad \varphi_{\text{MW}}^{\text{eq}} = \varphi_c - K_2 \frac{\eta_f \dot{\gamma}_{\text{MW}}}{p_{s|b}}, \\ \dot{\gamma}_{\text{MW}} &= 3 \frac{|v|}{h}, \quad \mu_{\text{MW}} = \tan(\delta + \psi_{\text{MW}}), \quad \beta_{\text{MW}} = (1 - \varphi)^2 \frac{\eta_f}{k_{\text{MW}}}. \end{aligned} \quad (\text{G.19a})$$

The pressure terms are

$$p_{s|b} = \varphi (\rho_s - \rho_f) g \cos \theta h - (p_e)_{|b}, \quad (p_e)_{|b} = -\frac{1}{2} \frac{\beta_{\text{MW}}}{(1 - \varphi)^2} h^2 \Phi_{\text{MW}}. \quad (\text{G.19b})$$

The distribution coefficient is $\lambda = 1 - \varphi$, and the hydraulic permeability k_{MW} , and coefficients α_s , α_f are considered as constants.

H Supplementary material for numerical results

H.1 Influence of the parameters on long-term stationary states

In figure 26 the stationary states for the height of the mixture, velocity and concentration are presented as a function of three parameters around their reference values $a_\mu = 11.29$, $b_\varphi = 0.66$ and $I_0 = 0.279$ [56]. Only one parameter is varied while the others stay constant.

From the first row of figure 26, we can observe that the bigger influence of a_μ is on the velocity. On the other hand, the stationary velocities are independent of b_φ which has a bigger influence on the concentration. The third row shows that I_0 has only a small influence on all the quantities. Finally, we can also observe on the third column that all parameters have a small influence on the stationary height of the mixture.

In this figure the stationary solution for the case of the rheology considered in [7] is also presented. We can observe that for bigger values of b_φ the stationary concentrations in the present model and in [7] are close. In figure 27 the stationary solutions are represented as a function of a_μ , but with $b_\varphi/0.66 = 1.5$. In particular for $a_\mu/11.29 \approx 0.5$ the stationary solutions for the velocity, concentration and height of the mixture with the new rheology are very close to the solutions in [7]. Then, for the following tests in this paper we set $a_\mu = 11.29/2$, $b_\varphi = 0.66 \cdot 1.5$, $I_0 = 0.279$.

Figure 28 shows the evolution of the two dimensionless numbers in the rheology I^2 and J corresponding to test 5.1. For high and low viscosity cases J is bigger than I^2 and for the case of high viscosity I^2 is negligible.

H.2 Forces in models in uniform regime

We present in the next table the forces applying to each model in the uniform regime, for equations written in conservative form.

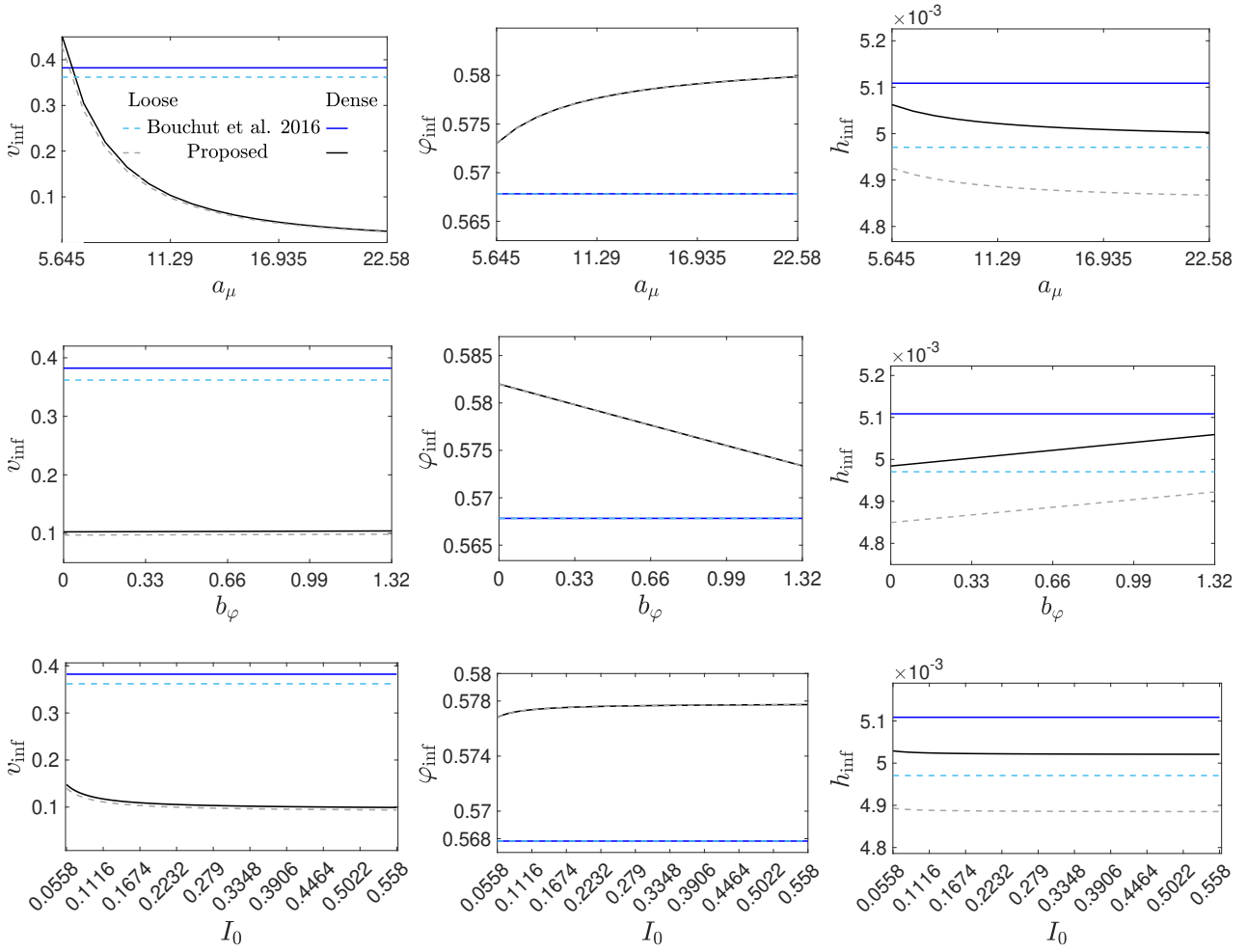


Figure 26: Long-term stationary states as a function of a_μ , b_φ , I_0 : (first column) solid velocity v_{inf} , (second column) concentration φ_{inf} and (third column) height of the mixture h_{inf} in the immersed simulations in section 5.1.

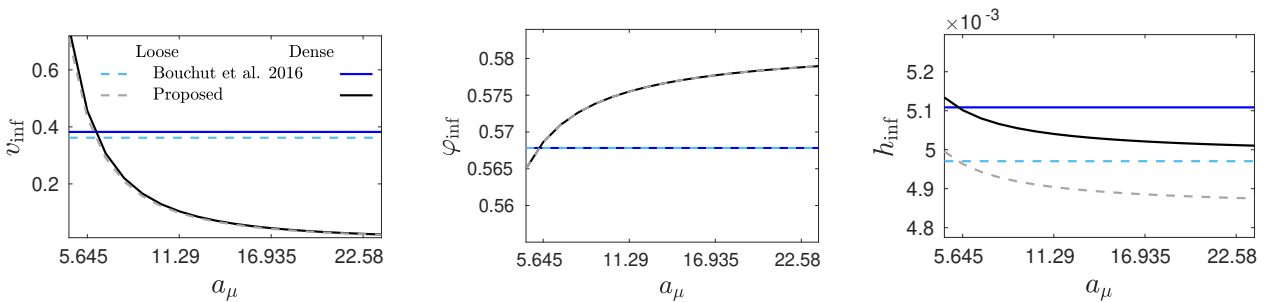
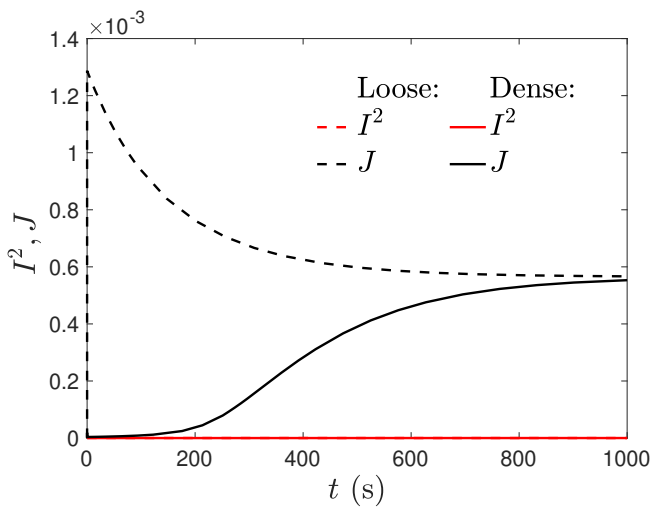


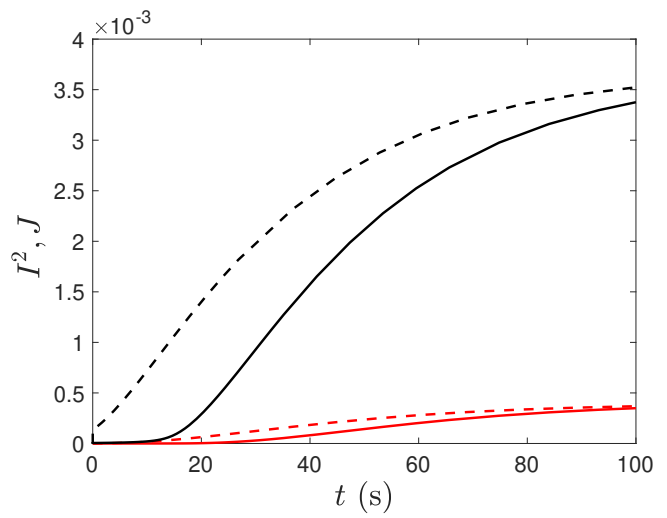
Figure 27: Long-term stationary states as a function of a_μ , b_φ , I_0 , but now around reference values $I_0 = 0.279$ and $b_\varphi = 0.66 \times 1.5$: (first column) solid velocity v_{inf} , (second column) concentration φ_{inf} and (third column) height of the mixture h_{inf} in the immersed simulations in section 5.1.

Model	f_{fricsb}	f_{fricfb}	f_{dragmix}	f_{dragf}	f_{transf}	f_{grav}
v	$-\mu \text{sgn}(v)p_{s_b}$	—	$\beta(u-v)h_m$	$k_f \frac{\rho_s \mathcal{L}}{\rho}(u_f - V_m)$	—	$-\rho_s \varphi h_m g \sin \theta$
(A1)	—	$-\frac{5}{2} \frac{\eta_e(1-\varphi)}{h_m} u$	$-\beta(u-v)h_m$	$k_f \frac{\rho_f(1-\varphi)}{\rho}(u_f - V_m)$	$((1-\lambda_f)u + \lambda_f u_f)\rho_f h_m \Phi$	$-\rho_f(1-\varphi)h_m g \sin \theta$
u_f	—	—	—	$-k_f(u_f - V_m)$	$-((1-\lambda_f)u + \lambda_f u_f)\rho_f h_m \Phi$	$-\rho_f h_f g \sin \theta$
v	$-\mu \text{sgn}(v)p_{s_b}$	—	$\beta(u-v)h_m$	—	—	$-\rho_s \varphi h_m g \sin \theta$
(B1)	—	$-\frac{5}{2} \frac{\eta_e(1-\varphi)}{h_m} u$	$-\beta(u-v)h_m$	—	$((1-\lambda_f)u + \lambda_f V_m)\rho_f h_m \Phi$	$-\rho_f(1-\varphi)h_m g \sin \theta$
V_m	—	—	—	—	$-((1-\lambda_f)u + \lambda_f V_m)\rho_f h_m \Phi$	$-\rho_f h_f g \sin \theta$
(C1)	$-\mu \text{sgn}(v)p_{s_b}^*$	—	$\beta(u-v)H$	—	$-\frac{\rho_s \mathcal{L}}{\rho}((1-\lambda_f^*)u + \lambda_f^* V_m)\rho_f H \Phi$	$-\rho_s \varphi H g \sin \theta$
u	—	$-\frac{5}{2} \frac{\eta_e(1-\varphi)}{H} u$	$-\beta(u-v)H$	—	$\frac{\rho_s \mathcal{L}}{\rho}((1-\lambda_f^*)u + \lambda_f^* V_m)\rho_f H \Phi$	$-\rho_f(1-\varphi)H g \sin \theta$
(A2)	$-\mu \text{sgn}(v)p_{s_b}$	$-\frac{5}{2} \frac{\eta_e(1-\varphi)}{h_m} v$	—	$k_f(u_f - v)$	$((1-\lambda_f)v + \lambda_f u_f)\rho_f h_m \Phi$	$-\rho h_m g \sin \theta$
u_f	—	—	—	$-k_f(u_f - v)$	$((1-\lambda_f)v + \lambda_f u_f)\rho_f h_m \Phi$	$-\rho_f h_f g \sin \theta$
(B2)	$-\mu \text{sgn}(v)p_{s_b}$	$-\frac{5}{2} \frac{\eta_e(1-\varphi)}{h_m} v$	—	—	—	$-(\rho h_m + \rho_f h_f)g \sin \theta$
(C2)	$-\mu \text{sgn}(v)p_{s_b}^*$	$-\frac{5}{2} \frac{\eta_e(1-\varphi)}{H} v$	—	—	—	$-\rho H g \sin \theta$

Table 6: Forces for the uniform configuration for all models. Forces are written from the conservative equations and they are: solid bottom friction f_{fricsb} , fluid bottom friction f_{fricfb} , drag in the mixture f_{dragmix} , drag with fluid upper layer f_{dragf} , fluid transfer f_{transf} , gravity f_{grav} . Note that $k_f = \frac{\rho h_m \rho_f h_f}{\rho h_m + \rho_f h_f} |u_f - V_m|$ for the (A1) model and $k_f = \frac{\rho h_m \rho_f h_f}{\rho h_m + \rho_f h_f} |u_f - v|$ for the (A2) model. We denote f_{tot} the sum of all forces which represents the mass acceleration for each model which is equal to $\partial_t u$ in our uniform configuration.



(a) I^2 and J high viscosity



(b) I^2 and J low viscosity

Figure 28: Time change of I^2 and J for high and low viscosity cases in the immersed simulations in section 5.1.

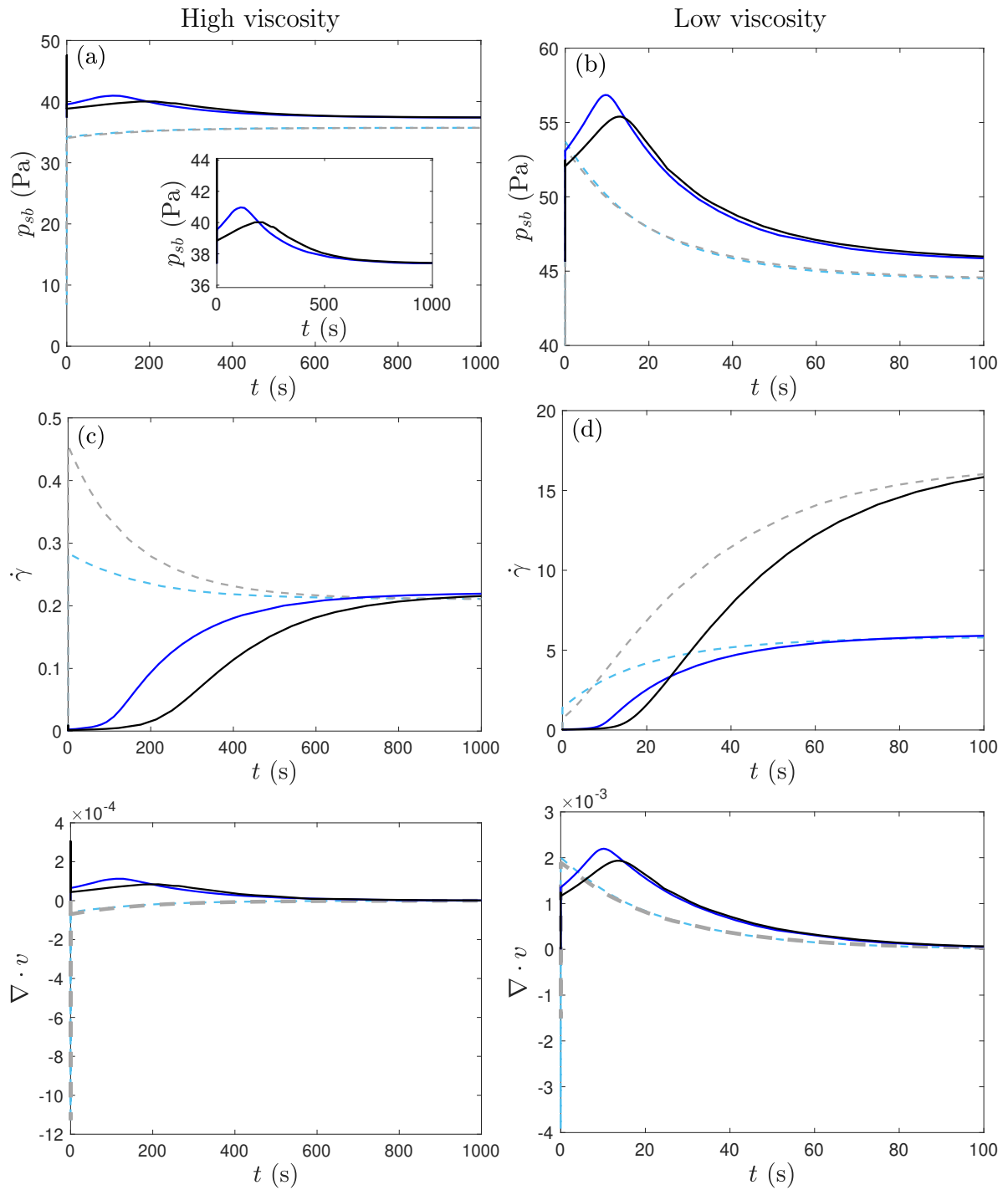


Figure 29: p_{sb} and $\dot{\gamma}$ in the high viscosity (left) and low viscosity case (right) in the immersed simulations in section 5.1, see figure 9.

References

- [1] K. Allstadt, R. Matoza, A. Lockhart, S. Moran, J. Caplan-Auerbach, and M. Haney. Seismic and acoustic signatures of surficial mass movements at volcanoes. *J. Volcanol. Geotherm. Res.*, (364), 2018.
- [2] L. Amarsid, J.-Y. Delenne, P. Mutabaruka, Y. Monerie, F. Perales, and F. Radjai. Viscoplastic regime of immersed granular flows. *Physical Review E*, 96(1):012901, jul 2017.
- [3] S. Athani, B. Metzger, Y. Forterre, and R. Mari. Transient flows and migration in granular suspensions: key role of reynolds-like dilatancy. *Journal of Fluid Mechanics*, 949:A9, 2022.
- [4] A. S. Baumgarten and K. Kamrin. A general fluid–sediment mixture model and constitutive theory validated in many flow regimes. *Journal of Fluid Mechanics*, 861:721–764, 2019.
- [5] F. Bouchut, E. D. Fernández-Nieto, A. Mangeney, and P. Y. Lagrée. On new erosion models of savage–hutter type for avalanches. *Acta Mechanica*, 199(1):181–208, 2008.
- [6] F. Bouchut, E. D. Fernández-Nieto, A. Mangeney, and G. Narbona-Reina. A two-phase shallow debris flow model with energy balance. *ESAIM: M2AN*, 49(1):101–140, 2015.
- [7] F. Bouchut, E. D. Fernández-Nieto, A. Mangeney, and G. Narbona-Reina. A two-phase two-layer model for fluidized granular flows with dilatancy effects. *Journal of Fluid Mechanics*, 801:166–221, 2016.
- [8] F. Bouchut, E. D. Fernández-Nieto, E. H. Koné, A. Mangeney, and G. Narbona-Reina. Dilatancy in dry granular flows with a compressible $\mu(i)$ rheology. *Journal of Computational Physics*, 429:110013, 2021.
- [9] F. Boyer, É. Guazzelli, and O. Pouliquen. Unifying suspension and granular rheology. *Physical Review Letters*, 107(18):188301, oct 2011.
- [10] C. Cassar, M. Nicolas, and O. Pouliquen. Submarine granular flows down inclined planes. *Physics of Fluids*, 17(10):103301, 2005.
- [11] J. Chauchat and M. Médale. A three-dimensional numerical model for incompressible two-phase flow of a granular bed submitted to a laminar shearing flow. *Computer Methods in Applied Mechanics and Engineering*, 199(9–12):439–449, 2010.
- [12] Y. F. Dafalias and M. T. Manzari. Simple plasticity sand model accounting for fabric change effects. *Journal of Engineering Mechanics*, 130(6):622–634, 2004.
- [13] R. de Boer and W. Ehlers. The development of the concept of effective stresses. *Acta Mechanica*, 83(1):77–92, 1990.
- [14] E. Drach. *Shallow-water type models for wet debris flows with dilatancy*. PhD thesis, Université Gustave-Eiffel (Paris), 2023.
- [15] A. Einstein. A new determination of molecular dimensions. *Ann.d.Phys*, 19:289–306, 1906.
- [16] F. Engelund. *On the laminar and turbulent flows of ground water through homogeneous sand*. Danish Academy of Technical Sciences / Transactions. Akademiet for de tekniske videnskaber, 1953.

- [17] J. Garres-Díaz, F. Bouchut, E. Fernández-Nieto, A. Mangeney, and G. Narbona-Reina. Multilayer models for shallow two-phase debris flows with dilatancy effects. *Journal of Computational Physics*, 419:109699, 2020.
- [18] D. George and R. Iverson. A depth-averaged debris-flow model that includes the effects of evolving dilatancy. II. Numerical predictions and experimental tests. *Proceedings of the Royal Society A: Mathematical, Physical and Engineering Sciences*, 470(2170):20130820, 2014.
- [19] D. L. George, R. M. Iverson, and C. M. Cannon. New methodology for computing tsunami generation by subaerial landslides: Application to the 2015 tyndall glacier landslide, alaska. *Geophysical Research Letters*, 44(14):7276–7284, 2017.
- [20] R. Holtzman, D. B. Silin, and T. W. Patzek. Mechanical properties of granular materials: A variational approach to grain-scale simulations. *International Journal for Numerical and Analytical Methods in Geomechanics*, 33(3):391–404, 2009.
- [21] O. Hungr and S. McDougall. Two numerical models for landslide dynamic analysis. *Computers & Geosciences*, 35(5):978–992, 2009. Modelling and Simulation of Dangerous Phenomena for Hazard Mapping.
- [22] R. M. Iverson. The physics of debris flows. *Reviews of Geophysics*, 35(3):245–296, 1997.
- [23] R. M. Iverson and D. L. George. A depth-averaged debris-flow model that includes the effects of evolving dilatancy. I. Physical basis. *Proceedings of the Royal Society A: Mathematical, Physical and Engineering Sciences*, 470(2170):20130819, 2014.
- [24] R. M. Iverson, M. Logan, R. G. LaHusen, and M. Berti. The perfect debris flow? aggregated results from 28 large-scale experiments. *Journal of Geophysical Research: Earth Surface*, 115(F3), 2010.
- [25] R. M. Iverson, M. E. Reid, N. R. Iverson, R. G. LaHusen, M. Logan, J. E. Mann, and D. L. Brien. Acute sensitivity of landslide rates to initial soil porosity. *Science*, 290(5491):513–516, 2000.
- [26] R. Jackson. *The Dynamics of Fluidized Particles*. Cambridges Monographs on Mechanics. Cambridge University Press, 2000.
- [27] C.-H. Lee. Two-phase modelling of submarine granular flows with shear-induced volume change and pore-pressure feedback. *Journal of Fluid Mechanics*, 907:A31, 2021.
- [28] A. Leonardi, M. Cabrera, F. K. Wittel, R. Kaitna, M. Mendoza, W. Wu, and H. J. Herrmann. Granular-front formation in free-surface flow of concentrated suspensions. *Phys. Rev. E*, 92:052204, Nov 2015.
- [29] I. Luca, C. Y. Kuo, K. Hutter, and Y. C. Tai. Modeling Shallow Over-Saturated Mixtures on Arbitrary Rigid Topography. *Journal of Mechanics*, 28(3):523–541, 08 2012.
- [30] A. Lucas, A. Mangeney, and J. P. Ampuero. Frictional velocity-weakening in landslides on earth and on other planetary bodies. *Nature Communications*, 5(3417), 2014.
- [31] M. Pelanti, F. Bouchut, and A. Mangeney. A Roe-type scheme for two-phase shallow granular flows over variable topography. *ESAIM: M2AN*, 42(5):851–885, 2008.

- [32] A. Mangeney, F. Bouchut, N. Thomas, J. P. Vilotte, and M. O. Bristeau. Numerical modeling of self-channeling granular flows and of their levee-channel deposits. *Journal of Geophysical Research: Earth Surface*, 112(F2):n/a–n/a, 2007. F02017.
- [33] A. Mangeney-Castelnau, J.-P. Vilotte, M. O. Bristeau, B. Perthame, F. Bouchut, C. Simeoni, and S. Yerneni. Numerical modeling of avalanches based on Saint Venant equations using a kinetic scheme. *Journal of Geophysical Research: Solid Earth*, 108(B11):n/a–n/a, 2003. 2527.
- [34] X. Meng, C. Johnson, and J. Gray. Formation of dry granular fronts and watery tails in debris flows. *Journal of Fluid Mechanics*, 943:A19, 2022.
- [35] X. Meng and Y. Wang. Modeling dynamic flows of grain–fluid mixtures by coupling the mixture theory with a dilatancy law. *Acta Mech*, 229(6):2521–2538, 2018.
- [36] X. Meng, Y. Wang, C. Wang, and J.-T. Fisher. Modeling of unsaturated granular flows by a two-layer approach. *Acta Geotechnica*, 12(3):677–701, 2017.
- [37] E. Montellà, J. Chauchat, C. Bonamy, D. Weij, G. Keetels, and T. Hsu. Numerical investigation of mode failures in submerged granular columns. *Flow*, 3:E28, 2023.
- [38] E. Montellà, J. Chauchat, B. Chareyre, C. Bonamy, and T. Hsu. A two-fluid model for immersed granular avalanches with dilatancy effects. *Journal of Fluid Mechanics*, 925:A13, 2021.
- [39] L. Moretti, K. Allstadt, A. Mangeney, Y. Capdeville, E. Stutzmann, and F. Bouchut. Numerical modeling of the mount meager landslide constrained by its force history derived from seismic data. *Journal of Geophysical Research: Solid Earth*, 120(4):2579–2599, 2015.
- [40] L. Moretti, A. Mangeney, Y. Capdeville, E. Stutzmann, C. Huggel, D. Schneider, and F. Bouchut. Numerical modeling of the mount steller landslide flow history and of the generated long period seismic waves. *Geophysical Research Letters*, 39(16), 2012.
- [41] M. Ouriemi, P. Aussillous, and E. Guazzelli. Sediment dynamics. part 1. bed-load transport by laminar shearing flows. *Journal of Fluid Mechanics*, 636:295–319, 2009.
- [42] M. Pailha, M. Nicolas, and O. Pouliquen. Initiation of underwater granular avalanches: Influence of the initial volume fraction. *Physics of Fluids*, 20(11):111701, 2008.
- [43] M. Pailha and O. Pouliquen. A two-phase flow description of the initiation of underwater granular avalanches. *Journal of Fluid Mechanics*, 633:115–135, 2009.
- [44] M. Pelanti, F. Bouchut, and A. Mangeney. A riemann solver for single-phase and two-phase shallow flow models based on relaxation. relations with roe and vfroe solvers. *Journal of Computational Physics*, 230(3):515–550, 2011.
- [45] M. Peruzzetto, J.-C. Komorowski, A. Le Friant, M. Rosas-Carbajal, A. Mangeney, and Y. Legendre. Modeling of partial dome collapse of la soufrière of guadeloupe volcano: implications for hazard assessment and monitoring. *Scientific Reports*, 9(1):13105, 2019.
- [46] M. Peruzzetto, C. Levy, Y. Thiery, G. Grandjean, A. Mangeney, A.-M. Lejeune, A. Nachbaur, Y. Legendre, B. Vittecoq, J.-M. Saurel, V. Clouard, T. Dewez, F. R. Fontaine,

- M. Mergili, S. Lagarde, J.-C. Komorowski, A. Le Friant, and A. Lemarchand. Simplified simulation of rock avalanches and subsequent debris flows with a single thin-layer model: Application to the pêcheur river (martinique, lesser antilles). *Engineering Geology*, 296:106457, 2022.
- [47] M. Peruzzetto, A. Mangeney, F. Bouchut, G. Grandjean, C. Levy, Y. Thiery, and A. Lucas. Topography curvature effects in thin-layer models for gravity-driven flows without bed erosion. *Journal of Geophysical Research: Earth Surface*, 126(4):e2020JF005657, 2021. e2020JF005657 2020JF005657.
- [48] E. Pitman and L. Le. A two-fluid model for avalanche and debris flows. *Philosophical Transactions of the Royal Society of London A: Mathematical, Physical and Engineering Sciences*, 363(1832):1573–1601, 2005.
- [49] P. Poulain, A. L. Friant, A. Mangeney, S. Viroulet, E. Fernandez-Nieto, M. Castro Diaz, M. Peruzzetto, G. Grandjean, F. Bouchut, R. Pedreros, and J.-C. Komorowski. Performance and limits of a shallow-water model for landslide-generated tsunamis: from laboratory experiments to simulations of flank collapses at Montagne Pelée (Martinique). *Geophysical Journal International*, 233(2):796–825, 12 2022.
- [50] S. P. Pudasaini, Y. Wang, and K. Hutter. Modelling debris flows down general channels. *Natural Hazards and Earth System Sciences*, 5(6):799–819, 2005.
- [51] L. Rondon, O. Pouliquen, and P. Aussillous. Granular collapse in a fluid: Role of the initial volume fraction. *Physics of Fluids*, 23(7):073301, 07 2011.
- [52] S. Roux and F. Radjai. *Texture-Dependent Rigid-Plastic Behavior*, pages 229–236. Springer Netherlands, Dordrecht, 1998.
- [53] S. B. Savage and K. Hutter. The motion of a finite mass of granular material down a rough incline. *Journal of Fluid Mechanics*, 199:177–215, 1989.
- [54] W. Sun, X. Meng, Y. Wang, S. S. Hsiau, and Z. You. A depth-averaged description of submarine avalanche flows and induced surface waves. *Journal of Geophysical Research: Earth Surface*, 128(4):e2022JF006893, 2023. e2022JF006893 2022JF006893.
- [55] F. Tapia, M. Ichihara, O. Pouliquen, and E. Guazzelli. Viscous to inertial transition in dense granular suspension. *Phys. Rev. Lett.*, 129:078001, 2022.
- [56] F. Tapia, O. Pouliquen, and E. Guazzelli. Influence of surface roughness on the rheology of immersed and dry frictional spheres. *Phys. Rev. Fluids*, 4:104302, Oct 2019.
- [57] M. Trulsson, B. Andreotti, and P. Claudin. Transition from the viscous to inertial regime in dense suspensions. *Physical Review Letters*, 109(11):118305, 2012.